Maximum-Entropy Meshfree Method for Linear and Nonlinear Elasticity

By

ALEJANDRO A. ORTIZ
B.S. (Universidad Técnica Federico Santa María) 2002
M.E. (Universitat Politècnica de Catalunya) 2006

DISSERTATION

Submitted in partial satisfaction of the requirements for the degree of

DOCTOR OF PHILOSOPHY

in

Civil and Environmental Engineering

in the

OFFICE OF GRADUATE STUDIES

of the

UNIVERSITY OF CALIFORNIA

DAVIS

Approved:

Natarajan Sukumar (Chair)

Yannis F. Dafalias

John E. Bolander

Committee in Charge

2011

Alejandro A. Ortiz
March 2011
Civil and Environmental Engineering

Maximum-Entropy Meshfree Method for Linear and Nonlinear Elasticity

ABSTRACT

A Galerkin-based maximum-entropy meshfree method for linear and nonlinear elastic media is developed. The standard displacement-based Galerkin formulation is used to model compressible linear elastic solids, whereas the classical u-p mixed formulation for near-incompressible linear elastic media is adopted to formulate a volume-averaged nodal technique in which the pressure variable is eliminated from the analysis. This results in a single-field formulation that is devoid of volumetric locking. A modified Gauss integration technique that alleviates integration errors in meshfree methods with guaranteed patch test satisfaction to machine precision is devised. The performance of the maximum-entropy meshfree method is assessed for problems in compressible and near-incompressible linear elastic media using three-node triangular and four-node tetrahedral background meshes. Both structured and unstructured meshes are considered to assess the accuracy, performance and stability of the maximum-entropy meshfree method by means of various numerical experiments, which include patch tests, bending dominated problem, combined bending-shear problem, rigid indentation, Stokes flow and numerical stability tests.

An extension of the volume-averaged nodal technique is proposed for the analysis of near-incompressible nonlinear elastic solids in two dimensions. In the nonlinear version, the volume change ratio of the dilatational constraint, namely J, is volume-averaged around nodes leading to a locking-free displacement-based formulation. The excellent performance of the maximum-entropy meshfree method for problems in near-incompressible nonlinear elastic solids is demonstrated via three standard two-dimensional numerical experiments—a combined bending-shear problem, a plane strain compression of a rubber block and a frictionless indentation problem. Three-node structured and unstructured triangular background meshes are employed and the results are compared to two finite element methods

that use such meshes, namely, the linear displacement/constant pressure triangle and the linear displacement/linear pressure triangle enriched with a displacement bubble node (`MINI` element). The two-dimensional nonlinear simulations reveal that the maximum-entropy meshfree method effectively improves the poor performance of linear triangular meshes in the analysis of near-incompressible solids at finite strains.

To My Wife, Constanza, and My Two Sons, Martín and Vicente

ACKNOWLEDGMENTS

This dissertation would not have been possible without the guidance and help of several individuals who in one way or another contributed and extended their valuable assistance in the preparation and completion of this study.

First and foremost, my sincerest gratitude to my academic supervisor, Professor Natarajan Sukumar, for his guidance, advising, support and encouragement throughout my doctoral studies at UC Davis. I was most fortunate to be fostered by his expertise in unconventional numerical methods for applications in science and engineering, especially, in meshfree methods. I am deeply grateful for his tremendous insights that always made me think more than once about my thoughts. I acknowledge his willingness to allow me the room to work in my own way. As a result, research life became smooth and rewarding for me.

I would like to express my sincere gratitude to Professor Yannis Dafalias, of my dissertation committee, for his willingness to discuss many theoretical things related to continuum mechanics and nonlinear elasticity. I am also thankful that he could do the reviewing of this dissertation, even though he was far away from here. I appreciate his friendship beyond academic discussions, constant encouragement and advices on academic life. My sincere thanks to him for having made my research life at UC Davis completer.

I am grateful to Professor John Bolander, of my dissertation committee, for his helpful suggestions, insightful observations and constructive criticism on the writing of this dissertation. His feedback impacted very positively the overall presentation of this dissertation.

Also, I would like to thank to Dr. Mike Puso, from Lawrence Livermore National Laboratory, for his generosity in discussing most of the topics that gave form to this dissertation. I am especially thankful to him for sharing his expertise in nonlinear solvers with me. I am also thankful to Professor Thomas J. R. Hughes for many clarifications on the F-bar methodology over e-mail. My thanks are also extended to Professor Klaus-Jürgen Bathe

for his availability to discuss theoretical aspects of the numerical inf-sup test over e-mail.

Finally, the everlasting and unconditional love and support from my family, especially, from my grandparents, Guillermo and Rina, who have enthusiastically followed all my academic endeavors, and from my wife, Constanza, who resigned from everything she had to stay with me during the course of my graduate studies. I am endlessly indebted to her for this and for giving me two wonderful sons.

Contents

List of Figures

List of Tables

Chapter 1

Introduction

1.1 Background and Motivations

In the Finite Element Method (FEM), the numerical approximation is locally built by means of shape functions that are defined over non-overlapping subdivisions (elements) that divide a domain of interest. These subdivisions are connected together by a topological map termed mesh. The foregoing features of FEM render it to be well-suited to solve partial differential equations (PDEs): they lead to well-established formulas for the finite element shape functions, which makes computation of shape functions straightforward; finite element shape functions are endowed with the so-called Kronecker-delta property, which allows the imposition of essential boundary conditions in a direct and simple manner; and very efficient and inexpensive computations are obtained since the final discrete system is banded and sparse. Despite these striking advantages that arise in many practical applications, a number of shortcomings that emanate from the need of a mesh are present in the finite element method. For instance, mesh distortions (especially in large deformation analysis) breakdown the simulation very early leading to inaccurate solutions; the accuracy of finite element computations is strongly dependent on the quality of the mesh, which complicates its generation, especially in three-dimensional settings with complex geometries; the piece-wise continuous character of finite element shape functions induces mesh alignment

sensitivity along shear band formations, which makes the numerical solution dependent on the mesh structure and element edge orientation.

The above-mentioned drawbacks and many others (see for instance, Refs. [1,2]) provide motivation for the development of alternative numerical procedures to improve the performance of simulations that otherwise are intractable with standard finite elements. Meshfree methods, whose approximations are not built using a mesh, are a promising alternative. However, meshfree methods are not exempt from drawbacks either. For instance, meshfree methods are prone to errors in the numerical integration of the weak form. As a means to alleviate these errors, expensive numerical integration technique is usually needed, which impacts the overall computational cost. For instance, Gauss integration with higher-order accurate scheme on a background mesh of finite elements [3, 4] or the use of higher-order quadrature rules on integration cells aligned with the support of shape functions [5, 6] are typically adopted. Thus, an in-depth understanding of the numerical integration error in meshfree methods, ways to control it, and the development of more efficient integration techniques are necessary.

Standard displacement-based Galerkin formulations exhibit severe stiffening when modeling near-incompressible materials. In elasticity theory, this occurs when the Poisson's ratio ν approaches 1/2, and is referred to as volumetric locking. In finite elements, some of the approaches to alleviate locking are: reduced/selective integration [7], B-bar technique [8], mixed formulations [9], and assumed strain methods [10]. All of these techniques are in fact specific instances of mixed formulations. The equivalence between reduced/selective integration and mixed formulation was demonstrated by Malkus and Hughes [9]. The B-bar technique and assumed strain methods can be derived from the three-field Hu-Washizu mixed formulation [11]. A recently developed B-bar technique for NURBS-based isogeometric analysis [12] is obtained by an L^2 projection of the dilatational strain onto the lower order approximation space—typically, the pressure space in a mixed u-p formulation.

An important consideration in employing mixed formulations is the selection of the approximation spaces since not all choices for them lead to stability. In particular, the

stability of two-field mixed formulations, such as u-p, is characterized by the Ladyzhenskaya-Babuška-Brezzi (LBB) inf-sup condition [13–15]. However, the analytical proof to establish LBB-stability is either cumbersome [16] or impossible to accomplish for distorted finite elements [17], which has led to the development of other approaches that by-pass the inf-sup condition [18,19]. Alternatively, a numerical test to verify the inf-sup condition has been developed [17], which can be readily performed over any finite element discretization. Finite element spaces for the displacement and pressure that pass the numerical (Chapelle-Bathe) inf-sup test are likely to satisfy its analytical counterpart [20]. Displacement-based Galerkin meshfree methods [4,5,21–27] that are based on moving least squares approximants, natural neighbor interpolants, or entropy approximants are also prone to locking. Huerta and Fernández-Méndez [28] have conducted an in-depth study of volumetric locking in the element-free Galerkin (EFG) method. Various remedies have been pursued in the literature to overcome this deficiency—for instance, Dolbow and Belytschko [29] employed reduced integration techniques within a mixed formulation of the EFG method; González et al. [30] enriched the displacement approximation in a mixed natural element formulation; Vidal et al. [31] used pseudo-divergence-free approximants in the EFG to satisfy the incompressibility condition; and the B-bar and enhanced strain methods were introduced in the EFG by Recio et al. [32]. In an effort to depart from background cell integration, stabilized nodal integration [33–37] and stress-point integration schemes [38–40] have also been proposed to overcome numerical integration errors and facilitate large deformation simulations with meshfree methods. These approaches attempt to mimic reduced integration procedures, and have had success in suppressing volumetric locking. Meshfree methods that are based on mixed formulations are also subjected to stability requirements.

The finite element literature is replete with use of mixed formulations and their stability analysis for incompressible media problems (for example, see Refs. [41, 42]). The performance and comparison among several stabilization procedures for finite elements is provided in Ref. [43]. On the other hand, the study of stability in meshfree mixed formulations is rendered difficult due to the rational form of meshfree basis functions and the

absence of an element structure in the construction of the meshfree approximation. For instance, Dolbow and Belytschko [29] and De and Bathe [44] emphasize the difficulty in obtaining an analytical proof to the inf-sup condition and in passing the inf-sup test. A stable meshfree formulation for incompressible media based on mixed formulations is, in general, an outstanding issue in meshfree methods. A few instances of meshfree methods that violate the LBB condition have also been developed within the framework of stabilized methods [45–47].

In this dissertation, a new formulation for meshfree methods that provides a remedy for volumetric locking in the incompressible limit is presented. A *volume-averaged* nodal technique is proposed, which allows to solve for nodal pressure variables in the pressure (divergence-free) constraint of a displacement/pressure formulation. As a result, the nodal pressure variables are explicitly written in terms of the displacement field. The latter is used to eliminate the pressure field from the analysis in the equilibrium constraint. A displacement-based formulation is yielded. Even though the proposed approach shares common features with the method proposed by Krysl and Zhu [48], there exist notable differences. We use averages of strain matrices from the elements attached to a particular node to satisfy the near-incompressibility constraint in the weak form, whereas in Ref. [48] the averages are used to obtain a strain field that satisfies a kinematic constraint in a displacement-based weak form. Additionally, Krysl and Zhu [48] formulate their method in a nodal integration framework for finite elements, whereas in this work numerical integration is tailored for meshfree basis functions using Gauss quadrature. Finally, the stability of the proposed method is demonstrated via various inf-sup tests and optimal convergence in energy- and L^2-norms is established.

In traditional finite element methods, mesh topology is one of the key ingredients towards an accurate solution. Ideally, metrics tolerances should be satisfied by the element topology in order to be valid for a finite element computation [49]. Examples of metrics are: relative size, element shape and maximum angle [50, 51]. A mechanism that precludes the ability of a mesh to comply with these metrics is called mesh distortion. Mesh dis-

tortion can arise in several ways. One instance is related to the mesh generation itself in which slivers, poor shapes or small element sizes appear. Another instance occurs when the continuum undergoes large deformations. In the latter case, the elements distort too much resulting in elements with high aspect ratio. Due to the maturity of mesh generators, the aforementioned metrics are easily accomplished in two dimensions. However, in three dimensions, especially in complex three-dimensional domains, some of these metrics are still difficult to achieve and other techniques have to be employed in order to improve the mesh quality such as mesh smoothing and mesh modification [49]. Due to the latter, it has been recognized that the easiest way to generate a mesh in complicated geometries is by means of an unstructured tessellation of triangles or tetrahedra, which has attracted the attention of many researchers using techniques such as advancing front [52–54] and Delaunay triangulation [55–58]. Moreover, low-order triangles or tetrahedra are preferred because their simplicity facilitates remeshing either for mesh refinement or mesh improving techniques [49].

An added difficulty for finite elements is the modeling of near-incompressible solids that undergo large deformations. In this setting, finite elements must deal not only with the volumetric locking issue but also with mesh distortions. Several procedures have been devised to overcome the former difficulty in large deformation analysis and can be grouped within mixed methods and displacement-based methods. Most popular techniques in the former are mixed variational methods of Simo et al. [59], enhanced assumed strain methods of Simo and Armero [60] and the mixed u-p formulation of Sussman and Bathe [61]. On the other hand, a series of 'improved' displacement-based methods have also been developed. Noteworthy methods in the latter category are the geometrically nonlinear version of B-bar projection method [62] and the F-bar method of de Souza Neto et al. [63]. Recently, two novel methods for near-incompressible analysis at finite strain have emerged. The first one corresponds to a class of mixed finite elements that establishes a special topology called *diamond element* [64] that in conjunction with a suitable choice of finite element spaces for both displacement and pressure fields guarantees the satisfaction of the inf-sup condition

with an optimal convergent solution. The second one is a projection method that was devised for NURBS-based isogeometric analysis [12], which reveals superior accuracy in the presence of extreme mesh distortions [65].

In the past few years, there has been great interest for using low-order finite element meshes, particularly in three-dimensional analysis, because they facilitate the mesh generation of complex domains. However, it is well-known that low-order triangles or tetrahedra are not suitable for practical use due to their poor performance in instances such as bending dominated problems, incompressible media and large deformations. In an effort to cope with this poor performance of low-order tessellations, various techniques have been developed especially in large deformation analysis of near-incompressible solids. These techniques can be classified in four approaches: mixed-enhanced elements [66–68], pressure stabilization [69–71], composite pressure fields [72–74], and average nodal pressure/strains [48, 75–79]. The last two approaches are broadly based on the idea of reducing pressure (dilatational) constraints to alleviate volumetric locking.

Contrary to finite elements, meshfree methods are constructed based upon basis functions that possess larger supports and do not rely on a mesh for their definition. This confers meshfree methods some degree of insensitivity to mesh distortions. However, a background mesh is still required in Galerkin meshfree methods to perform the numerical integration of the weak form integrals. The mesh need not comply with the metrics previously discussed as long as enough neighbors (nodes) are contributing at a given Gauss point evaluation as to reproduce the consistency of the approximation required by the weak form—typically linear in a second-order partial differential equation [80]. In principle, any kind of background mesh can be used. In the meshfree method that is developed herein, a background mesh of three-node triangles in two dimensions and four-node tetrahedra in three dimensions, is used.

In nonlinear solid mechanics, a meshfree method that has been utilized to exploit the mesh insensitivity property of meshfree methods is the well-known reproducing kernel particle method (RPKM) [23]. Notwithstanding the many applications of the RPKM and

other meshfree methods in compressible hyperelasticity [81–83], large deformation shear banding [84] and metal forming analyzes [85, 86], most of the meshfree methods that address near-incompressible solids do so by enlarging the support of the basis functions to mimic under-integration [87–89]. However, enlarging supports leads to costly computational times and therefore this kind of technique is in practice avoided [90]. Others have exploited the use of nodal integration [36, 91, 92], which decreases the numbers of Gauss points substantially, hence producing a good balance between displacement degrees of freedom and number of dilatational constraints as to alleviate locking. On the other hand, few applications have been documented in meshfree methods using methodologies that were especially designed for finite elements. For instance, in Refs. [93, 94] mixed u-p formulations were employed for near-incompressible hyperelasticity in the natural element method (NEM) and the meshless local Petrov-Galerkin (MLPG) method, respectively, whereas in Ref. [95] the F-bar method of de Souza Neto et al. [63] was adapted for the element-free Galerkin (EFG) method. Among the existing meshfree methodologies, it appears that the only attempt to exploit the meshfree character to design procedures that can efficiently deal with the incompressibility constraint is the pressure projection method of Ref. [90]. However, the aforementioned method leads to a non-symmetric tangent stiffness matrix which is not consistent with hyperelasticity theory—the continuum problem is symmetric and we would like to preserve that symmetry. Additionally, a non-symmetric tangent stiffness matrix in implicit solvers needs twice the memory and is twice slower than a solver for symmetric matrices. Therefore, an effective meshfree methodology suitable not only for large deformations but also for modeling incompressible media is at present an open topic.

In this dissertation, new methodologies for meshfree analysis of two-dimensional nonlinear elastic solids are presented with a two-fold aim: firstly, the development of a method for large deformations analysis with low-order background (integration) meshes, namely, three-node triangles; and secondly, the design of a numerical procedure where the meshfree character is exploited to prevent volumetric locking in the near-incompressible limit. To these ends, the nonlinear version of the *volume-averaged* nodal technique is developed. The

formulation so devised leads to a displacement-based method that exhibits some commonalities with the F-bar-Patch method of Ref. [96] and the isogeometric F-bar projection method of Ref. [12], and as such, it can be regarded as an F-bar methodology for meshfree methods.

Traditionally, numerical integration of the weak form in meshfree methods is carried out using background cells—triangular or quadrilateral elements are typically adopted in two dimensions [22]. Meshfree basis functions are non-polynomial and in addition the support of the basis functions no longer coincides with the union of the background cells that are used in the numerical integration. This leads to inaccuracies in the numerical integration of weak form integrals, and the patch test is not passed to machine precision. In the EFG method, Belytschko et al. [22] used higher-order Gauss quadrature in each background cell, and in a subsequent study by Dolbow and Belytschko [3], integration cells that were aligned with the support of the nodal basis functions were used. Griebel and Schweitzer [97] developed a partition of unity meshfree method by formulating a hierarchical algorithm to construct a nodal cover by partitioning the domain into overlapping hyperrectangular patches using d-dimensional trees. Due to the overlapping nodal patches, a decomposition of the patches into disjoint cells was performed, and these cells were used as the integration domains. A sparse grid quadrature rule based on univariate Gauss-Patterson rules was employed [98]. As a departure from covers that are rectangular, Riker and Holzer [99] recently proposed a partition-of-unity method in which the nodal cover is a combination of simplexes and polygons.

Atluri et al. [100] proposed a methodology to integrate the weak form in the meshless local Petrov-Galerkin method without the need for background cells by using the support of the basis functions as the domain of integration. This approach was adopted and improved upon in the work of De and Bathe [6]. Similar ideas have also been pursued in Refs. [101–104]. With the aim of using anisotropic weight functions with reduced support sizes, Balachandran et al. [105] developed a methodology that automatically confines the basis functions to natural neighbor polygonal regions by means of the Schwarz-Christoffel

mapping. The resulting basis functions are used within a MLS-based meshfree method. Liu and Tu [106] developed an adaptive procedure within individual background cells for meshfree methods. One of the first theoretical studies on the influence of numerical quadrature errors in meshfree methods was recently put forth by Babuška et al. [107]. Schembri et al. [108] compare the performance of different meshfree approximation schemes in three-dimensional computations.

In this dissertation, a new numerical integration scheme for Galerkin meshfree methods is proposed. On appealing to assumed strain methods [11] and nodal integration techniques [34–36], a modified strain tensor is defined. Maximum-entropy basis functions [27,109] are used in its discretization, and Gauss quadrature is adopted in the numerical integration. The procedure so devised alleviates numerical integration errors in meshfree methods and ensures patch test satisfaction to within machine precision. An added feature of the numerical integration scheme is that fewer number of Gauss points than in standard Gauss quadrature are required to accurately compute the weak form integrals.

Parts of this dissertation are published. Chapter 4 has led to two articles. One is already published [110] and the other one is to appear [111]. Ref. [112], which is based on Chapter 5, is currently in preparation.

1.2 Original Contributions

Because mesh generation is eased in complex geometries, three-node triangle and four-node tetrahedron, are highly desirable in finite element analysis. However, due to mesh distortion issues and very 'stiff' solutions that are delivered when finite element shape functions are used in the analysis of near-incompressible media, these type of meshes are rarely employed. The formulation of an effective methodology for simulation of near-incompressible media problems with low-order finite element meshes is one of the main contributions in this dissertation. Although the elemental structure of the mesh is not used to construct the meshfree approximation, it is used for computation of the numerical integration of the

weak form in the meshfree method. Accurate solutions are obtained, which enable the use of these low-order meshes in practical applications in near-incompressible elasticity at small and finite strains. The meshfree method developed in this dissertation should allow even larger deformations than those achieved by F-bar methodologies for finite elements. However, this remains to be assessed.

Numerical integration errors are important issues in meshfree methods. As previously discussed, many attempts have been made to improve the accuracy of the numerical integration in meshfree methods. However, very expensive techniques have resulted, which impact the computational cost. The development of a numerical integration scheme that alleviates integration errors in meshfree methods with minimal number of Gauss points is another key contribution in this dissertation. A modified strain tensor is proposed to obtain an accurate numerical integration technique. This results in a correction to the stiffness matrix that alleviates integration errors in meshfree methods and patch test is met to within machine precision. In this dissertation, maximum-entropy basis functions are used, but the generality of the proposed numerical integration scheme renders it applicable to any method, not necessarily meshfree, that is able to use a background mesh of triangles or tetrahedra. For instance, the element-free Galerkin (EFG) method [22], the natural element method (NEM) [4] and polygonal finite element interpolants [113] can be adopted.

1.3 Dissertation Outline

The remainder of this dissertation is organized as follows. In Chapter 2, a summary of meshfree methods is presented. A historical background is provided. Distinct ways to construct meshfree methods with their respective features are also presented. The remainder of Chapter 2 is devoted to specific issues in meshfree methods.

Chapter 3 focuses on maximum-entropy approximation. A description of the *principle of maximum entropy* and its link to the linear approximation problem are presented. Details on the construction of maximum-entropy basis functions are elaborated in the rest of

Chapter 3.

The formulation of the maximum-entropy meshfree method for linear elastic media is presented in Chapter 4. It focuses on both compressible and near-incompressible behavior. An accurate numerical integration scheme for meshfree methods is developed. A novel meshfree formulation for near-incompressible media along with theoretical background for numerical stability is also presented. The accuracy and performance of the maximum-entropy meshfree method is studied using two- and three-dimensional structured and unstructured background meshes by means of various benchmark problems, which include problems with homogeneous deformation (patch tests), bending dominated problems, rigid indentation, Stokes flow and numerical stability tests. Wherever appropriate, the maximum-entropy solutions are compared to analytical solutions and to a finite element solution.

Chapter 5 is devoted to the formulation of the maximum-entropy meshfree method for near-incompressible nonlinear elasticity in two dimensions. A novel meshfree formulation for near-incompressible elastic solids at finite strains is presented. The performance of the maximum-entropy meshfree method in large deformation analysis with near-incompressible behavior is investigated. Structured and unstructured triangular background meshes are employed in three benchmark problems: nonlinear Cook's membrane, plane strain compression of a rubber block, and a frictionless indentation problem. In all the problems, the maximum-entropy solution is compared to two finite element solutions that use a mesh of three-node triangles.

In Chapter 6, a summary of the main results and findings of this dissertation are presented, with some concluding remarks on the potential of maximum-entropy meshfree method to solve incompressible media problems. Some thoughts on future work are also provided.

Chapter 2

Meshfree Methods in Computational Mechanics

In this chapter, a summary of meshfree methods is provided. We start by presenting a historical background on the evolution of meshfree methods since their inception to recent developments. A discussion on distinct ways to construct meshfree methods along with their respective features is then provided. We close this chapter discussing some of the main issues of meshfree methods with remarks on possible cures that have been pursued.

2.1 Historical Background

Meshfree methods are relatively new numerical techniques compared to finite elements. In a nutshell, what characterizes *meshfree* or *meshless* methods is that the construction of basis (or shape) functions depends only on the nodal coordinates and no mesh definition is indeed employed to this objective. The first recognized meshfree method was developed in 1977 under the name of *smoothed particle hydrodynamics* (SPH) [114,115] to model astrophysical phenomena such as galaxy and star formation, stellar collision, and gravity currents [116–121]. Over the years, SPH has gained increasing interest in a wide range of applications such as metal impact [122–125], wave impact [126–128], steel penetration [125,129,130], and

metal forming analysis [131, 132]. The success of SPH method in modeling astrophysical phenomena without a explicit mesh has led to the development of several meshfree methods with the aim of overcoming drawbacks of mesh-based methods. Some of the shortcomings of mesh-based methods such as standard finite elements are encountered, for instance, in the modeling of explosion and penetration problems. In this type of problems the continuum is broken into small fragments which would imply breakage of finite elements or the use of adaptive/refinement mesh techniques to accurately capture the transformation of the continuum into small pieces. Either way is difficult since, on one hand, a discontinuity can not be embedded in a standard finite element, and on the other hand, adaptive/refinement mesh techniques, apart from being a formidable task in complicated geometries, imply mapping of states variables from one mesh to another, which introduces numerical error in the solution. Another problem that presents difficulties for finite elements is the modeling of phenomena that require higher-order interpolation fields, which is the case for plates and shells simulations, and gradient theory of plasticity. The applicability of finite elements is limited in this type of problems since constructing C^1 finite element interpolants is non-trivial [7]. One of the main applications in which meshfree methods have shown promise over finite elements is in the modeling of phenomena involving large deformations [81–85, 87–90, 93–95]. Distorted finite elements have a tendency to breakdown the computation very early with the accuracy of the solution being lost, whereas meshfree basis functions do not depend on the mesh and as such are less sensitive to mesh distortions.

In the realm of difficulties for finite elements, meshfree methods have therefore emerged as an alternative to finite elements. Although after the invention of SPH method other meshfree methods such as *generalized finite difference method* (GFDM) [133] and *meshfree collocation method* (MCM) [134] have been devised, it has been recognized that most of the advances in meshfree methods were done in the 1990s with the introduction of the *diffuse element method* (DEM) [21] in 1992 and a posterior improvement, which was termed as *element-free Galerkin method* (EFG) in the seminal work of Belytschko et al. [22] in 1994. The list began to increase with the introduction of other meshfree methods such

as the *reproducing kernel particle method* (RKPM) [23] and the *natural element method* (NEM) [135] in 1995; the *partition of unity method* (PUM) [136, 137], the *finite point method* (FPM) [138] and the *h-p cloud* method [139] in 1996; the *meshless local Petrov-Galerkin* (MLPG) method [5] in 1998; the *method of finite spheres* (MFS) [26] in 2000, and so on. This list is by no means exhaustive. A detailed overview of meshfree methods is provided in Refs. [2, 140, 141]. Due to the mesh-independence of meshfree basis functions, greater flexibility for constructing meshfree methods is realized. Meshfree methods can be formulated starting from a strong form or starting from a weak form, or from a combination of both.

2.2 Strong-Form Meshfree Methods

Strong-form meshfree methods are formulated starting from a boundary-value problem. Since in a boundary-value problem only derivatives appear, there is no need for numerical integration. However, the consistency of the approximation is 'strong' in the sense that it must satisfy up to the order of the highest derivative—second-order consistency for solid mechanics. A strong-form numerical approximation implies that the boundary value problem is satisfied only at the nodes of a domain of discretization, which is refer to as collocation. One of the drawback of meshfree collocation techniques is that they suffer from instabilities due to the ill-conditioned moment matrix that arises in the process of function approximation and the need to satisfy the derivative boundary conditions of the PDE. Additionally, they usually lead to unsymmetric matrices. However, they are easier to implement than meshfree methods obtained from a weak form. Some examples of strong-form meshfree methods are the *generalized finite difference method* (GFDM) [133], the *smoothed particle hydrodynamics* (SPH) [114,115], the *meshfree collocation method* (MCM) [134] and the *finite point method* (FPM) [138].

2.3 Weak-Form Meshfree Methods

Weak-form meshfree methods are obtained by 'weakening' the consistency imposed by the strong form over the approximation. To this end, the PDE is satisfied in an average sense by converting it to an integral form using a variational principle or a weighted residual method. This leads to two function definitions. The trial function, which describes the approximation, and the test function, which acts as the weighting function in the integral form. If a weighted residual method is used, integration by parts needs to be done in order to obtain the final weak form expression. In contrast to strong forms, the surface integral that appears in the weak form provides a natural way to satisfy the derivative boundary conditions at no additional cost.

Since integrals are present in a weak form, numerical integration is required. Thus, in meshfree methods that are formulated from weak forms, a quadrature mesh (also referred to as background mesh) is needed to compute the weak form integrals. However, the basis function definition does not depend on the quadrature mesh. In other words, the mesh is only used to sample the basis functions at the integration points. As long as the numerical integration is done accurately and the space for the approximation is correctly chosen, weak-form meshfree methods (and also finite elements) are stable formulations. However, due to the need for numerical integration, the implementation is more involved than in strong-form meshfree methods.

Weak forms offer many attractive ways to formulate numerical procedures depending on the selection of the trial and test functions. For instance, if trial and test functions are chosen to be the same, *Galerkin methods* are obtained. Most meshfree methods are based on a Galerkin method. Some examples of Galerkin-based meshfree methods are the *element free Galerkin method* (EFG) [22], the *reproducing kernel particle method* (RKPM) [23], the *natural element method* (NEM) [4], and the method of finite spheres (MFS) [26]. The method developed in this dissertation belongs to this category. On the other hand, if trial and test functions are chosen differently, *Petrov-Galerkin methods* are obtained. The

meshless local Petrov-Galerkin (MLPG) method [5] is a representative one in this category.

2.4 Weak-Strong Form Meshfree Methods

As the name suggests, weak-strong form meshfree methods are obtained from a combination of weak and strong forms. In this type of methods, the strong form formulation is used everywhere except at those nodes that are on or near boundaries with derivative boundary conditions. Instead, a weak form formulation is used at those nodes. The latter choice is to prevent instabilities stemming from derivatives boundary conditions. Since the weak form is employed in a limited region of the domain, the use of background cells for numerical integration is minimal. Weak-Strong form were introduced by Liu and Gu [142] for problems in two-dimensional solids and further extended to incompressible fluids [143].

2.5 Issues in Meshfree Methods

As previously pointed out, meshfree methods are an attractive alternative to overcome issues that are related to the dependency of the finite element interpolation on a well defined element topology. However, meshfree methods have their shortcomings. The understanding of these shortcomings combined with the understanding of possibilities that strong forms and weak forms offer for the development of meshfree formulations are of vital importance in the success of a meshfree methodology. The main shortcomings are summarized next.

2.5.1 Issues in Strong-Form Meshfree Methods

The instability of the discrete equations is the main issue related to strong-form meshfree methods. The instability stems from two sources. The singularity of the moment matrix that arises from the function approximation and the large errors introduced by the derivative boundary condition. The former occurs when the nodes that are selected to construct the approximation of a function (usually a field variable) at a given point in the domain

are not correctly chosen or are not sufficient in number. For instance, the polynomial basis $p = \{a_0, a_1x, a_2y\}$ provides a linearly-independent basis for a first-order approximation in two dimensions. In order to find the unknown coefficients a_0, a_1 and a_2, three conditions are exactly needed. One can provide these three conditions by approximating a field variable u at three nodes of the discretized domain. Proceeding likewise results in the linear system of equations $u_n = a_0 + a_1x_n + a_2y_n$ (n=1,2,3), where the coefficients represent nodal field variables and (x_n, y_n) are the coordinates of node n. The singularity in this system of equations can appear in two ways. Firstly, the procedure to find the three nodes might not actually find all of them, resulting in an undetermined system of equations. Secondly, the three nodes selected might not produce a linearly-independent system of equations. For instance, the latter might occur if two nodes are collinear, again resulting in an undetermined system of equations. However, this source of instability is a minor issue since there are efficient methods to overcome it. For instance, the use of weighted least square method [144], the use of radial basis functions [134] and the use of the matrix triangularization algorithm [145], are frequently adopted in the formulation of strong-form meshfree methods. The use of maximum-entropy basis functions would also provide a way to overcome this issue if a procedure to construct higher-order maximum-entropy basis functions is developed. On the other hand, the derivative boundary condition is the critical issue in strong-form meshfree methods [146], since differentiation is a roughening operator that magnifies errors in the approximation. Therefore, any error in the numerical approximation of the derivative boundary conditions might introduce large numerical error in the discrete equations resulting in an ill-conditioned system that needs some form of stabilization to be usable. Ways for stabilization have been studied in strong-form meshfree methods. For instance, the use of additional derivative variables to enforce the derivative boundary conditions [147], the addition of higher-order differential terms in the strong form equations [148, 149] and the use of weak-strong form meshfree methods [142, 143], are usually employed to formulate stable strong-form meshfree methods.

2.5.2 Issues in Weak-Form Meshfree Methods

Two main issues are present in weak-form meshfree methods. The non-zero contribution of basis functions of interior nodes on the boundary and the errors in the numerical integration. The former emanates from the fact that most meshfree basis functions lack the Kronecker-delta property, and therefore they do not interpolate the field variables. Moreover, it has a direct impact on the imposition of essential boundary conditions since the weak form demands their exact satisfaction by requiring basis functions to vanish on the boundary. The consequence in violating this is that essential boundary conditions can not be imposed directly at the nodes as in finite elements[1], and special techniques have to be considered to impose them. Among techniques to impose essential boundary conditions, Nitsche's method and blending technique of Huerta and Fernández-Méndez [150] are most efficient. Maximum-entropy basis functions offer an elegant means to solve this problem since by construction the vanishing property is readily obtained on convex boundaries, which is sufficient to impose essential boundary condition directly at the nodes [27]. However, this property is lost in non-convex domains. Radial point interpolation basis functions [151] provide another means to directly impose essential boundary conditions at the nodes. On the other hand, numerical integration errors is the critical issue in weak-form meshfree methods, which is understood as follows. Meshfree basis functions are non-polynomial and in addition the support of basis functions does not coincide with the union of the background cells that are employed in the numerical integration—triangular or quadrilateral elements are typically adopted in two dimensions [22]. This leads to inaccuracies in the numerical integration of weak form integrals, and patch test is not passed to machine precision. Whether or not to pass the patch test exactly is not an issue per se. However, the importance of ensuring sufficient accuracy in the numerical integration is that its error is not larger than the error of the approximation. This can be evidenced in the patch test. Many attempts have been pursued in order to reduce the integration error in weak-from

[1]Finite element shape functions meet the vanishing requirement very easily since they possess Kronecker-delta property which automatically implies vanishing of interior basis functions on the boundary.

meshfree methods. The adoption of higher-order Gauss quadrature rule has been suggested to overcome this issue partially [3]. Another option that has been pursued by many is the construction of background cells that coincide with the support of the basis functions [3,5,6, 152]. Neither procedure is efficient since considerable number of Gauss points to achieve an adequate accuracy is implied, especially in three-dimensional computations. In an attempt to reduce the burden of adopting many Gauss points, nodal integration techniques that use the nodes as the Gauss points have been devised [34, 36]. However, numerical instabilities are present in these methods, which require further attention. A promising technique that uses smoothing operators in the construction of the strain field is proposed in this dissertation.

Chapter 3

Maximum-Entropy Approximation

This chapter focuses on maximum-entropy approximation. We start by providing some insights on the linear completeness concept along with standard ways of constructing linearly-complete meshfree approximations. A description of the *principle of maximum entropy* is provided and its link to the linear approximation problem is presented. Details on the construction of maximum-entropy basis functions are elaborated towards the end of this chapter.

3.1 Linear Completeness

Linear completeness is the ability of an approximant to exactly reproduce constant and linear field variables (also known as zeroth and firth-order consistency, respectively). In order for a numerical method that is based on the weak form of a second-order partial differential equation to converge, approximants that possess linear completeness are sufficient [80]. Meshfree basis functions are sought such that completeness is obtained by construction. A standard procedure to construct basis functions with a desired completeness order was briefly described in Section 2.5.1. More details are presented here. Consider a continuous field function $u(\mathbf{x})$ defined in a domain Ω, which is represented by a set of field nodes. The approximation of the field variable $u(\mathbf{x})$ at a point with coordinates $\mathbf{x} = \{x, y\}$ in Ω, is

obtained as follows:

$$u(\mathbf{x}) = \sum_{i=1}^{m} p_i(\mathbf{x}) a_i = \begin{bmatrix} p_1(\mathbf{x}) & p_2(\mathbf{x}) & \dots & p_m(\mathbf{x}) \end{bmatrix} \begin{bmatrix} a_1 \\ a_2 \\ \vdots \\ a_m \end{bmatrix} = \mathbf{p}^{\mathrm{T}} \mathbf{a}, \tag{3.1}$$

where $p_i(\mathbf{x})$ is a monomial of a polynomial basis, and a_i is the coefficient for $p_i(\mathbf{x})$. In two dimensions, a linear polynomial basis is

$$\mathbf{p}^{\mathrm{T}} = \begin{bmatrix} 1 & x & y \end{bmatrix}. \tag{3.2}$$

If the approximation (3.1) is required to pass through n nodes of the domain Ω with the polynomial basis (3.2) being used, the following system of equations is obtained:

$$\begin{bmatrix} u_1 \\ \vdots \\ u_n \end{bmatrix} = \begin{bmatrix} 1 & x_1 & y_1 \\ \dots & \dots & \dots \\ 1 & x_n & y_n \end{bmatrix} \begin{bmatrix} a_1 \\ a_2 \\ a_3 \end{bmatrix} = \mathbf{P}_m \mathbf{a}. \tag{3.3}$$

It is evident that if $n = 3$ in (3.3), the system is square and, provided is not singular, a unique set of nodal coefficients a_i can be obtained as a result of the linear approximation procedure as

$$\mathbf{a} = \mathbf{P}_m^{-1} \mathbf{u}. \tag{3.4}$$

The basis functions ϕ_i ($i = \{1, 2, ..., n\}$) are then computed on substituting (3.4) back into (3.1) as follows:

$$u(\mathbf{x}) = \mathbf{p}^{\mathrm{T}} \mathbf{P}_m^{-1} \mathbf{u} \equiv \sum_{i=1}^{n} \phi_i u_i = \mathbf{\Phi}^{\mathrm{T}}(\mathbf{x}) \mathbf{u}. \tag{3.5}$$

However, if $n > 3$, the system (3.3) is undetermined with non-unique solution. Some mesh-free methods construct basis functions imposing that $n = m$ such that a square system is obtained. Doing that has the shortcoming, however, that the nodes entering the ap-

proximation procedure have to be correctly selected as to obtain a non-singular system (see Section 2.5.1). Procedures that are related to optimization theory can be adopted to compute basis functions when $n > m$. Among these procedures, *moving least squares* [144] and the *principle of maximum entropy* [153] are two possibilities.

In order to interpret the linear approximation problem under the *maximum entropy* formalism to be introduced in the next section, the linear approximation problem in two dimensions is rewritten as

$$\begin{bmatrix} 1 & 1 & \cdots & 1 \\ x_1 & x_2 & \cdots & x_n \\ y_1 & y_2 & \cdots & y_n \end{bmatrix} \begin{bmatrix} \phi_1 \\ \phi_2 \\ \vdots \\ \phi_n \end{bmatrix} = \begin{bmatrix} 1 \\ x \\ y \end{bmatrix}, \tag{3.6}$$

where the basis functions ϕ_i $(i = \{1, 2, ..., n\})$ are now directly obtained as the solution of (3.6). Note that similar to (3.3), the system (3.6) is also undetermined if $n > 3$.

3.2 Principle of Maximum Entropy

In this section, the construction of linearly-complete basis functions is linked to the *principle of maximum entropy*. Consider a set of n discrete events $\{x_1, \ldots, x_n\}$. The possibility of each event is $p_a = p(x_a) \in [0, 1]$ with uncertainty $-\ln p_a$. The Shannon-entropy [154] $H(p) = -\sum_{a=1}^{n} p_a \ln p_a$ is the amount of uncertainty represented by the distribution $\{p_1, \ldots, p_n\}$. Based on the Shannon-entropy, Jaynes [153] postulated that solving the optimization problem (*principle of maximum entropy*):

$$\max_{p \in \mathbb{R}_+^n} -\sum_{a=1}^{n} p_a \ln p_a, \tag{3.7a}$$

subject to the constraints:

$$\sum_{a=1}^{n} p_a = 1, \quad \sum_{a=1}^{n} p_a g_r(x_a) =< g_r(x) >, \tag{3.7b}$$

yields the least-biased probability distribution and the one that has the most likelihood to occur. In (3.7), $\mathbb{R}^n_+$ is the non-negative orthant and $< g_r(x) >$ is the expectation of the function $g_r(x)$. On considering the constraints of the max-ent problem as the only information available for a set of n discrete probabilities (n usually larger than the number of constraints), the *principle of maximum entropy* provides a rationale means for least-biased statistical inference when insufficient information is available.

The optimization problem (3.7) assigns probabilities to every p_a in the set. Assume now that the probability p_a has an initial guess w_a known as a *prior*, which reduces its uncertainty to $-\ln p_a + \ln w_a = -\ln(p_a/w_a)$. An alternative problem can be formulated on using this *prior* in (3.7) (*principle of minimum relative entropy* [155, 156]):

$$\max_{p \in \mathbb{R}^n_+} -\sum_{a=1}^{n} p_a \ln\left(\frac{p_a}{w_a}\right), \tag{3.8a}$$

subject to the constraints:

$$\sum_{a=1}^{n} p_a = 1, \quad \sum_{a=1}^{n} p_a g_r(x_a) =< g_r(x) > . \tag{3.8b}$$

Depending upon the *prior* employed, the optimization problem (3.8) may assign probabilities to a selected number of p_a in the set. It can be easily seen that if the *prior* is constant, the Shannon-Jaynes entropy functional (3.7) is recovered as a particular case. The max-ent approach is demonstrated next by means of two dice experiments.

Example 3.2.1. A fair dice is thrown. The set of possible outcomes are the events $\{1, 2, 3, 4, 5, 6\}$. Since the dice is fair, we infer that all the events have equal possibility

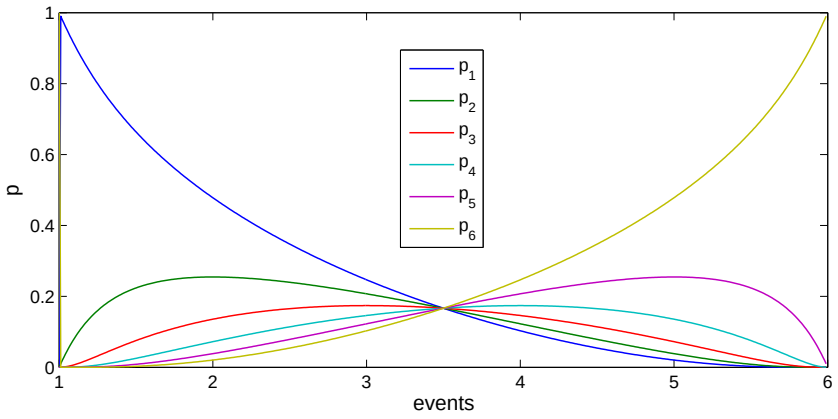

Figure 3.1: Throwing a fair dice. If the dice is fair, max-ent assigns equal possibilities to all events.

1/6 of being the outcome. Taking the expectation of the outcome yields:

$$E = \frac{1}{6} \cdot 1 + \frac{1}{6} \cdot 2 + \frac{1}{6} \cdot 3 + \frac{1}{6} \cdot 4 + \frac{1}{6} \cdot 5 + \frac{1}{6} \cdot 6 = 3.5.$$

If this expectation is viewed as the constraint in the max-ent problem (3.7), the set of possibilities previously inferred is exactly predicted by max-ent. The result is shown in Fig. 3.1.

Example 3.2.2. A biased dice is thrown. The set of possible outcomes are the events $\{1, 2, 3, 4, 5, 6\}$. A guess is made on each outcome via the following set of prior possibilities $w = \{0.1, 0.1, 0.1, 0.1, 0.5, 0.1\}$. On considering these priors, the expectation of the outcome yields:

$$E = 0.1 \cdot 1 + 0.1 \cdot 2 + 0.1 \cdot 3 + 0.1 \cdot 4 + 0.5 \cdot 5 + 0.1 \cdot 6 = 4.1.$$

If this expectation is viewed as the constraint in the max-ent problem (3.8), the set of 'most honest' possibilities assigned by max-ent is $p = \{0.1, 0.1, 0.1, 0.1, 0.5, 0.1\}$, which is exactly the guess, as expected. The result is depicted in Fig. 3.2.

The connection between the *principle of maximum entropy* and the construction of

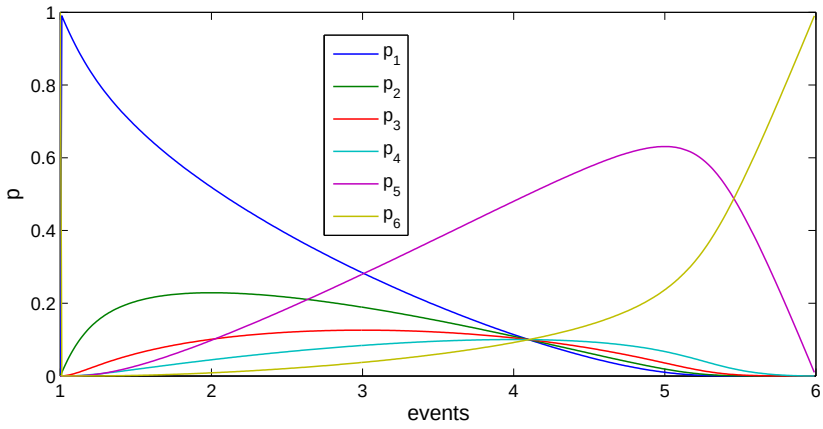

Figure 3.2: Throwing a biased dice. If the dice is biased, max-ent assigns the most probable possibility to each event.

linearly-complete basis functions is now evident: the discrete probabilities and the constraints of the max-ent problem are interpreted as the basis functions and the linear reproducing conditions given in the system (3.6), respectively.

3.3 Maximum-Entropy Basis Functions

As already stated in Section 3.2, basis functions are viewed as discrete probabilities satisfying the max-ent constraints. The connection between maximum-entropy basis functions and linearly-complete approximations was established by Sukumar [157]. In Ref. [157], the principle of maximum entropy was employed to obtain linearly-complete interpolants on polygonal domains. Arroyo and Ortiz [27] realized a meshfree approximation using a modified entropy functional—with emphasis on establishing a smooth transition between finite element and meshfree methods. Sukumar and Wright [109] generalized the construction of max-ent meshfree basis functions by using the relative (Shannon-Jaynes) entropy functional with a prior [155, 156]. On using compactly-supported prior functions that are at least C^0, compactly-supported max-ent basis functions are realized. In particular, when a Gaussian prior is employed the approach of Arroyo and Ortiz [27] is recovered. Maximum-

entropy basis functions are obtained from a convex optimization problem and are endowed with the following attributes [27]: variation diminishing property; positive-definite mass matrices and weak Kronecker-delta property on the boundary. The last property is noteworthy since it enables the direct imposition of essential boundary conditions as in finite elements[1]. Recently, new applications of max-ent meshfree basis functions have emerged: barycentric coordinates for arbitrary polytopes are developed in Ref. [158], co-rotational formulation is presented in Ref. [159], second-order max-ent approximants are proposed in Refs. [160, 161], fluid and plastic flows are studied in Ref. [162], and stable meshfree methods for fluid mechanics are developed in Refs. [163, 164].

The approach in Ref. [109] is now followed to present expressions for max-ent basis functions and their derivatives. To this end, let the prior function be denoted by $w_a(\mathbf{x})$. The set of max-ent basis functions $\{\phi_a(\mathbf{x}) \geq 0\}_{a=1}^n$ is obtained via the solution of the following optimization problem:

$$\max_{\boldsymbol{\phi}\in\mathbb{R}^n_+} -\sum_{a=1}^n \phi_a(\mathbf{x}) \ln\left(\frac{\phi_a(\mathbf{x})}{w_a(\mathbf{x})}\right), \tag{3.9a}$$

subject to the linear reproducing conditions:

$$\sum_{a=1}^n \phi_a(\mathbf{x}) = 1, \quad \sum_{a=1}^n \phi_a(\mathbf{x})\tilde{\mathbf{x}}_a = \mathbf{0}, \tag{3.9b}$$

where $\tilde{\mathbf{x}}_a = \mathbf{x}_a - \mathbf{x}$ are shifted nodal coordinates and $\mathbb{R}^n_+$ is the non-negative orthant. If $w_a(\mathbf{x})$ is a constant for all a, then the Shannon-Jaynes entropy functional, $-\sum_a \phi_a \ln \phi_a$, is recovered. In practice, any prior function that is compactly-supported and at least C^0-continuous may be used. Typical prior functions are smooth Gaussian radial basis functions [27]

$$w_a(\mathbf{x}) = \exp(-\beta_a \|\mathbf{x}_a - \mathbf{x}\|^2), \tag{3.10a}$$

[1]Most available meshfree basis functions would typically not vanish on the boundary and as such special procedures are needed to enforce essential boundary conditions [140, 141, 150].

and C^2 quartic polynomials [159]

$$w_a(q) = \begin{cases} 1 - 6q^2 + 8q^3 - 3q^4 & 0 \leq q \leq 1, \\ 0 & q > 1. \end{cases} \tag{3.10b}$$

In (3.10a), $\beta_a = \gamma/h_a^2$; γ is a parameter that controls the support-width of the basis function at node a; and h_a is a characteristic nodal spacing that may be distinct for each node a. In n dimensions, h_a is set as the distance to the n-nearest neighbor from node a. For the quartic polynomial, $q = \|\mathbf{x}_a - \mathbf{x}\|/\rho_a$ and $\rho_a = \gamma h_a$ is the radius of the basis function support at node a. In a recent study on max-ent meshfree methods [165], it has been shown that substantial improvements in accuracy are realized by letting the support-width parameters as unknowns and solving for them through the variational structure (minimizing principle) of the continuum problem.

On using the procedure of Lagrange multipliers, the solution of the variational statement (3.9) is [109]:

$$\phi_a(\mathbf{x}) = \frac{Z_a(\mathbf{x};\boldsymbol{\lambda}^*)}{Z(\mathbf{x};\boldsymbol{\lambda}^*)}, \quad Z_a(\mathbf{x};\boldsymbol{\lambda}^*) = w_a(\mathbf{x}) \exp(-\boldsymbol{\lambda}^* \cdot \tilde{\mathbf{x}}_a), \tag{3.11}$$

where the partition function $Z(\mathbf{x};\boldsymbol{\lambda}^*) = \sum_b Z_b(\mathbf{x};\boldsymbol{\lambda}^*)$, and in three dimensions $\tilde{\mathbf{x}}_a = [\tilde{x}_a \ \tilde{y}_a \ \tilde{z}_a]^{\mathrm{T}}$ and $\boldsymbol{\lambda}^* = [\lambda_1^* \ \lambda_2^* \ \lambda_3^*]^{\mathrm{T}}$. In (3.11), the Lagrange multiplier vector $\boldsymbol{\lambda}^*$ is the minimizer of the dual of the optimization problem posed in (3.9)

$$\boldsymbol{\lambda}^* = \arg \min_{\boldsymbol{\lambda} \in \mathbb{R}^3} \ln Z(\mathbf{x};\boldsymbol{\lambda}), \tag{3.12}$$

which gives rise to the following system of nonlinear equations:

$$\mathbf{r}(\mathbf{x};\boldsymbol{\lambda}) = \nabla_{\boldsymbol{\lambda}} \ln Z(\mathbf{x};\boldsymbol{\lambda}) = -\sum_a^n \phi_a(\mathbf{x}) \tilde{\mathbf{x}}_a = \mathbf{0}, \tag{3.13}$$

where $\nabla_{\boldsymbol{\lambda}}$ stands for the gradient with respect to $\boldsymbol{\lambda}$.

The gradient of max-ent basis functions is needed to complete the derivation. To this end, we use the converged value of $\boldsymbol{\lambda}^*$ and rewrite (3.11) as follows:

$$\phi_a(\mathbf{x}) = \frac{\exp\left[f_a(\mathbf{x};\boldsymbol{\lambda}^*)\right]}{\sum_b \exp\left[f_b(\mathbf{x};\boldsymbol{\lambda}^*)\right]}, \quad f_a(\mathbf{x};\boldsymbol{\lambda}^*) = \ln w_a(\mathbf{x}) - \boldsymbol{\lambda}^* \cdot \tilde{\mathbf{x}}_a. \tag{3.14}$$

Taking the gradient of ϕ_a in the above expression yields

$$\nabla\phi_a = \phi_a \left(\nabla f_a - \sum_{b=1}^{n} \phi_b \nabla f_b \right). \tag{3.15}$$

Next, we use f_a given in (3.14) and take its gradient to obtain

$$\nabla f_a = \frac{\nabla w_a}{w_a} + \boldsymbol{\lambda}^* - \tilde{\mathbf{x}}_a \cdot \nabla\boldsymbol{\lambda}^*, \tag{3.16}$$

which needs the gradient of $\boldsymbol{\lambda}^*$. In order to find the latter, we take the total derivative of (3.13), which vanishes for $\boldsymbol{\lambda}^*$:

$$D\mathbf{r} = \nabla\mathbf{r} + \nabla_{\boldsymbol{\lambda}}\mathbf{r} \cdot \nabla\boldsymbol{\lambda}^* = \mathbf{0}, \tag{3.17}$$

where $\nabla\mathbf{r}$ is the gradient of $\mathbf{r}$ taken with $\boldsymbol{\lambda}$ fixed. Proceeding likewise in (3.13) and noting that $\nabla_{\boldsymbol{\lambda}}\mathbf{r}$ is the Hessian of $\ln Z$, (3.17) leads to

$$\nabla\boldsymbol{\lambda}^* = \mathbf{H}^{-1}\left(\mathbf{A} - \mathbf{I}\right), \quad \mathbf{H} = \sum_{b=1}^{n} \phi_b \tilde{\mathbf{x}}_b \otimes \tilde{\mathbf{x}}_b, \quad \mathbf{A} = \sum_{b=1}^{n} \phi_b \tilde{\mathbf{x}}_b \otimes \frac{\nabla w_b}{w_b}, \tag{3.18}$$

and therefore ∇f_a in (3.16) becomes

$$\nabla f_a = \frac{\nabla w_a}{w_a} + \boldsymbol{\lambda}^* + \tilde{\mathbf{x}}_a \cdot \left[(\mathbf{H})^{-1} - (\mathbf{H})^{-1} \cdot \mathbf{A}\right]. \tag{3.19}$$

Using the above expression for ∇f_a in (3.15) yields the final expression for the gradient of

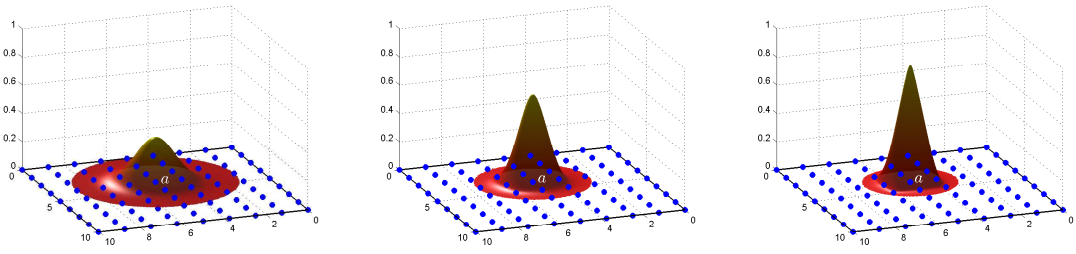

(a) (b) (c)

Figure 3.3: Plots of a maximum-entropy basis function computed with a Gaussian prior for three values of γ. Note that the locality of the basis function is affected but it always vanishes on the boundary. (a) $\gamma = 1$; (b) $\gamma = 2$; and (c) $\gamma = 3$.

ϕ_a [159]:

$$\nabla\phi_a = \phi_a \left\{ \tilde{\mathbf{x}}_a \cdot \left[(\mathbf{H})^{-1} - (\mathbf{H})^{-1} \cdot \mathbf{A} \right] + \frac{\nabla w_a}{w_a} - \sum_{b=1}^{n} \phi_b \frac{\nabla w_b}{w_b} \right\}. \tag{3.20}$$

In Fig. 3.3, plots of a max-ent basis function computed with a Gaussian prior for various support-width parameter γ are illustrated for two dimensions. For $\gamma = 2$, plots of the Gaussian prior and the corresponding max-ent basis function along with their derivatives are shown in Fig. 3.4. For the Gaussian prior, (3.20a) reduces to [27]

$$\nabla\phi_a = \phi_a \mathbf{H}^{-1} \cdot \tilde{\mathbf{x}}_a. \tag{3.21}$$

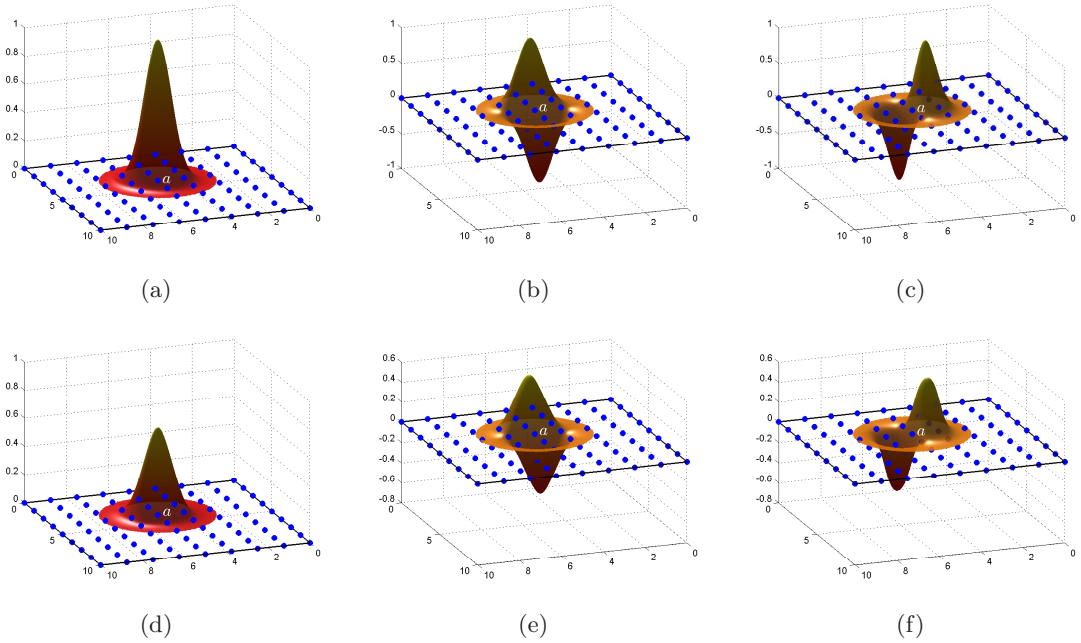

Figure 3.4: Plots of Gaussian prior ($\gamma = 2$) and maximum-entropy basis function and their derivatives for node a. Note that $w_a(\mathbf{x}_a) = 1$, but $\phi_a(\mathbf{x}_a) \neq 1$, and hence the interior basis function ϕ_a does not satisfy the Kronecker-delta property. The smoothness of the basis function and its derivatives are inherited from the Gaussian prior. (a) Gaussian prior, w_a; (b) $\partial w_a/\partial x$; (c) $\partial w_a/\partial y$; (d) ϕ_a; (e) $\partial \phi_a/\partial x$; and (f) $\partial \phi_a/\partial y$.

Chapter 4

Maximum-Entropy Meshfree Method for Linear Elastic Media

In this chapter, the formulation of the maximum-entropy meshfree method for linear elastic media is presented. Both compressible and near-incompressible behavior are considered. A novel meshfree formulation for near-incompressible media along with theoretical background for its numerical stability is presented. The development of an accurate numerical integration technique for meshfree methods that alleviates integration errors with guaranteed patch test satisfaction is also presented. The accuracy and performance of the maximum-entropy meshfree method is studied using two- and three-dimensional structured and unstructured background meshes by means of various benchmark problems, which include patch tests, bending dominated problem, combined bending-shear problem, rigid indentation, Stokes flow and numerical stability tests.

4.1 Governing Equations and Variational Formulation

4.1.1 Strong Form

Consider a body defined by an open bounded domain $\Omega \subset \mathbb{R}^n$ ($n = \{2, 3\}$) with boundary Γ such that $\Gamma = \Gamma_u \cup \Gamma_t$ and $\Gamma_u \cap \Gamma_t = \emptyset$. A nearly-incompressible isotropic linear elastic solid or fluid under static loads and no body force is governed by the following equations [7]:

$$\boldsymbol{\nabla} \cdot \boldsymbol{\sigma} = 0 \quad \text{in } \Omega, \tag{4.1a}$$

$$\boldsymbol{\nabla} \cdot \mathbf{u} + \frac{p}{\eta} = 0 \quad \text{in } \Omega, \tag{4.1b}$$

and the following essential (displacement or velocity) and natural (traction) boundary conditions imposed on Γ_u and Γ_t, respectively:

$$\mathbf{u} = \bar{\mathbf{u}} \quad \text{on } \Gamma_u, \tag{4.1c}$$

$$\boldsymbol{\sigma} \cdot \mathbf{n} = \bar{\mathbf{t}} \quad \text{on } \Gamma_t, \tag{4.1d}$$

where the Cauchy stress tensor $\boldsymbol{\sigma}$ is related to the strain tensor $\boldsymbol{\varepsilon}$ and the pressure parameter p by the following isotropic linear elastic constitutive relation:

$$\boldsymbol{\sigma}(\mathbf{u}, p) = -p\mathbf{I} + 2\mu\boldsymbol{\varepsilon}(\mathbf{u}). \tag{4.1e}$$

In (4.1) η and μ are identified with the first and second Lamé parameters of the solid:

$$\eta = \lambda = \frac{\nu E}{(1+\nu)(1-2\nu)}, \quad \mu = \frac{E}{2(1+\nu)}, \tag{4.2}$$

respectively, where ν is the Poisson's ratio and E is the Young's modulus of the material. If the continuum is a fluid, the Lamé parameters in (4.2) stand for a penalty parameter and the dynamic viscosity, respectively. The penalty parameter is usually taken as $\eta \sim 10^7\mu$ [7]. The kinematic relation between the strain tensor $\boldsymbol{\varepsilon}$ and the displacement or velocity vector

$\mathbf{u}$ is:

$$\boldsymbol{\varepsilon} = \frac{1}{2}\left[\mathbf{u} \otimes \boldsymbol{\nabla} + \boldsymbol{\nabla} \otimes \mathbf{u}\right]. \tag{4.3}$$

4.1.2 Weak Form

For Galerkin-based mixed formulations with $\mathbf{u}, \mathbf{v}$ as the trial and test displacement (or velocity) functions, and p, q as the trial and test hydrostatic pressure functions, the weak form of (4.1) (with (4.1e) substituted) reads [7]:

Find $\mathbf{u} \in \mathscr{U}$ and $p \in \mathscr{P}$ such that

$$a(\mathbf{u}, \mathbf{v}) - b(p, \mathbf{v}) = (\mathbf{t}, \mathbf{v}) \quad \forall \mathbf{v} \in \mathscr{V}, \tag{4.4a}$$

$$b(q, \mathbf{u}) + \frac{1}{\eta}(p, q) = 0 \quad \forall q \in \mathscr{P}, \tag{4.4b}$$

where $\mathscr{U} \subset \mathbf{H}^1(\Omega)$ is the Sobolev space of functions with square-integrable first derivatives in Ω, $\mathscr{V} \equiv \mathbf{H}^1_0(\Omega)$ is the Sobolev space of functions with square-integrable first derivatives in Ω and vanishing values on the essential boundary Γ_u, and $\mathscr{P} \equiv \mathbb{H}^0_0(\Omega) = L^2_0(\Omega)$ is the Sobolev space of square-integrable functions with zero mean. The bilinear forms $a(\cdot, \cdot)$ and $b(\cdot, \cdot)$ are given by

$$a(\mathbf{u}, \mathbf{v}) = 2\mu \int_\Omega \boldsymbol{\varepsilon}(\mathbf{u}) : \boldsymbol{\varepsilon}(\mathbf{v})\, d\Omega, \tag{4.4c}$$

$$b(q, \mathbf{v}) = \int_\Omega q \boldsymbol{\nabla} \cdot \mathbf{v}\, d\Omega, \tag{4.4d}$$

whereas the linear form $(\mathbf{t}, \cdot)$ is

$$(\mathbf{t}, \mathbf{v}) = \int_{\Gamma_t} \mathbf{t} \cdot \mathbf{v}\, d\Gamma. \tag{4.4e}$$

4.2 Modified Gauss Integration

As in finite element methods, numerical integration is used in meshfree methods to evaluate the weak form integrals that appear in (4.4). Typically, the support of meshfree basis functions is greater than the support of finite element basis functions, which lends flexibility to meshfree methods and often leads to improved accuracy. However, this has its consequences: with polynomial finite element basis functions whose support includes the union of triangles or tetrahedra, appropriate Gauss quadrature rules can be selected to ensure accurate and optimally convergent finite element solutions. In meshfree methods, these properties are lost, and hence use of standard Gauss quadrature to evaluate (4.4) leads to errors in the numerical integration. The integration issue in meshfree methods that use background cells for integration is well-documented in Ref. [3]. It can be understood due to the following characteristic of meshfree basis functions. Meshfree basis functions are rational (non-polynomial) functions and their support do not coincide with the union of background cells that are employed in the numerical integration. When performing numerical integration of the weak form, a multiplication of the form $\mathbf{B}_a^{\mathrm{T}}\mathbf{C}\mathbf{B}_b$[1] arises. This in turn leads to multiplication between basis function derivatives (for instance, $\phi_{a,x}\phi_{b,y}$) whose support is the intersection of the support of ϕ_a and ϕ_b and as such can differ appreciably from the union of the cells used in the numerical integration. As a consequence, significant numerical errors can be expected from the numerical integration using the standard strain tensor. To overcome this deficiency in existing meshfree methods, a numerical integration scheme that alleviates the aforementioned errors and ensures patch test satisfaction to within machine precision, is devised. To this end, the following modification to the strain tensor in a certain background finite element cell is proposed:

$$\hat{\boldsymbol{\varepsilon}} = \boldsymbol{\varepsilon} - \bar{\boldsymbol{\varepsilon}} + \bar{\bar{\boldsymbol{\varepsilon}}}, \tag{4.5}$$

[1] $\mathbf{B}_a$ is the nodal strain matrix and $\mathbf{C}$ is the matrix stemming from the material constitutive relation.

where $\hat{\boldsymbol{\varepsilon}}$ bears resemblance to an assumed strain [11], which is referred to as the *modified strain*. The rest of the terms in (4.5) are defined next. $\boldsymbol{\varepsilon}$ is the standard small strain tensor, $\bar{\boldsymbol{\varepsilon}}$ is the volume average strain tensor over the background cell, and $\bar{\bar{\boldsymbol{\varepsilon}}}$ corresponds to $\bar{\boldsymbol{\varepsilon}}$ written as a surface integral by means of Green's theorem. The corresponding equations are

$$\boldsymbol{\varepsilon} = \frac{1}{2}\left[\mathbf{u} \otimes \boldsymbol{\nabla} + \boldsymbol{\nabla} \otimes \mathbf{u}\right], \tag{4.6a}$$

$$\bar{\boldsymbol{\varepsilon}} = \frac{1}{V^e}\int_{\Omega^e} \boldsymbol{\varepsilon}\, d\Omega, \tag{4.6b}$$

$$\bar{\bar{\boldsymbol{\varepsilon}}} = \frac{1}{V^e}\int_{\Gamma^e} \frac{1}{2}\left[\mathbf{u} \otimes \mathbf{n} + \mathbf{n} \otimes \mathbf{u}\right]\, d\Gamma. \tag{4.6c}$$

In the numerical examples that are presented in this dissertation, the integral in (4.6b) is referred to as the *volume integral* and the integral in (4.6c) as the *surface integral*. When linearly complete finite elements are used, (4.6b) and (4.6c) yield the same result with $\bar{\boldsymbol{\varepsilon}} = \bar{\bar{\boldsymbol{\varepsilon}}}$, and the small strain tensor is recovered. However, for meshfree basis functions $\bar{\boldsymbol{\varepsilon}} \neq \bar{\bar{\boldsymbol{\varepsilon}}}$, in general. The latter observation allows one to see $\bar{\boldsymbol{\varepsilon}} - \bar{\bar{\boldsymbol{\varepsilon}}}$ as a correction that is introduced into the stiffness matrix such that the integration error is reduced when the same Gauss quadrature rule is employed to integrate $\boldsymbol{\varepsilon}$ as well as $\bar{\boldsymbol{\varepsilon}}$. It is pertinent to mention here that the strain in the form of (4.6b) and (4.6c) has been previously used in nodal integration schemes [34–36], which in part has motivated the definition of the modified strain via (4.5).

On using n-point Gauss quadrature in the numerical integration of the weak form integrals, the evaluation of $\hat{\boldsymbol{\varepsilon}}$ will be required at each of these Gauss points $\mathbf{x}_k$, namely

$$\hat{\boldsymbol{\varepsilon}}(\mathbf{x}_k) = \boldsymbol{\varepsilon}(\mathbf{x}_k) - \bar{\boldsymbol{\varepsilon}}(\mathbf{x}_k) + \bar{\bar{\boldsymbol{\varepsilon}}}(\mathbf{x}_k). \tag{4.7}$$

Since $\bar{\boldsymbol{\varepsilon}}$ and $\bar{\bar{\boldsymbol{\varepsilon}}}$ are integral expressions over the background cell where numerical integration is carried out, it follows that for each $\mathbf{x}_k$ of the n-point evaluations, these integrals must also be computed using numerical integration[2].

[2]Note that $\bar{\boldsymbol{\varepsilon}}$ and $\bar{\bar{\boldsymbol{\varepsilon}}}$ are constants within each background cell, and hence are pre-computed.

A further step that will be useful for later discretization of the weak form (4.4) is to discretize the modified strain (4.5). For this, the following discretization for the displacement (or velocity) over a background mesh of triangles or tetrahedra is considered:

$$\mathbf{u}_h(\mathbf{x}) = \sum_{a=1}^{N} \phi_a(\mathbf{x})\mathbf{u}_a, \tag{4.8}$$

where $N = \{3, 4\}$, $\mathbf{u}_h \in \mathscr{U}_h \in \mathscr{U}$; ϕ_a are max-ent basis functions. On substituting (4.8) into (4.5) leads to the following strain matrices:

$$\hat{\mathbf{B}}_a(\mathbf{x}) = \mathbf{B}_a(\mathbf{x}) - \bar{\mathbf{B}}_a + \bar{\bar{\mathbf{B}}}_a, \tag{4.9a}$$

where in two dimensions

$$\mathbf{B}_a(\mathbf{x}) = \begin{bmatrix} \phi_{a,x} & 0 \\ 0 & \phi_{a,y} \\ \phi_{a,y} & \phi_{a,x} \end{bmatrix}, \tag{4.9b}$$

or in three dimensions

$$\mathbf{B}_a(\mathbf{x}) = \begin{bmatrix} \phi_{a,x} & 0 & 0 \\ 0 & \phi_{a,y} & 0 \\ 0 & 0 & \phi_{a,z} \\ \phi_{a,y} & \phi_{a,x} & 0 \\ \phi_{a,z} & 0 & \phi_{a,x} \\ 0 & \phi_{a,z} & \phi_{a,y} \end{bmatrix}. \tag{4.9c}$$

is the standard strain matrix. In two and three dimensions

$$\bar{\mathbf{B}}_a = \sum_{p=1}^{n} \mathbf{B}_a(\mathbf{x}_p) w_p, \tag{4.9d}$$

whereas in two dimensions

$$\bar{\bar{\mathbf{B}}}_a = \frac{1}{A^e} \sum_{L=1}^{3} \left\{ \sum_{r=1}^{m} \bar{\bar{\mathbf{N}}}_a(\xi_r) |J(\xi_r)| w_r \right\}, \tag{4.9e}$$

$$\bar{\bar{\mathbf{N}}}_a(\xi_r) = \begin{bmatrix} \phi_a n_x & 0 \\ 0 & \phi_a n_y \\ \phi_a n_y & \phi_a n_x \end{bmatrix}, \tag{4.9f}$$

or in three dimensions

$$\bar{\bar{\mathbf{B}}}_a = \frac{1}{V^e} \sum_{L=1}^{4} \left\{ \sum_{r=1}^{m} \bar{\bar{\mathbf{N}}}_a(\mathbf{x}_r) w_r \right\} A^L, \tag{4.9g}$$

$$\bar{\bar{\mathbf{N}}}_a(\mathbf{x}_p) = \begin{bmatrix} \phi_a n_x & 0 & 0 \\ 0 & \phi_a n_y & 0 \\ 0 & 0 & \phi_a n_z \\ \phi_a n_y & \phi_a n_x & 0 \\ \phi_a n_z & 0 & \phi_a n_x \\ 0 & \phi_a n_z & \phi_a n_y \end{bmatrix}. \tag{4.9h}$$

In two as well as three dimensions, $\bar{\bar{\mathbf{N}}}_a$ is evaluated along the boundary of the element with n_i $(i = \{x, y, z\})$ as the i-component of the unit outward normal to the cell's edge. Note that when $\bar{\mathbf{B}}_a - \bar{\bar{\mathbf{B}}}_a = 0$, the standard strain matrix $\mathbf{B}_a$ is recovered.

As a last remark on the modified Gauss integration scheme, we point out that the integration order is preserved and the integration error is minimized when the same Gauss quadrature rule is used to integrate $\boldsymbol{\varepsilon}$ as well as $\bar{\boldsymbol{\varepsilon}}$. When the strain is a constant, which occurs in the patch test, machine precision accuracy is realized. To prove the foregoing, it suffices to show that the nodal forces at all interior nodes (whose basis function support

vanish on the boundary) are identically equal to zero for a uniform stress field $\boldsymbol{\sigma} = \boldsymbol{\sigma}^c$, i.e.,

$$\mathbf{f}_a = \sum_e \int_{\Omega^e} \hat{\mathbf{B}}_a^{\mathrm{T}} \boldsymbol{\sigma}^c \, d\Omega = \mathbf{0} \tag{4.10}$$

is to be established, where the assembly is over all elements e that have a non-zero intersection with the support of ϕ_a. The proof follows.

Proof. On using (4.9), $\mathbf{f}_a$ can be expressed as

$$\mathbf{f}_a = \sum_e \int_{\Omega^e} \left[\mathbf{B}_a^T(\mathbf{x}) - \sum_{p=1}^{n} \mathbf{B}_a^T(\mathbf{x}_p) w_p + \bar{\bar{\mathbf{B}}}_a^T \right] \boldsymbol{\sigma}^c \, d\Omega.$$

On performing numerical integration using n-point Gauss quadrature within the element, the following is obtained:

$$\mathbf{f}_a = \sum_e \sum_{q=1}^{n} \left[\mathbf{B}_a^T(\mathbf{x}_q) w_q - \left(\sum_{p=1}^{n} \mathbf{B}_a^T(\mathbf{x}_p) w_p \right) w_q + \bar{\bar{\mathbf{B}}}_a^T w_q \right] A^e \boldsymbol{\sigma}^c,$$

which simplifies to

$$\mathbf{f}_a = \sum_e \sum_{q=1}^{n} \bar{\bar{\mathbf{B}}}_a^T A^e w_q \boldsymbol{\sigma}^c,$$

since the first two terms cancel because $\sum_{q=1}^{n} w_q = 1$ (Gauss weights sum to unity). For the sake of simplicity, the two-dimensional expression for $\bar{\bar{\mathbf{B}}}_a$ given in (4.9e) are used to write

$$\mathbf{f}_a = \sum_e \sum_{q=1}^{n} \sum_{L=1}^{3} \left\{ \sum_{r=1}^{m} \bar{\bar{\mathbf{N}}}_a^T(\xi_r) |J(\xi_r)| w_r \right\} w_q \boldsymbol{\sigma}^c.$$

Now, closer inspection of the above equation and the expression for $\bar{\bar{N}}_a$ given in (4.9f) reveals that contribution along an interior edge L will arise from two adjacent triangles with common edge L. However, since the normal vector on the edge will assume equal magnitude but opposite signs for the two cases, the two contributions cancel each other. Proceeding likewise, the net contribution to $\mathbf{f}_a$ from all interior edges vanishes, and hence (4.10) is

satisfied. □ □

4.3 Discrete System and MEM implementation

In the derivations of this section, the strain matrices resulted from the modified strain already developed in Section 4.2 are employed.

4.3.1 Discrete Weak Form

The objective is to obtain a formulation solely in terms of the primary variable $\mathbf{u}$. To this end, the pressure field is written in terms of nodal pressure values that are obtained by volume-averaging of the divergence-free constraint in a neighborhood of a given node. This procedure has been previously adopted in finite element and meshfree studies [48,75,76,78]. Consider the following discretizations for the displacement (or velocity) and pressure (trial and test functions) over a background mesh of triangles or tetrahedra:

$$\mathbf{u}_h(\mathbf{x}) = \sum_{a=1}^{N} \phi_a(\mathbf{x})\mathbf{u}_a,\ \mathbf{v}_h(\mathbf{x}) = \sum_{a=1}^{N} \phi_a(\mathbf{x})\mathbf{v}_a, \tag{4.11a}$$

$$p_h(\mathbf{x}) = \sum_{a=1}^{N} N_a(\mathbf{x})p_a,\ q_h(\mathbf{x}) = \sum_{a=1}^{N} N_a(\mathbf{x})q_a, \tag{4.11b}$$

where $N = \{3, 4\}$, $\mathbf{u}_h \in \mathscr{U}_h \in \mathscr{U}$ and $p_h \in \mathscr{P}_h \in \mathscr{P}$; ϕ_a are max-ent basis functions and N_a are standard finite element shape functions[3]. In order to ensure stability of the solution [7], the displacement approximation is enhanced with an extra displacement node in the interior of each triangle or tetrahedra. This approach is similar to the use of nodal bubble shape functions in finite element methods [166,167], even though in the present case the max-ent basis function of the interior node does not necessarily vanish on the boundary of the element. See Ref. [168] for a related study on meshfree methods involving bubble functions. On substituting (4.11) into the weak form (4.4b) and relying on the arbitrariness

[3]Note that since the derivative of the pressure does not appear in the weak form, there is no need to use meshfree basis functions and hence finite element shape functions are adopted in the discretization of the pressure.

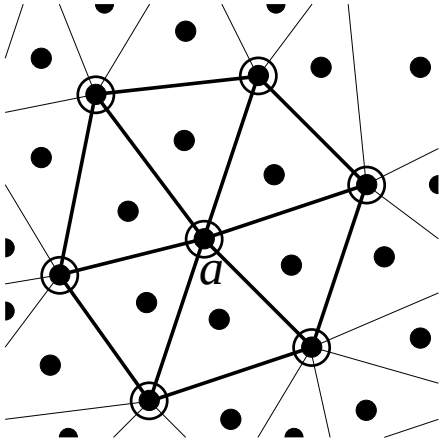

Figure 4.1: Mesh to compute volume-averaged nodal pressure around a representative node a. Filled black circles represent displacement or velocity nodes and open circles are for pressure nodes.

of nodal pressure test functions yields

$$\sum_{b=1}^{N} \int_{\Omega} N_a \mathbf{m}^{\mathrm{T}} \hat{\mathbf{B}}_b \mathbf{u}_b \, d\Omega + \frac{1}{\eta} \sum_{b=1}^{N} \int_{\Omega} N_a N_b p_b \, d\Omega = 0, \tag{4.12}$$

and performing row-sum in the pressure term leads to

$$\sum_{b=1}^{N} \left\{ \int_{\Omega} N_a \mathbf{m}^{\mathrm{T}} \hat{\mathbf{B}}_b \, d\Omega \right\} \mathbf{u}_b + \left\{ \frac{1}{\eta} \int_{\Omega} N_a \, d\Omega \right\} p_a = 0. \tag{4.13}$$

Now, solving for p_a in (4.13), the following *volume-averaged nodal pressure* is obtained:

$$p_a = -\eta \sum_{b=1}^{N} \left\{ \frac{\int_{\bar{\Omega}} N_a \mathbf{m}^{\mathrm{T}} \hat{\mathbf{B}}_b \, d\Omega}{\int_{\bar{\Omega}} N_a \, d\Omega} \right\} \mathbf{u}_b, \tag{4.14}$$

where $\mathbf{m}^{\mathrm{T}} = [1\ 1\ 0]$ in two dimensions or $\mathbf{m}^{\mathrm{T}} = [1\ 1\ 1\ 0\ 0\ 0]$ in three dimensions. For the purpose of computation of integrals in (4.14), $\bar{\Omega}$ is the union of all the elements attached to node a, i.e., $\bar{\Omega} = \cup \Omega_a^e$. A reference mesh for the method developed in this dissertation is illustrated in Fig. 4.1. In three dimensions, the 3-node triangle is replaced by a 4-node tetrahedron.

Even though the approach here devised shares common features with the method proposed by Krysl and Zhu [48], there exist notable differences. We use averages of strain matrices from the elements attached to a particular node to satisfy the near-incompressibility constraint in the weak form (4.4), whereas in Ref. [48] the averages are used to obtain a strain field that satisfies a kinematic constraint in a displacement-based weak form within a nodal integration scheme.

4.3.2 Discrete System

On substituting (4.11) along with the nodal pressure expression (4.14) into the weak form (4.4a), and appealing to the arbitrariness of nodal test functions, the following discrete system of equations is obtained:

$$\mathbf{K}\mathbf{d} = \mathbf{f}, \tag{4.15a}$$

where $\mathbf{d}$ is the vector of nodal coefficients and

$$\mathbf{K}_{ab} = \int_{\Omega} \hat{\mathbf{B}}_a^{\mathrm{T}} \bar{\mathbf{C}} \hat{\mathbf{B}}_b \, d\Omega - \int_{\Omega} \hat{\mathbf{B}}_a^{\mathrm{T}} \mathbf{m} \left\{ \sum_{c=1}^{3} N_c \mathbf{Q}_{cb} \right\} d\Omega, \tag{4.15b}$$

$$\mathbf{f}_a = \int_{\Gamma_t} \phi_a \bar{\mathbf{t}} \, d\Gamma \tag{4.15c}$$

with

$$\bar{\mathbf{C}} = \begin{bmatrix} 2\mu & 0 & 0 \\ 0 & 2\mu & 0 \\ 0 & 0 & \mu \end{bmatrix} \tag{4.15d}$$

for plane strain or

$$\bar{\mathbf{C}} = \begin{bmatrix} 2\mu & 0 & 0 & 0 & 0 & 0 \\ 0 & 2\mu & 0 & 0 & 0 & 0 \\ 0 & 0 & 2\mu & 0 & 0 & 0 \\ 0 & 0 & 0 & \mu & 0 & 0 \\ 0 & 0 & 0 & 0 & \mu & 0 \\ 0 & 0 & 0 & 0 & 0 & \mu \end{bmatrix} \tag{4.15e}$$

in three dimensions and

$$\mathbf{Q}_{cb} = -\eta \left\{ \frac{\int_{\bar{\Omega}} N_c \mathbf{m}^{\mathrm{T}} \hat{\mathbf{B}}_b \, d\Omega}{\int_{\bar{\Omega}} N_c \, d\Omega} \right\}. \tag{4.15f}$$

Note that only unknowns related to $\mathbf{u}$ appear in the system given in (4.15). The pressure field p can be computed a posteriori from the $\mathbf{u}$ field through (4.14). The numerical evaluation of the integrals appearing in (4.15) is performed over the background mesh of triangles or tetrahedra using Gauss integration with the modified strain matrix $\hat{\mathbf{B}}_a$ that was developed in Section (4.2).

4.3.3 Numerical Integration of the Stiffness Matrix and the External Force Vector

In (4.15), matrix $\mathbf{K}_{ab}$ now appears corrected in terms of the modified strain matrix $\hat{\mathbf{B}}_a$, and is numerically integrated using n-point Gauss quadrature rule. Recall that the same Gauss quadrature rule is used in (4.6b). In particular, for a three-node triangular background cell, the numerical integration of the stiffness matrix disregarding the pressure part is computed as follows:

$$\mathbf{K}_{ab} = \sum_{k=1}^{n} \hat{\mathbf{B}}_a^{\mathrm{T}}(\mathbf{x}_k) \bar{\mathbf{C}} \hat{\mathbf{B}}_b(\mathbf{x}_k) A^e t w_k, \tag{4.16}$$

where A^e is the area of the three-node triangle and t its thickness. In (4.16), indices a and b range over the nodes covered by the intersection of the support of the basis functions contained in $\hat{\mathbf{B}}_a$ and $\hat{\mathbf{B}}_b$. Numerical integration of the external force vector is done as usual with an n-point Gauss quadrature rule.

4.3.4 On the Selection of the Appropriate Gauss Quadrature Rule

The weak form integrals appearing in (4.15) need to be computed with sufficient accuracy to preclude under integration or a rank-deficient stiffness matrix. Due to the interior displacement node that is added inside the triangle or tetrahedra for stability, at least second-order accurate Gauss rule is needed to compute the volume integrals, which is confirmed by the numerical experiments presented in Section 4.5. Using first-order accurate Gauss rule will lead to a rank-deficient stiffness matrix. On the other hand, the computation of the surface integral is not a significant issue since it does not involve basis function derivatives; a second-order accurate scheme is used on each edge. The above-mentioned quadrature rules suffice to pass the patch test to machine precision and to ensure optimal rates of convergence in the energy norm for the proposed meshfree method.

4.4 Inf-Sup Condition and Numerical Inf-Sup Test

Consider the bilinear forms appearing in the weak form (4.4). The optimality and stability of the mixed formulation is guaranteed if the consistency of the approximation, the ellipticity of $a(\cdot,\cdot)$ on the null space of $b(\cdot,\cdot)$ and the LBB inf-sup condition [13–15] on $b(\cdot,\cdot)$ are satisfied [20]. By construction, max-ent basis functions satisfy the linear consistency required by the weak form (4.4). On the other hand, if numerical integration is accurate enough—which is the case herein (see Section 4.2), the ellipticity condition is always met by displacement or velocity-pressure mixed formulations [169]. What remains to be established for the stability of the meshfree formulation is the satisfaction of the inf-sup

condition [13–15]:

$$\inf_{q_h \in \mathbb{H}^0(\Omega)} \sup_{\mathbf{v}_h \in \mathbb{H}^1_0(\Omega)} \frac{\int_\Omega |q_h \boldsymbol{\nabla} \cdot \mathbf{v}_h| \, d\Omega}{\|q_h\|_0 \|\mathbf{v}_h\|_1} = \alpha_h \geq \alpha > 0 \tag{4.17}$$

holds with α a positive constant independent of h. Since in the formulation proposed in this dissertation the pressure field is eliminated by writing it as a function of the displacement (or velocity) field, i.e., $q_h \equiv q_h(\mathbf{w}_h)$, the following equivalent form of the inf-sup condition is useful:

$$\inf_{\mathbf{w}_h \in \mathbb{H}^1_0(\Omega)} \sup_{\mathbf{v}_h \in \mathbb{H}^1_0(\Omega)} \frac{\int_\Omega |q_h(\mathbf{w}_h) \boldsymbol{\nabla} \cdot \mathbf{v}_h| \, d\Omega}{\|q_h(\mathbf{w}_h)\|_0 \|\mathbf{v}_h\|_1} = \alpha_h \geq \alpha > 0. \tag{4.18}$$

An analytical proof to condition in (4.18) is difficult for meshfree methods [29,44]. Instead, it is commonly verified through the numerical inf-sup test [17, 20]. To this end, let us consider the matrix (numerical) form of (4.18), namely

$$\inf_{\mathbf{W}_h} \sup_{\mathbf{V}_h} \frac{\mathbf{W}_h^{\mathrm{T}} \mathbf{G}^h \mathbf{V}_h}{\sqrt{\mathbf{W}_h^{\mathrm{T}} \mathbf{G}^h \mathbf{W}_h} \sqrt{\mathbf{V}_h^{\mathrm{T}} \mathbf{S}^h \mathbf{V}_h}} = \alpha_h \geq \alpha > 0, \tag{4.19}$$

where $\mathbf{W}_h$ and $\mathbf{V}_h$ are vectors corresponding to the nodal displacement or velocity test functions $\mathbf{w}_h$ and $\mathbf{v}_h$ with

$$\|q_h(\mathbf{w}_h)\|_0^2 = \int_\Omega (q_h(\mathbf{w}_h))^2 \, d\Omega = \mathbf{W}_h^{\mathrm{T}} \mathbf{G}^h \mathbf{W}_h, \tag{4.20}$$

and

$$\|\mathbf{v}_h\|_1^2 = \int_\Omega \sum_{i,j=1}^{2} \left(\frac{\partial (\mathbf{v}_h)_i}{\partial x_j} \right)^2 \, d\Omega = \mathbf{V}_h^{\mathrm{T}} \mathbf{S}^h \mathbf{V}_h. \tag{4.21}$$

In the meshfree formulation, matrices $\mathbf{G}^h$ and $\mathbf{S}^h$ in two dimensions are given by

$$\mathbf{G}^h_{ab} = \int_\Omega \hat{\mathbf{B}}^{\mathrm{T}}_a \mathbf{m} \sum_{c=1}^{3} N_c \left\{ \frac{\int_{\bar{\Omega}} N_c \mathbf{m}^{\mathrm{T}} \hat{\mathbf{B}}_b \, d\Omega}{\int_{\bar{\Omega}} N_c \, d\Omega} \right\} d\Omega, \tag{4.22a}$$

$$\mathbf{S}^h_{ab} = \int_\Omega \begin{bmatrix} \phi_{a,x}\phi_{b,x} + \phi_{a,y}\phi_{b,y} & 0 \\ 0 & \phi_{a,x}\phi_{b,x} + \phi_{a,y}\phi_{b,y} \end{bmatrix} d\Omega. \tag{4.22b}$$

The numerical evaluation of the inf-sup value α_h in (4.19) is based on the solution of the following generalized eigenvalue problem, which is computed on a sequence of refined meshes [17, 20]:

$$\mathbf{G}^h \boldsymbol{\psi} = \omega \mathbf{S}^h \boldsymbol{\psi}. \tag{4.23}$$

If the eigenvalues are set in increasing order, then the smallest nonzero eigenvalue ω_k is used to compute the numerical inf-sup value α_h as [17, 20]

$$\alpha_h = \sqrt{\omega_k}, \tag{4.24}$$

provided that there are no spurious pressure modes. The number of pressure modes can be anticipated from [20]

$$k_{pm} = k - (n_u - n_p + 1),$$

where n_u is the number of displacement or velocity degrees of freedom and n_p the number of pressure degrees of freedom. A formulation that passes the inf-sup test must do so with $k_{pm} = 0$ (no pressure modes) or if $k_{pm} > 0$ (constant or spurious pressure modes), the pressure modes must be constant pressure modes as these can be removed by appropriate modification of the essential boundary conditions [16, 20]. Hence, a formulation that is free of spurious pressure modes and does not show a decrease towards a vanishing α_h with mesh refinement is said to pass the inf-sup test. In Section 4.5.8, we show that the inf-sup test is passed by the maximum-entropy meshfree method for several benchmark problems.

4.5 Numerical Results and Discussions

The application of the maximum-entropy meshfree (MEM) method to near-incompressible solids at small strains as well as Stokes flow is presented. The accuracy and performance of the (MEM) method are examined by means of eight benchmark problems: displacement patch test, a cantilever beam subjected to a parabolic end load, Cook's membrane problem, a three-dimensional cantilever beam, a three-dimensional rigid flat punch under frictionless indentation, two-dimensional cavity flow, two-dimensional Poiseuille flow, and various inf-sup tests. Structured background meshes are adopted for all the two-dimensional examples other than inf-sup tests. For the latter, distorted meshes are employed. The performance of the MEM method on unstructured tetrahedral background meshes is assessed in all the three-dimensional examples. We consider the `MINI` [166] element within the standard u-p formulation for near-incompressible solids as a representative finite element that relies on the background mesh employed by the MEM method. The MEM solution is compared to the `MINI` element solution in most of the examples. In the numerical experiments, STD stands for standard Gauss quadrature (i.e., $\bar{\mathbf{B}}_a - \bar{\bar{\mathbf{B}}}_a = 0$) and MOD for the modified integration scheme presented in Section 4.2 (i.e., $\bar{\mathbf{B}}_a - \bar{\bar{\mathbf{B}}}_a \neq 0$). Unless stated otherwise, MOD with a second-order accurate scheme is used for both the volume and surface integrals. In the examples, no explicit unit system is adopted, but consistency of units is assumed.

4.5.1 Displacement Patch Test

Consider the boundary-value problem for a two-dimensional elastic plate under essential boundary conditions:

$$\boldsymbol{\nabla} \cdot \boldsymbol{\sigma} = \mathbf{0} \quad \text{in } \Omega = (0,1)^2,$$

$$u_x(\mathbf{x}) = x \ \text{ on } \Gamma, \quad u_y(\mathbf{x}) = x + y \ \text{ on } \Gamma.$$

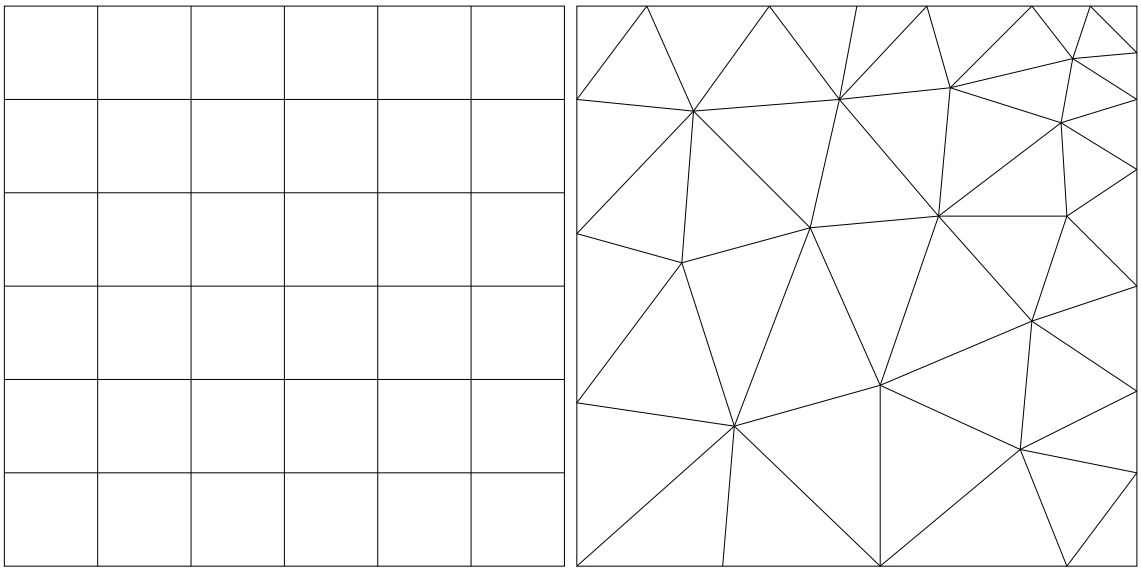

(a) (b)

Figure 4.2: Meshes used for the displacement patch test. (a) Uniform mesh of four-node quadrilaterals (Q4); and (b) Non-uniform mesh of three-node triangles (T3). For the near-incompressible case, nodal degrees of freedom are as shown in Fig. 4.1.

Plane strain conditions are assumed with the following material parameters: $E = 3 \times 10^7$ and $\nu = \{0.3; 0.499\}$. The meshes used in the study are shown in Fig. 4.2: a uniform mesh of four-node quadrilateral elements (Q4) for $\nu = 0.3$, and a non-uniform mesh of three-node triangular elements (T3) for $\nu = \{0.3; 0.499\}$. Both meshes are tested using STD and MOD schemes. Maximum-entropy basis functions are used with a support-width parameter $\gamma = 2.0$ for the Gaussian prior, and $\gamma = 1.5$ for the quartic prior. Numerical results for the relative error in the L^2-norm are shown in Tables 4.1 and 4.2. Different Gauss quadrature rules (number of Gauss points) for the volume integrals are tested (quadrature rule for quadrilateral elements is indicated within braces). Numerical results confirm that patch test satisfaction is met to within machine precision for both compressible and near-incompressible material behavior only when MOD is employed. In this study, max-ent approximants are used, but the generality of the integration approach renders it applicable to other meshfree approximants as well as polygonal finite element interpolants [113].

Table 4.1: Relative error in the L^2-norm for the patch test ($\nu = 0.3$)

Prior	Quadrature	T3 (STD)	T3 (MOD)	Q4 (STD)	Q4 (MOD)
Gaussian	3 (3×3)	1.7×10^{-3}	3.2×10^{-16}	6.4×10^{-6}	1.2×10^{-15}
	6 (6×6)	5.6×10^{-4}	3.1×10^{-16}	1.9×10^{-8}	2.8×10^{-15}
	12 (12×12)	2.9×10^{-4}	3.4×10^{-16}	6.6×10^{-12}	2.5×10^{-15}
Quartic	3 (3×3)	2.6×10^{-3}	2.8×10^{-16}	1.3×10^{-4}	3.2×10^{-16}
	6 (6×6)	3.0×10^{-3}	4.4×10^{-16}	5.6×10^{-7}	9.3×10^{-16}
	12 (12×12)	7.8×10^{-4}	3.6×10^{-16}	1.3×10^{-8}	7.9×10^{-16}

Table 4.2: Relative error in the L^2-norm for the patch test ($\nu = 0.499$)

Prior	Quadrature	T3 (STD)	T3 (MOD)
Gaussian	3	5.4×10^{-1}	8.2×10^{-14}
	6	4.8×10^{-1}	8.8×10^{-14}
	12	4.5×10^{-1}	8.6×10^{-14}
Quartic	3	5.2×10^{-1}	2.6×10^{-13}
	6	3.9×10^{-1}	2.6×10^{-13}
	12	5.1×10^{-1}	6.2×10^{-13}

4.5.2 Cantilever Beam

A cantilever beam of thickness t with a a parabolic end load P (Fig. 4.3(a)) is considered. The displacement solution for compressible ($\nu = 0.3$) and near-incompressible ($\nu = 0.499999$) material behavior with $E = 10^7$ in plane strain condition is sought. Essential boundary conditions on the clamped edge are applied according to the analytical solution given by Timoshenko and Goodier [170]:

$$u_x = \frac{Py}{6\bar{E}I}\left(3x^2 - 6Lx + \bar{\nu}y^2\right) - \frac{Py}{6I\mu}\left(y^2 - \frac{3}{4}D^2\right), \tag{4.26a}$$

$$u_y = \frac{P}{6\bar{E}I}\left(3\bar{\nu}\left(L - x\right)y^2 + 3Lx^2 - x^3\right), \tag{4.26b}$$

Table 4.3: Normalized tip deflection for the cantilever beam (plane strain).

	$u_2^{\text{NUM}}/u_2^{\text{EXACT}}$ at point A			
	Regular mesh		Irregular mesh	
Method	$\nu = 0.3$	$\nu = 0.499999$	$\nu = 0.3$	$\nu = 0.499999$
MINI	0.963	0.969	0.955	0.962
MEM	1.001	0.999	1.001	1.000

where μ is the material shear modulus (Lamé parameter) and

$$\bar{E} = \begin{cases} E & \text{for plane stress} \\ E/\left(1-\nu^2\right) & \text{for plane strain} \end{cases}, \tag{4.27a}$$

$$\bar{\nu} = \begin{cases} \nu & \text{for plane stress} \\ \nu/\left(1-\nu\right) & \text{for plane strain} \end{cases}. \tag{4.27b}$$

In the numerical computations the following parameters are used: $L = 16$, $D = 4$, $t = 1$ and $P = -1$. Two background meshes for the upper half of the beam are studied: a regular mesh of three-node triangles (Fig. 4.3(b)) and an irregular mesh of three-node triangles (Fig. 4.3(c)). Maximum-entropy basis functions are used with a support-width parameter $\gamma = 2.0$ for the Gaussian prior. The numerical solution of the maximum-entropy meshfree method with MOD is compared to the (`MINI` element) solution. Results for the normalized tip deflection are shown in Table 4.3 for both meshes. The numerical and exact solution for the nodal hydrostatic pressure along the fibers of the beam (regular mesh only) are depicted in Fig. 4.4a for the `MINI` element and in Fig. 4.4(b) for the maximum-entropy meshfree method. For the pressure field, the `MINI` element has some oscillations about the analytical solution, whereas the maximum-entropy solution is devoid of oscillations and is in very good agreement with the analytical solution. The convergence study of the normalized tip deflection for the regular mesh is shown in Fig. 4.5 for the `MINI` element and the MEM method. The numerical results indicate that compared to the finite element solution, the MEM solution has better accuracy and converges faster towards the exact tip-deflection.

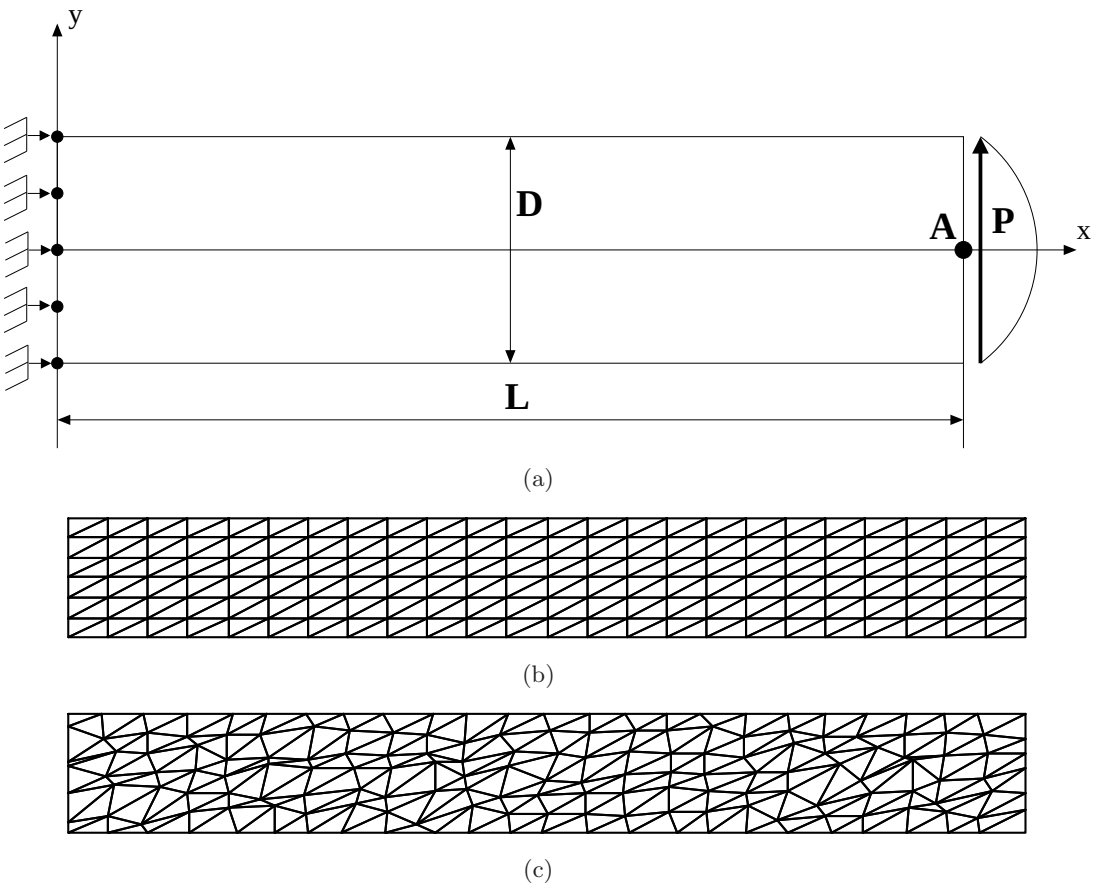

Figure 4.3: Cantilever beam problem. (a) Model geometry and boundary conditions; (b) Regular mesh of three-node triangles; and (c) Irregular mesh of three-node triangles. Unless otherwise stated in the text, nodal degrees of freedom are as shown in Fig. 4.1 for both compressible and near-incompressible elasticity.

To assess the influence of numerical integration, a study of the MEM method with STD and MOD schemes is conducted. The numerical results for $\nu = 0.3$ and $\nu = 0.499999$ are presented in Fig. 4.6. For $\nu = 0.3$, the standard displacement-based max-ent formulation is used with nodes located only at the vertices of the triangles. From the convergence curves in Fig. 4.6(a), we observe that the rate of convergence of STD (with 3-, 6-, and 12-point quadrature) and MOD techniques are in agreement with theory—the energy norm of the error is of $O(h)$. For $\nu = 0.499999$, the nodal-averaged pressure formulation is adopted, and an additional displacement-node is inserted in the middle of every triangle. It is evident from the curves in Fig. 4.6(b) that a 3-point Gauss quadrature is insufficient

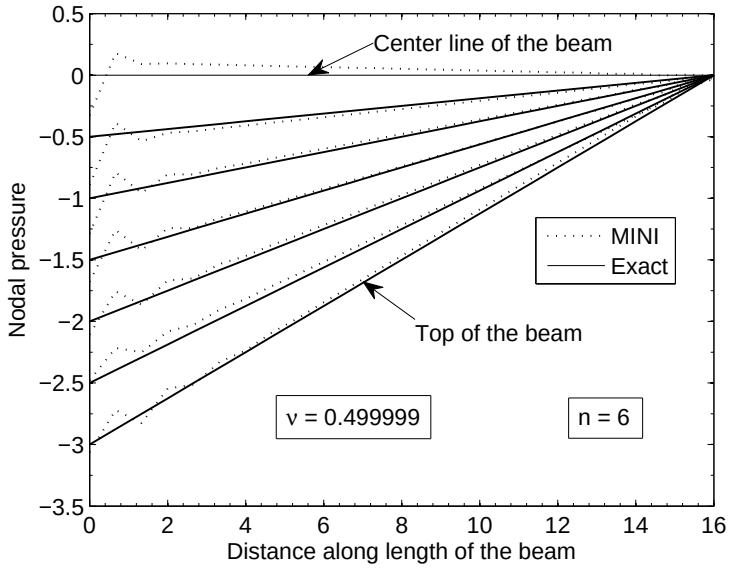

(a)

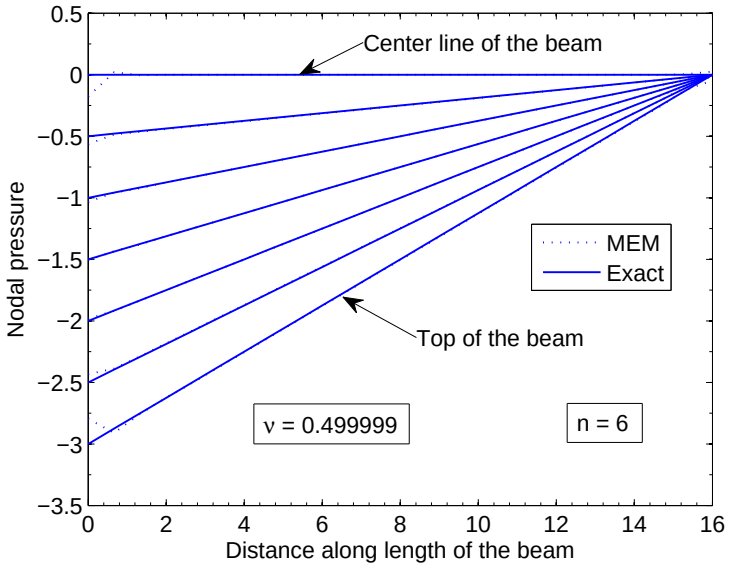

(b)

Figure 4.4: Cantilever beam problem. (a) Nodal pressure for the MINI element; and (b) Nodal pressure for the maximum-entropy meshfree method.

(under-integration leads to lack of convergence), and only with higher-order Gauss quadrature is the convergence rate closer to optimal. This is not surprising, since 3-point and

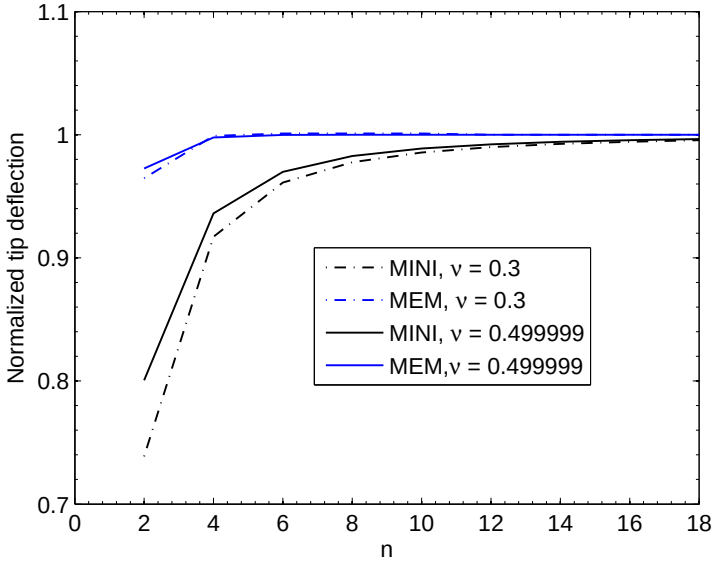

Figure 4.5: Convergence of the normalized tip deflection for the cantilever beam problem. $4n \times n$ (n is the number of divisions along the y-direction) mesh pattern is used on the upper half of the beam.

6-point quadrature rules in a triangle are exact for second-order and fourth-order bivariate polynomials, respectively, but the max-ent basis function for the interior node bears similarity to a cubic bubble function, which renders the integrand of the stiffness matrix to be like a fourth-order bivariate polynomial. Hence, the improved accuracy with 6-point quadrature is realized, with 12-point quadrature being able to deliver about the same accuracy as the modified integration scheme. The numerical results demonstrate the performance of STD and MOD schemes, and establishes that the MOD technique can deliver accurate and optimal convergence in MEM computations.

Lastly, the accuracy and rate of convergence of the `MINI` element and the maximum-entropy meshfree method for two support-width parameters γ are compared in Fig. 4.7. For the Gaussian prior, $\gamma = 2.0$ represents a larger support and $\gamma = 4.0$ a smaller support. From Fig. 4.7, we observe that the max-ent and finite element solutions are accurate and have the optimal rate of convergence in the energy norm for both support sizes.

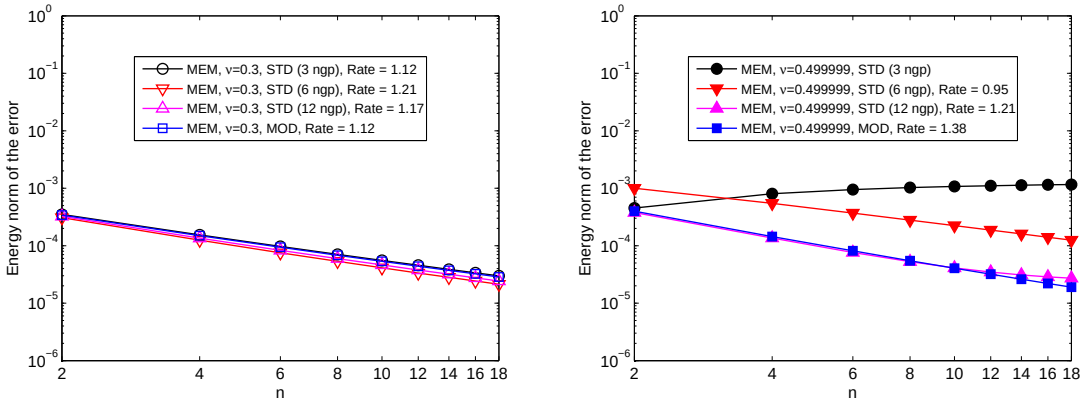

(a) (b)

Figure 4.6: Rate of convergence in energy norm for the cantilever beam problem using standard and modified Gauss integration techniques. (a) $\nu = 0.3$; and (b) $\nu = 0.499999$. $4n \times n$ (n is the number of divisions along the y-direction) mesh pattern is used on the upper half of the beam.

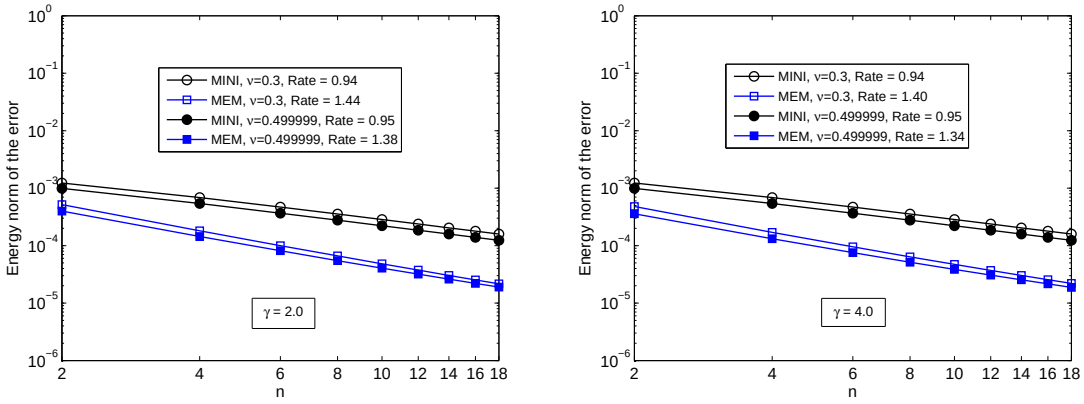

(a) (b)

Figure 4.7: Rate of convergence in energy norm for the cantilever beam problem for two support-width parameters. (a) $\gamma = 2.0$; and (b) $\gamma = 4.0$. $4n \times n$ (n is the number of divisions along the y-direction) mesh pattern is used on the upper half of the beam.

4.5.3 Cook's Membrane

The model geometry and boundary conditions for the Cook's membrane problem is shown in Fig. 4.8(a). This standard benchmark problem is suitable to test the behavior of the near-incompressible formulation under combined bending and shear (see for instance, Refs. [10,

64, 96]). The left edge is clamped and the right end is subjected to a shear load $F = 6.25$ per unit length (total shear load of 100). The following material parameters are considered: $E = 250$ and $\nu = 0.4999$. A regular mesh of three-node triangles is used with a mesh pattern of $n \times n$ divisions per side. A reference mesh for $n = 6$ is shown in Fig. 4.8(b). Maximum-entropy basis functions are used with a support-width parameter $\gamma = 2.0$ for the Gaussian prior. The numerical solution of the maximum-entropy meshfree method with MOD is compared to the `MINI` element solution. The convergence study of the vertical tip displacement at point A upon mesh refinement is shown in Fig. 4.8(c) for both the `MINI` element and the maximum-entropy meshfree method. Numerical results indicate that the max-ent solution has a faster convergence in the vertical tip displacement vis-à-vis the `MINI` element solution. It is also observed that the `MINI` element produces oscillations in the hydrostatic pressure field, whereas the maximum-entropy pressure field is smooth.

4.5.4 Three-Dimensional Cantilever Beam

In this example, a three-dimensional cantilever beam subjected to an end load is studied to establish the robustness of the maximum-entropy meshfree method in bending problems. The geometry, boundary and loading conditions are depicted in Fig. 4.9(a). The tetrahedral background mesh used in this example is illustrated in Fig. 4.9(b). The geometry and loading parameters are set as follows: $L = 21$, $H = 4$, $W = 6$ and $P = 50000$. The following material parameters are considered: $E = 200000$ and $\nu = 0.4999$. We focus on the tip deflection at point A of the beam whose exact solution is -21.11, as well as on the smoothness of the pressure field. The analysis is conducted for the `MINI` element and the MEM method. In the latter case, the MOD integration technique is used. The corresponding numerical solutions are shown in Figs. 4.10(a) and 4.10(b) for the `MINI` element, whereas Figs. 4.10(c) and 4.10(d) depict the solutions for the MEM method. We note that the maximum-entropy solution is proximal to the exact one, whereas the `MINI` element solution behaves somewhat 'stiff' on the same mesh. Additionally, a smoother pressure field is observed in the maximum-entropy meshfree method than in the `MINI`

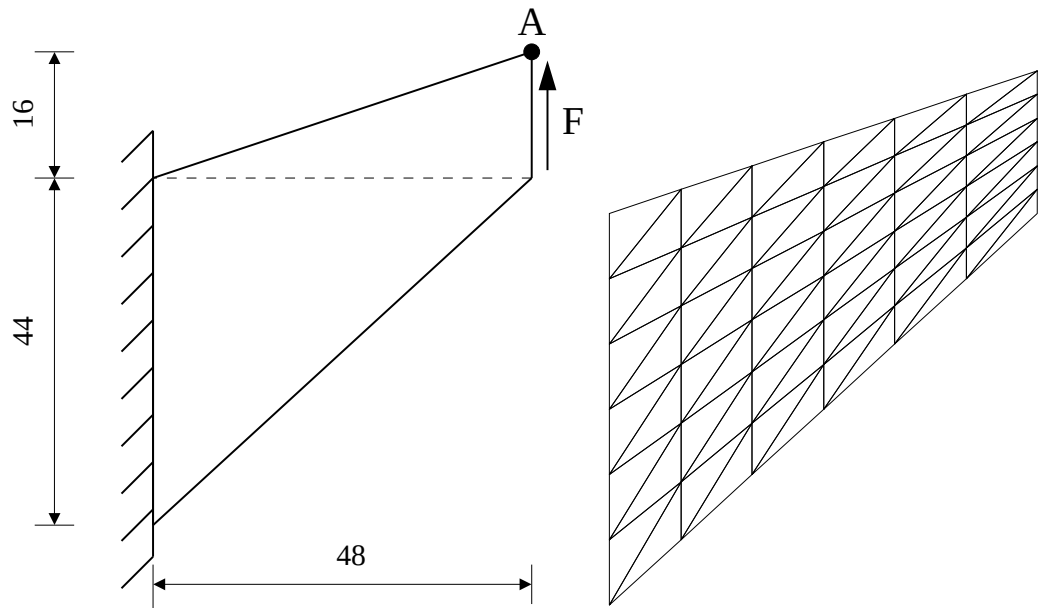

(a) (b)

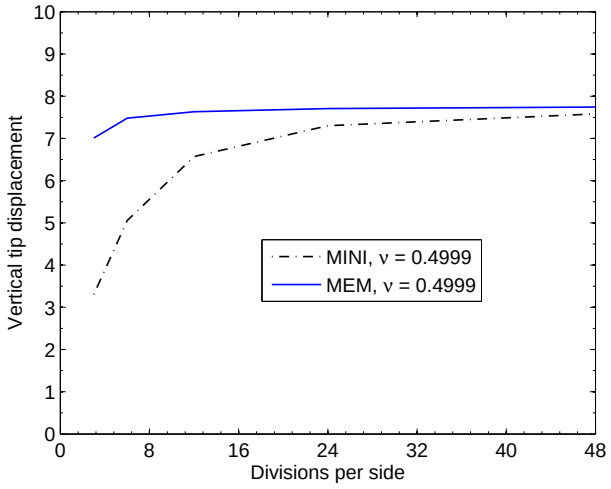

(c)

Figure 4.8: Cook's membrane problem. (a) Model geometry and boundary conditions; (b) Sample mesh; and (c) Vertical tip displacement. Nodal degrees of freedom are as shown in Fig. 4.1.

element method.

In order to demonstrate the need for the MOD integration scheme in three dimensions, the same analysis is conducted using an eight-order Gauss quadrature rule (STD integration

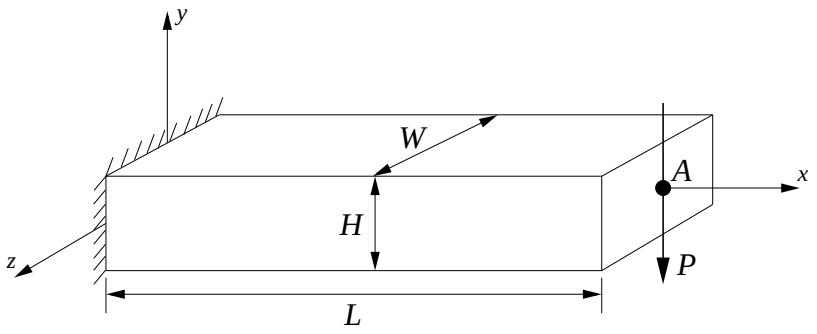

(a)

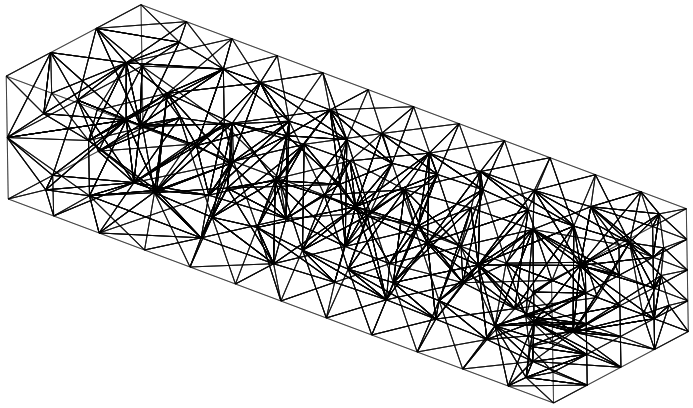

(b)

Figure 4.9: Three-dimensional cantilever beam. (a) Geometry, boundary and loading conditions; and (b) background mesh for integration.

scheme) for the MEM method. The numerical and exact tip deflections at point A are summarized in Table 4.4. We observe that the STD scheme can not deliver the correct result, and indeed higher-order Gauss quadrature is needed. The latter is not surprising since due to the unstructured mesh, the support of basis functions can get significantly large leading to under-integration if the accuracy of the quadrature rule employed is not sufficient. However, use of very higher-order Gauss quadrature is unappealing in a meshfree method since it imposes a computational burden on the simulations.

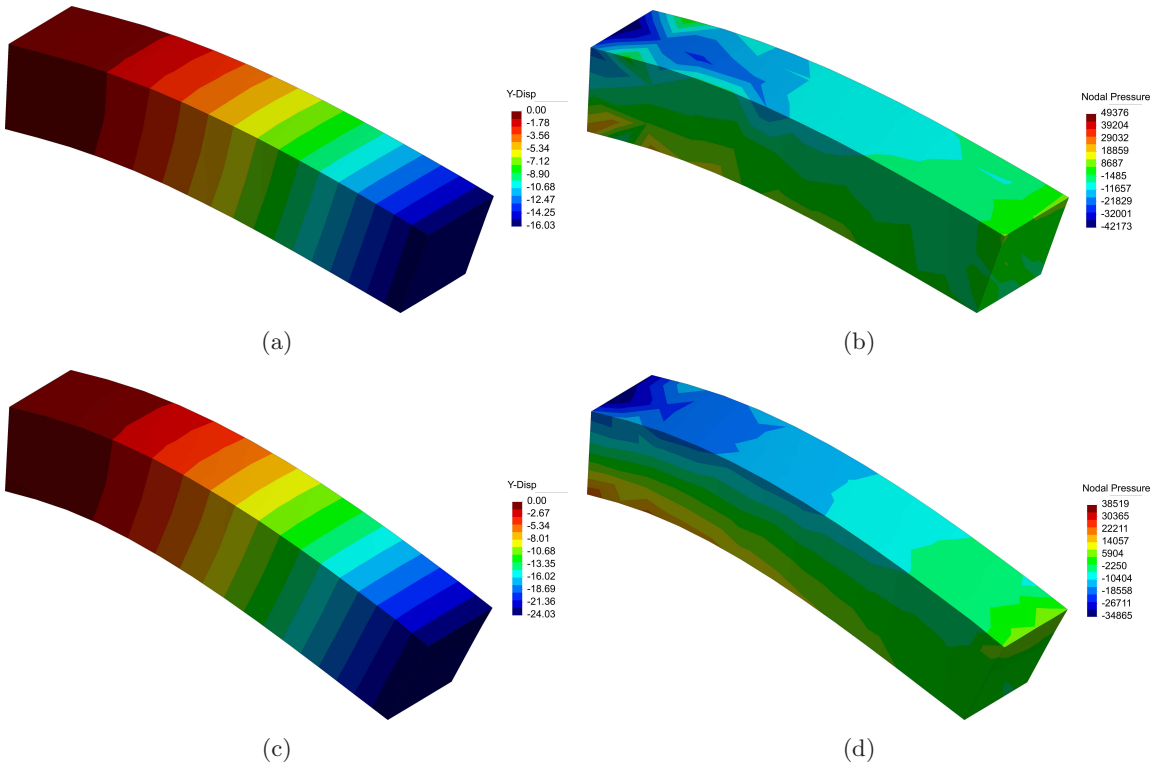

Figure 4.10: Three-dimensional cantilever beam. (a) MINI element solution for vertical displacement; (b) MINI element solution for hydrostatic pressure field; (c) MEM solution for vertical displacement; and (d) MEM solution for hydrostatic pressure field.

Table 4.4: Tip deflection for the three-dimensional cantilever beam at point A.

Method	Numerical	Exact
MINI	-16.02	-24.11
MEM (MOD)	-24.02	-24.11
MEM (STD)	-141.99	-24.11

4.5.5 Three-Dimensional Rigid Flat Punch

In this example, a simple model of three-dimensional frictionless indentation is considered to showcase the performance of the MEM method under compressive loads. Similar benchmark problems are typically studied in two dimensions [64, 96, 171]. The geometry of the problem is depicted in Fig. 4.11(a). A severe constraint on allowable deformation states is introduced by fully clamping the bottom surface and the four lateral surfaces. A frictionless

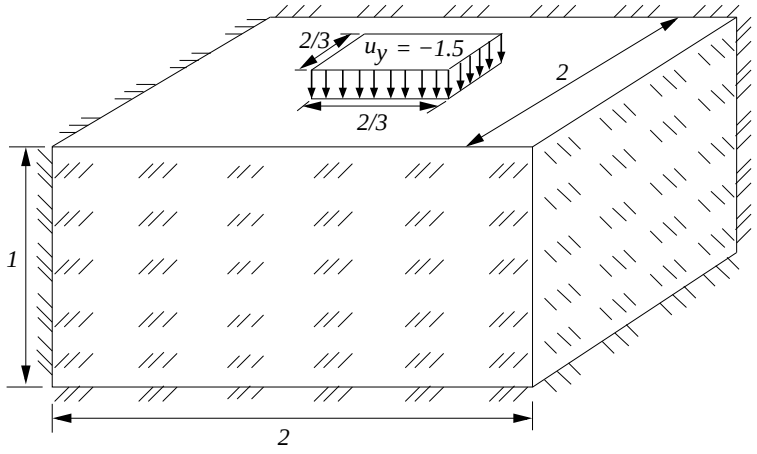

(a)

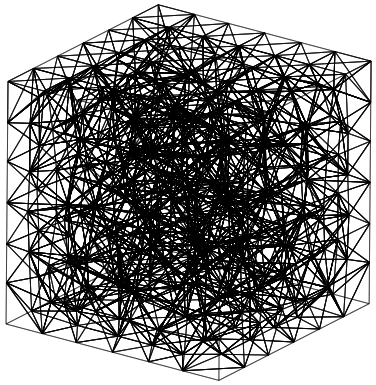

(b)

Figure 4.11: Three-dimensional rigid flat punch. (a) Geometry and boundary conditions; and (b) background mesh for integration.

downward displacement of 0.15 is applied on the center of the top surface within a square area of $2/3 \times 2/3$. Due to the symmetry of the problem, only a quarter of the geometry is considered. The material parameters are set to $E = 3 \times 10^7$ and $\nu = 0.4999$. The unstructured tetrahedral background mesh shown in Fig. 4.11(b) is used to demonstrate the ability of the MEM method. The numerical solutions for the `MINI` element are presented in Figs. 4.12(a) and 4.12(b), whereas the maximum-entropy solutions are depicted in Figs. 4.12(c) and 4.12(d). In light of these results, the MEM method is clearly superior in the prediction of the displacement field and in realizing a smoother pressure solution.

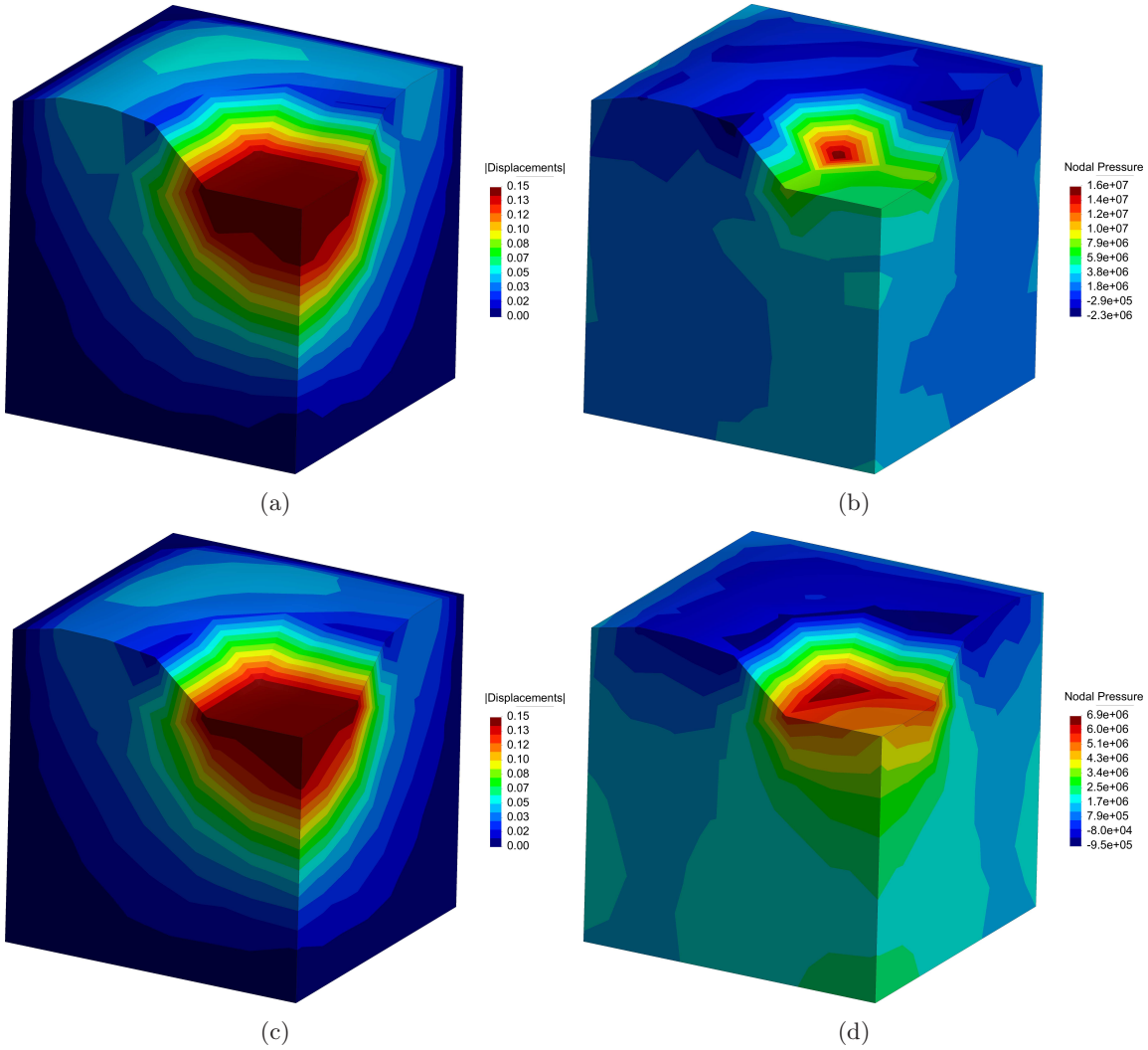

Figure 4.12: Three-dimensional rigid flat punch. (a) MINI element solution for displacement field; (b) MINI element solution for hydrostatic pressure field; (c) MEM solution for displacement field; and (d) MEM solution for hydrostatic pressure field.

4.5.6 Leaky-Lid Driven Cavity Flow

The leaky-lid driven cavity flow problem is a standard benchmark to test the performance of numerical methods in incompressible flow [7, 49, 167, 172]. The geometry, background mesh and prescribed velocity along the boundary of the domain are depicted in Fig. 4.13. Max-ent basis functions are used with a support-width parameter $\gamma = 2.0$ for the Gaussian prior.

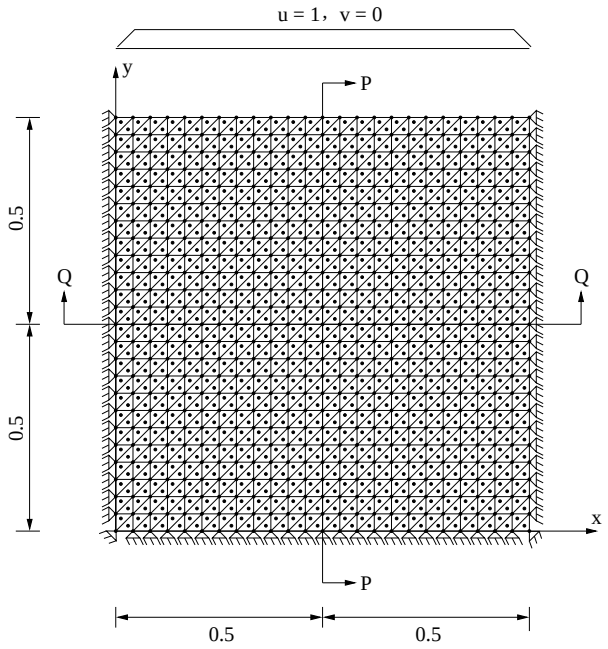

Figure 4.13: Leaky-lid driven cavity flow. Geometry, mesh and boundary conditions.

In Fig. 4.14, the numerical velocity and hydrostatic pressure fields for the `MINI` element and MEM formulation are compared. We observe that the velocity field is quite similar for both approximations and that they are in agreement with the numerical results of Ref. [167]. A good match between the velocity of the `MINI` and MEM solutions is observed in Fig. 4.15. However, the MEM method better predicts the hydrostatic pressure field with a smoother solution throughout the domain. This behavior is also confirmed by the results shown in Fig. 4.16, where the nodal pressure is plotted for two background meshes along line Q-Q. The first one, a coarser mesh of 12×12 divisions and the second one, a finer mesh of 24×24 divisions shown in Fig. 4.13. On the finer mesh, the `MINI` element solution drifts away from the smooth MEM solution, and the former also has some oscillations. The situation is still worse for the `MINI` element in the coarser mesh, whereas the MEM solution on both meshes is similar and they are in agreement with the results of Ref. [167].

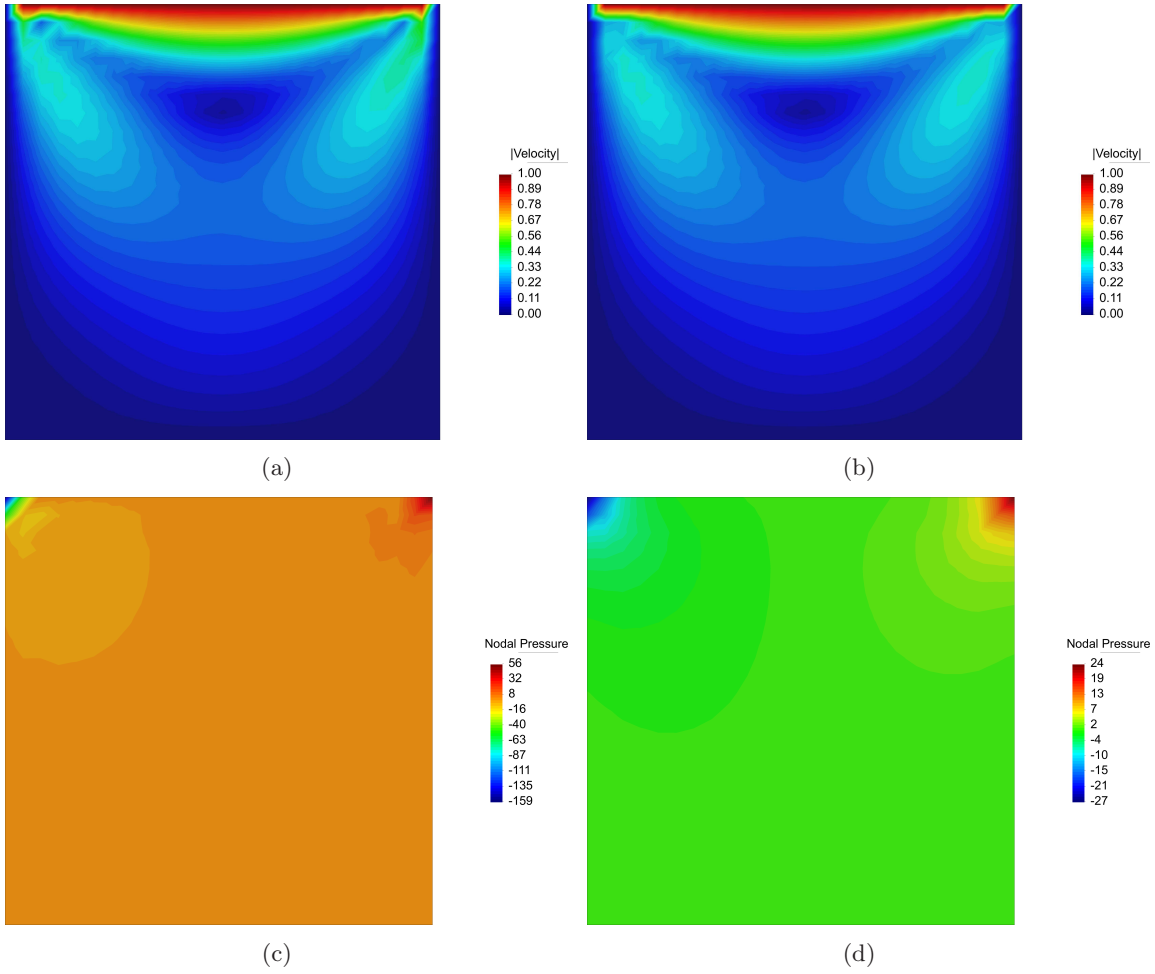

Figure 4.14: Leaky-lid driven cavity flow. (a) `MINI` element solution for velocity field, (b) MEM solution for velocity field, (c) `MINI` element solution for hydrostatic pressure field; and (d) MEM solution for hydrostatic pressure field.

4.5.7 Poiseuille Flow

In this example, we are interested in predicting the steady laminar flow between two fixed (no-slip) parallel plates (sufficiently large compared to the gap between the plates) when a parabolic velocity field is prescribed at the inlet. This problem is known as Poiseuille flow [173]. The geometry, background mesh and boundary conditions are shown in Fig. 4.17. On considering unit dynamic viscosity and vanishing natural boundary conditions at the outlet, the following analytical solution is valid well away from the edge of the plates [173]:

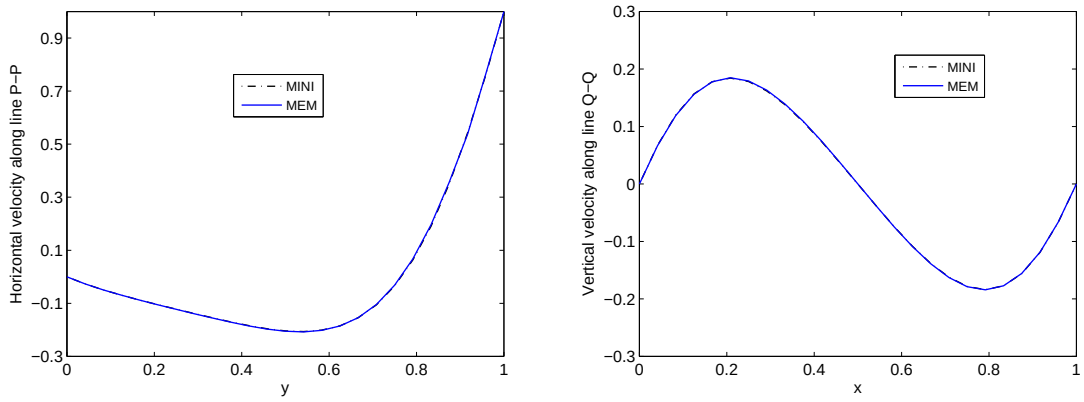

(a) (b)

Figure 4.15: Leaky-lid driven cavity flow. Nodal velocity measured along lines (a) P-P and (b) Q-Q.

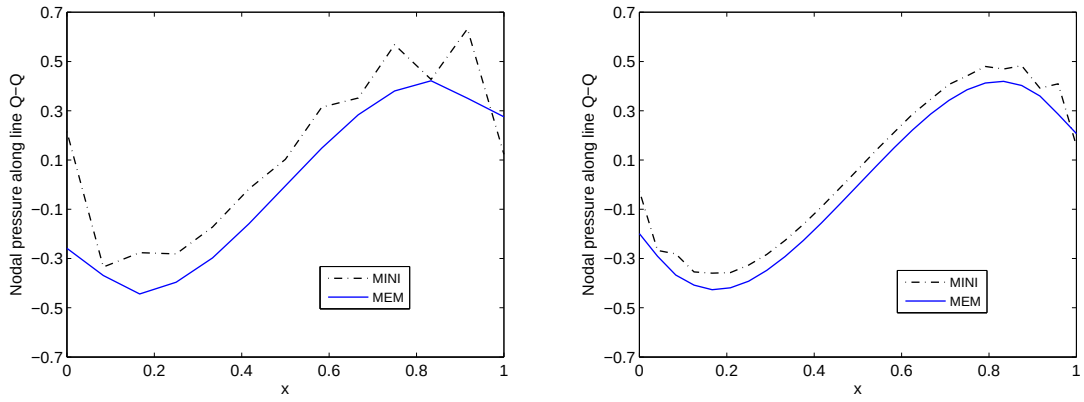

(a) (b)

Figure 4.16: Leaky-lid driven cavity flow. Nodal pressure measured along line Q-Q (a) for 12×12 mesh and (b) for 24×24 mesh.

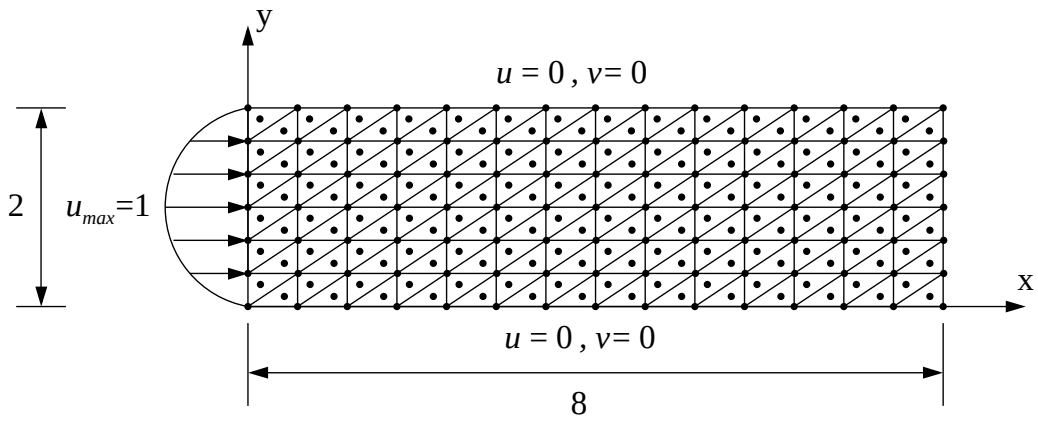

Figure 4.17: Poiseuille flow. Geometry, mesh and boundary conditions.

$$u = 1 - (y-1)^2, \tag{4.28a}$$

$$v = 0, \tag{4.28b}$$

$$p = -2x + 16, \tag{4.28c}$$

Eqs. (4.28a) and (4.28b) are imposed as essential boundary conditions at the inlet and on the upper and bottom plates. Max-ent basis functions are used with a support-width parameter $\gamma = 2.0$ for the Gaussian prior. The numerical axial velocity and pressure field are depicted in Fig. 4.18. We observe that both the `MINI` element and MEM solutions match the analytical solution in (4.28).

4.5.8 Inf-Sup Tests

The numerical inf-sup test described in Section 4.4 has been assessed for meshfree methods [29,44]. Here, the inf-sup test is applied on three problems: leaky-lid driven cavity flow, Poiseuille flow, and a square domain (the same used for the cavity flow) with zero-velocity imposed along the boundary. When a vanishing velocity is imposed along the boundary of the domain, a zero pressure field must be obtained everywhere. Otherwise, the formulation

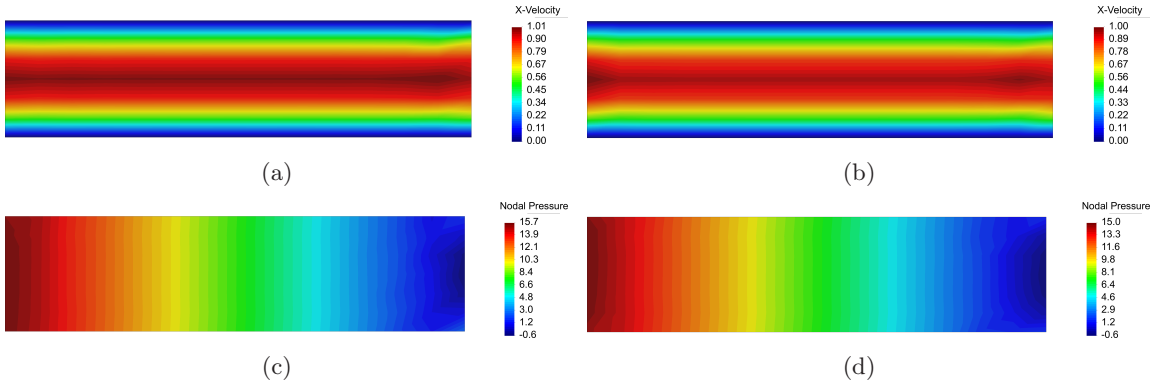

Figure 4.18: Poiseuille flow. (a) `MINI` element solution for axial velocity, (b) MEM solution for axial velocity, (c) `MINI` element solution for hydrostatic pressure field; and (d) MEM solution for hydrostatic pressure field.

Table 4.5: Values of α_h in the numerical inf-sup tests.

Problem	$n = 4$	$n = 8$	$n = 12$	$n = 16$
Cavity	0.295	0.308	0.308	0.300
Poiseuille	0.112	0.113	0.113	0.113
Zero-velocity	0.295	0.308	0.308	0.300

would suffer from spurious pressure modes [16]. In order to compute the numerical inf-sup value, four nodal discretizations are considered in each problem. The background meshes are shown in Fig. 4.19. Numerical inf-sup values are presented in Table 4.5. From Table 4.5, we observe that for all the tests the numerical inf-sup values converge to a value that is bounded away from zero with successive mesh refinements. Since the whole boundary has been imposed with essential boundary conditions for the leaky-lid driven cavity flow and zero-velocity tests, one constant pressure mode was obtained in both cases. However, the constant pressure mode can be eliminated if one essential boundary condition is removed from the boundary. We also mention that a zero-pressure field was obtained for the zero-velocity test, which indicates that the MEM formulation is free of spurious pressure modes. The inf-sup test is therefore passed and the MEM formulation is stable.

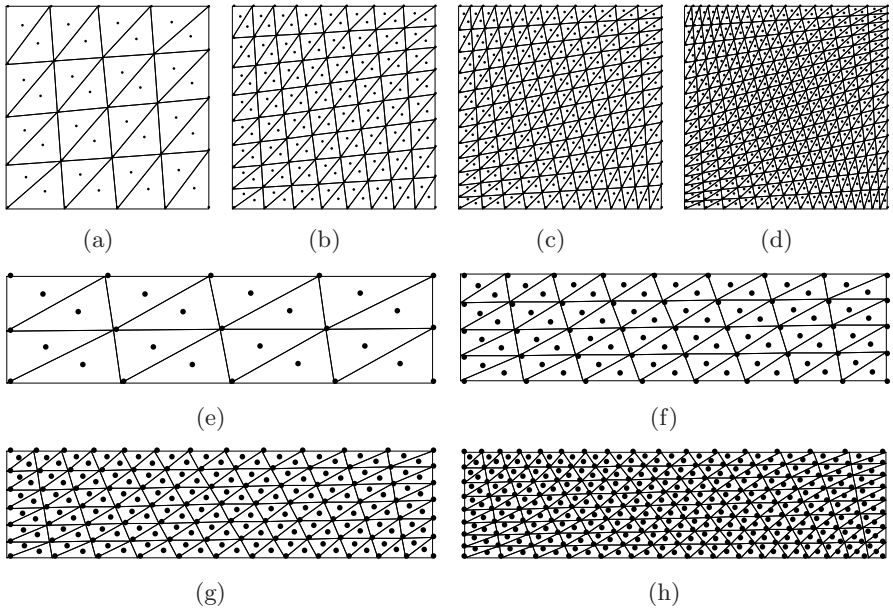

Figure 4.19: Distorted background meshes employed for the inf-sup test. (a), (b), (c) and (d) for the leaky-lid driven cavity flow and the zero-boundary velocity problems; (e), (f), (g) and (h) for the Poiseuille problem. $n \times n$ mesh pattern is used for the leaky-lid driven cavity flow and zero-boundary velocity problems, while for the Poiseuille flow, $n \times n/2$ mesh pattern is considered. In both cases n is the number of divisions along the x-direction.

Chapter 5

Maximum-Entropy Meshfree Method for Near-Incompressible Nonlinear Elasticity

In this chapter, the formulation of the maximum-entropy meshfree method for two-dimensional near-incompressible nonlinear elasticity is presented. Some basic concepts on nonlinear continuum mechanics that are used in several parts of this chapter are first given. A novel meshfree formulation for near-incompressible elastic solids at finite strains is then presented. The performance of the maximum-entropy meshfree method in large deformation analysis with near-incompressible behavior is investigated. Structured and unstructured three-node triangular background meshes are employed in three numerical experiments: a combined bending-shear problem (nonlinear Cook's membrane), a plane strain compression of a rubber block, and a frictionless indentation problem. In all the experiments, the maximum-entropy solution is compared to two finite element solutions that use three-node triangular meshes, namely, the linear displacement/constant pressure triangle (T1P0) and the `MINI` [166] element.

5.1 Basic Nonlinear Continuum Mechanics

5.1.1 Reference Map

The motion of a body is mathematically described by a mapping χ between initial ($\mathbf{X}$) and current ($\mathbf{x}$) body particle positions as

$$\mathbf{x} = \chi(\mathbf{X}, t) \equiv \mathbf{x}(\mathbf{X}, t), \tag{5.1}$$

where t is the time variable. For a fixed t, the above equation represents the mapping between the undeformed and deformed bodies. On the other hand, if $\mathbf{X}$ is kept fixed for a given particle, (5.1) represents the trajectory of that particle as a function of time. The undeformed configuration is referred to as *material*, *Lagrangian* or *reference* configuration, whereas the deformed configuration is referred to as *spatial*, *Eulerian* or *current* configuration.

5.1.2 Displacement Vector

The displacement vector is the distance between the spatial and material configurations of a particle and is given by

$$\mathbf{u} = \mathbf{x} - \mathbf{X}. \tag{5.2}$$

5.1.3 Deformation Gradient Tensor

The deformation gradient tensor is the gradient of the mapping function that describes the motion and is given by

$$\mathbf{F} = \frac{\partial \chi}{\partial \mathbf{X}} = \frac{\partial \mathbf{x}}{\partial \mathbf{X}} = \mathbf{I} + \frac{\partial \mathbf{u}}{\partial \mathbf{X}}. \tag{5.3}$$

The deformation gradient tensor plays a prominent role in finite deformation theory since it is used to define strain and stress measures as well as material constitutive relations. It accounts for geometrical effects that are neglected in infinitesimal deformation theory.

5.1.4 Volume Changes

Volume change ratio

It represents the ratio between the volume after deformation per unit reference (infinitesimal) volume, or simply *volume change ratio*. It is given by

$$J = \det \mathbf{F}. \tag{5.4}$$

If $J = 1$, no volume change is observed, which is the case when the body has not undergone any motion ($\mathbf{F} = \mathbf{I}$) or if it has deformed, its deformation is *isochoric*. On the other hand, $J = 0$ implies that the body has collapsed into a material particle, which is not physically acceptable. In general, $J > 0$ so that the deformation map is one-to-one.

Isochoric deformations

These are deformations that do not induce volume changes (*volume-preserving*). They only produce volume distortions. Isochoric deformations are described by $J = 1$.

Volumetric deformations

These are deformations that induce volume changes (*volume-dilatation*) that stem from uniform contraction/dilatation ratio in all directions. They are described by a spherical deformation gradient tensor as

$$\mathbf{F} = \alpha \mathbf{I}, \tag{5.5}$$

where α is a scalar representing the contraction/dilatation ratio.

5.1.5 Push-Forward/Pull-Back Operations

Measures defined on the material configuration can be expressed in terms of measures defined on the spatial configuration by means of a *push-forward* operation, which is denoted by $\chi_*[\cdot]$. For instance, the elemental spatial vector $d\mathbf{x}$ can be considered as the *push-forward*

of its material vector counterpart $d\mathbf{X}$. The operation is written as

$$d\mathbf{x} \equiv \chi_*[d\mathbf{X}] = \mathbf{F}d\mathbf{X}. \tag{5.6}$$

Conversely, measures defined on the spatial configuration can be expressed in terms of measures defined on the material configuration by means of a *pull-back* operation, which is denoted by $\chi_*^{-1}[\cdot]$. For instance, the elemental material vector $d\mathbf{X}$ can be considered as the *pull-back* of its spatial vector counterpart $d\mathbf{x}$. The operation is written as

$$d\mathbf{X} \equiv \chi_*^{-1}[d\mathbf{x}] = \mathbf{F}^{-1}d\mathbf{x}. \tag{5.7}$$

5.1.6 Strain Measures

Right Cauchy-Green deformation tensor

It is a symmetric material tensor given as

$$\mathbf{C} = \mathbf{F}^{\mathrm{T}}\mathbf{F}, \tag{5.8}$$

which is defined via the *push-forward* of the scalar product of two elemental material vectors as

$$d\mathbf{x}_1 \cdot d\mathbf{x}_2 = d\mathbf{X}_1 \cdot \mathbf{C}\, d\mathbf{X}_2. \tag{5.9}$$

The right Cauchy-Green deformation tensor represents the change in length of the two material vectors after deformation along with the change in the enclosed angle between the two material vectors after deformation.

Left Cauchy-Green deformation tensor

It is a symmetric spatial tensor given as

$$\mathbf{b} = \mathbf{F}\mathbf{F}^{\mathrm{T}}, \tag{5.10}$$

which is defined via the *pull-back* of the scalar product of two elemental spatial vectors as

$$d\mathbf{X}_1 \cdot d\mathbf{X}_2 = d\mathbf{x}_1 \cdot \mathbf{b}^{-1} d\mathbf{x}_2. \tag{5.11}$$

The left Cauchy-Green deformation tensor represents the change in length of the two spatial vectors measured from the material configuration along with the change in the enclosed angle between the two spatial vectors measured from the material configuration.

Green-Lagrange strain tensor

It is a symmetric material tensor defined as

$$\mathbf{E} = \frac{1}{2}(\mathbf{C} - \mathbf{I}). \tag{5.12}$$

Euler-Almansi strain tensor

It is a symmetric spatial tensor defined as

$$\mathbf{e} = \frac{1}{2}(\mathbf{I} - \mathbf{b}^{-1}). \tag{5.13}$$

5.1.7 Stress Measures

Cauchy stress tensor

It is a symmetric spatial tensor that represents the current force per unit of deformed area. It is also referred to as *true stress tensor* or simply *stress tensor* and is denoted by $\boldsymbol{\sigma}$.

First Piola-Kirchhoff stress tensor

It is an unsymmetric (neither spatial nor material) tensor that can be interpreted as the current force per unit of undeformed area and is related to the Cauchy stress tensor by

$$\mathbf{P} = J\boldsymbol{\sigma}\mathbf{F}^{-\mathrm{T}}. \tag{5.14}$$

Second Piola-Kirchhoff stress tensor

It is a symmetric material tensor that can be interpreted as a force in the undeformed configuration per unit of undeformed area and is related to the Cauchy stress tensor by

$$\mathbf{S} = J\mathbf{F}^{-1}\boldsymbol{\sigma}\mathbf{F}^{-\mathrm{T}}. \tag{5.15}$$

Kirchhoff stress tensor

It is a symmetric spatial tensor which results from a *push-forward* of the second Piola-Kirchhoff stress tensor as

$$\boldsymbol{\tau} = \mathbf{F}\mathbf{S}\mathbf{F}^{\mathrm{T}}, \tag{5.16}$$

which can be related to the Cauchy stress tensor by considering (5.15) to yield

$$\boldsymbol{\tau} = J\boldsymbol{\sigma}. \tag{5.17}$$

5.1.8 Hyperelasticity

When the work done by stresses during a deformation process is stored in the material as part of its internal energy and is independent of the path followed to reach the final configuration from the initial one, the material behavior is said to be *path-independent* and is termed *hyperelastic*. A *hyperelastic* material is characterized by a *strain energy function* or *elastic potential* Ψ.

Strain energy function

Various strain energy functions are available. Typical expressions for the strain energy of isotropic materials commonly used in the finite element and meshfree literature are:

$$\begin{aligned}
&\Psi(\mathbf{E}) = \tfrac{1}{2}\lambda(\mathrm{tr}\mathbf{E})^2 + \mu\mathbf{E}:\mathbf{E}, && \text{(St. Venant-Kirchhoff)}\\
&\Psi(\mathbf{C}) = \tfrac{1}{2}\mu(\mathrm{tr}\mathbf{C} - 3) - \mu\ln J + \tfrac{\lambda}{2}(\ln J)^2, && \text{(compressible neo-Hookean)}\\
&\Psi(\mathbf{C}) = \tfrac{1}{2}\mu(\mathrm{tr}\mathbf{C} - 3), && \text{(incompressible neo-Hookean)}
\end{aligned}$$

where λ and μ are the Lamé material parameters. When modeling incompressible materials with finite elements or meshfree methods, a common practice is to treat the material as slightly compressible, which results in near-incompressible material behavior. This is accomplished by separation of the strain energy function into two parts. An isochoric (distortional) part and a volumetric (dilatational) part. For instance, some examples of near-incompressible isotropic neo-Hookean materials commonly used to validate numerical procedures have the expressions:

$$\begin{aligned}
\Psi(\mathbf{C}) &= \tfrac{1}{2}\mu(J^{-2/3}\mathrm{tr}\mathbf{C} - 3) + \tfrac{1}{2}\kappa(J-1)^2,\\
\Psi(\mathbf{C}) &= \tfrac{1}{2}\mu(J^{-2/3}\mathrm{tr}\mathbf{C} - 3) + \tfrac{1}{2}\kappa(\ln J)^2,
\end{aligned}$$

where the parts that depend on the bulk modulus of the material, κ, are the volumetric strain energy functions.

Stress tensors

The second Piola-Kichhoff stress tensor is obtained as

$$\mathbf{S} = \frac{\partial \boldsymbol{\Psi}(\mathbf{E})}{\partial \mathbf{E}}, \tag{5.18}$$

which can also be written in terms of $\mathbf{C}$ with the aid of (5.12) as

$$\mathbf{S} = 2\frac{\partial \boldsymbol{\Psi}(\mathbf{C})}{\partial \mathbf{C}}. \tag{5.19}$$

Various other stress tensors can be obtained using the relations given in Section 5.1.7.

Elasticity tensors

Most numerical procedures, as the one proposed in this dissertation, are based on the minimization of a potential energy functional. On taking the first variation of that functional in an arbitrary direction yields the weak form which is used to build the numerical procedure. The relationship between stress and strain measures (constitutive relations) are nonlinear in hyperelasticity, therefore the weak form. An iterative procedure is then needed to find a solution that satisfies the weak form. Typically, Newton-based methods are employed. The latter implies that the weak form must be linearized. The linearization is usually done in the reference (material) configuration. A push-forward operation follows if the linearized quantities are required in the spatial configuration. As part of the linearization of the weak form in the reference configuration, we obtain the *material* or *Lagrangian elasticity tensor*, which is given as

$$\mathcal{C} = \frac{\partial \mathbf{S}(\mathbf{E})}{\partial \mathbf{E}} = 2\frac{\partial \mathbf{S}(\mathbf{C})}{\partial \mathbf{C}}. \tag{5.20}$$

F-bar methodology

An incompressible material that undergoes finite strains must satisfy

$$J = \det \mathbf{F} = 1. \tag{5.21}$$

In a numerical method, the above equation is typically enforced by means of Lagrange multipliers or penalty procedures in the minimization of a potential energy functional. A standard approach to model incompressible solids by means of penalty procedures implicitly

introduced in the material constitutive relation is obtained by using the multiplicative decomposition of the deformation gradient tensor [12, 72, 174–177] as

$$\mathbf{F} = \mathbf{F}^{\text{dil}}\mathbf{F}^{\text{dev}}, \tag{5.22}$$

where $\mathbf{F}^{\text{dil}} = J^{1/3}\mathbf{I}$ and $\mathbf{F}^{\text{dev}} = J^{-1/3}\mathbf{F}$. Due to the fact that the deviatoric part of the deformation gradient tensor is volume-preserving, $\det \mathbf{F}^{\text{dev}} = 1$. This leaves us with $\mathbf{F}^{\text{dil}}$ as the important quantity in the incompressible behavior of the media, namely,

$$\det \mathbf{F} = \left(\det \mathbf{F}^{\text{dil}}\right)\left(\det \mathbf{F}^{\text{dev}}\right) = \det \mathbf{F}^{\text{dil}} = 1 \tag{5.23}$$

to be enforced. For a single-field (finite element or meshfree) approximation, it would not be possible to satisfy $\det \mathbf{F}^{\text{dil}} = 1$ without inducing a locking mechanism. However, a locking-free methodology can be developed in a single-field formulation if the modified gradient tensor

$$\bar{\mathbf{F}} = \bar{\mathbf{F}}^{\text{dil}}\mathbf{F}^{\text{dev}} \tag{5.24}$$

is constructed. In (5.24), $\bar{\mathbf{F}}^{\text{dil}} = \bar{J}^{1/3}\mathbf{I}$, which leads to

$$\det \bar{\mathbf{F}} = \bar{J} = 1 \tag{5.25}$$

to be enforced in lieu of (5.21) or (5.23). An identity like (5.24) is coined as F-bar methodology in the literature and has been successfully used in the context of finite elements [72,177] and isogeometric analysis [12].

Of importance is to note that in standard displacement formulations, (5.21) imposes a severe constraint on possible deformations. That is, the resulting motion is unable to distort while simultaneously satisfying the incompressibility constraint (5.21), which leads to a catastrophic artificial stiffening known as volumetric locking. The F-bar methodology provides a means to preclude volumetric locking by considering two independent quantities,

namely, J and $\bar{J}$, which both depend on displacement field variables. The resulting motion is now able to distort while simultaneously satisfying the new constraint (5.25). An important step that follows is the appropriate definition of the 'bared' quantities in (5.25). This is presented in the next section.

5.2 F-bar Methodology in the Maximum-Entropy Meshfree Method

The key ingredient in the F-bar methodology is the definition of $\bar{J}$. For instance, in Ref. [12] it is defined as the L^2 projection onto the lower-order approximation space, whereas in Ref. [72] it is defined as the ratio of the volume of an element that belongs to a patch to the total volume of that patch. In the F-bar methodology that is proposed here for meshfree approximations, $\bar{J}$ is defined in a different way. The methodology presented in Chapter 4 for small strain elasticity is extended to nonlinear computations. To this end, a corresponding *volume-averaged nodal* quantity on J is considered for nonlinear analysis as follows:

$$J_a = \frac{\int_{\bar{\Omega}} N_a J \, d\Omega}{\int_{\bar{\Omega}} N_a \, d\Omega}, \tag{5.26}$$

where N_a is a linear finite element shape function[1] defined on a background (integration) mesh of three-node triangles and $\bar{\Omega}$ is the union of all the elements attached to node a, i.e., $\bar{\Omega} = \cup \Omega_a^e$. Following the approach of F-bar methodologies that was described in Section 5.1.8, we define $\bar{J}$ as the finite element interpolation of the nodal averages given in (5.26), i.e.,

$$\bar{J} = \sum_a N_a J_a. \tag{5.27}$$

Note that in the method developed in this dissertation, we compute the average of J itself (see (5.26)) and not the average of $J^{1/3}$ as is done in Ref. [12]. This leads to slightly

[1] Although a meshfree basis function could be used in lieu of N_a, this is not strictly needed for the meshfree method herein since derivatives of N_a do not appear in the formulation.

different results in the weak form and in its linearization. For convenience in further derivations, (5.24) is rewritten as follows on considering the definition of $\mathbf{F}^{\mathrm{dev}}$ and $\bar{\mathbf{F}}^{\mathrm{dil}}$:

$$\bar{\mathbf{F}} = \alpha \mathbf{F}, \tag{5.28}$$

where $\alpha = \left(\bar{J}/J\right)^{1/3}$.

The F-bar methodology of Ref. [12] operates on the potential energy functional, whereas the corresponding methodology of Refs. [72, 177] operates on the stress measure only. The former methodology is more consistent in hyperelasticity since it leads to a symmetric tangent stiffness matrix. The F-bar methodology for meshfree methods is developed along the lines of Ref. [12]. To this end, the usual space of admissible deformations is considered:

$$\mathscr{D} = \{\chi : \Omega \to \mathbb{R}^2 \mid \det \mathbf{F} > 0,\, \chi = \chi^* \ \text{on}\, \Gamma_\chi\}, \tag{5.29}$$

where $\Omega \in \mathbb{R}^2$ is an open bounded domain on the initial (reference) configuration with boundary Γ and χ is the mapping that defines the displacement of a particle from its initial position $\mathbf{X}$ to its current position $\mathbf{x}$, i.e., $\mathbf{u} = \chi(\mathbf{X}) - \mathbf{X} = \mathbf{x} - \mathbf{X}$. On the other hand, Γ_χ is the portion of the boundary where the deformation χ^* is prescribed. The vectors of external body forces $\mathbf{f}_0$ and external surface forces $\mathbf{t}_0$ are assumed independent of the motion. Next, the following modified potential energy functional is considered:

$$\bar{\Pi}(\chi) = \int_\Omega \Psi(\bar{\mathbf{E}}(\chi))\, d\Omega - \int_\Omega \mathbf{f}_0 \cdot \chi \, d\Omega - \int_{\Gamma_t} \mathbf{t}_0 \cdot \chi \, d\Gamma, \tag{5.30}$$

where $\Psi(\bar{\mathbf{E}}(\chi))$ is the modified strain energy function, which depends on $\bar{\mathbf{F}}$ through the modified Green-Lagrange strain tensor:

$$\bar{\mathbf{E}}(\chi) = \frac{1}{2}\left(\bar{\mathbf{F}}^{\mathrm{T}}\bar{\mathbf{F}} - \mathbf{I}\right). \tag{5.31}$$

The weak form of the finite strain near-incompressible elastic problem and its lineariza-

tion need to be carefully developed due to the dependency of the potential energy functional on the modified deformation gradient tensor $\bar{\mathbf{F}}$. We deal with this in the next section.

5.3 Variational Weak Form

The stationarity of (5.30) in the arbitrary direction $\mathbf{v} \in \mathscr{V} = \{\mathbf{v} : \Omega \to \mathbb{R}^2 \mid \mathbf{v} = \mathbf{0} \text{ on } \Gamma_\chi\}$ given by the directional derivative[2]

$$\mathrm{D}\bar{\Pi}(\chi)[\mathbf{v}] \equiv \left.\frac{\partial \bar{\Pi}(\chi + \epsilon \mathbf{v})}{\partial \epsilon}\right|_{\epsilon=0} = 0 \tag{5.32}$$

yields the weak form

$$\mathrm{D}\bar{\Pi}(\chi)[\mathbf{v}] = \int_\Omega \bar{\mathbf{S}}(\chi) : \mathrm{D}\bar{\mathbf{E}}(\chi)[\mathbf{v}]\, d\Omega - \int_\Omega \mathbf{f}_0 \cdot \mathbf{v}\, d\Omega - \int_{\Gamma_t} \mathbf{t}_0 \cdot \mathbf{v}\, d\Gamma = 0, \tag{5.33}$$

where the modified second Piola-Kirchhoff stress tensor $\bar{\mathbf{S}}(\chi)$ is defined as

$$\bar{\mathbf{S}}(\chi) = \mathbf{S}(\bar{\mathbf{E}}(\chi)) = \frac{\partial \Psi(\mathbf{E})}{\partial \mathbf{E}}(\bar{\mathbf{E}}(\chi)) \tag{5.34}$$

and $\mathrm{D}\bar{\mathbf{E}}(\chi)[\mathbf{v}]$ needs to be developed. To this end, the following operators are defined:

$$\theta(\cdot) = \sum_{a=1}^{3} N_a(\mathbf{X}) \left\{ \frac{\int_{\bar{\Omega}} N_a\{\cdot\}\, d\Omega}{\int_{\bar{\Omega}} N_a\, d\Omega} \right\}, \tag{5.35a}$$

$$\vartheta(\cdot) = \frac{\theta(\cdot)}{\bar{J}} - \frac{1}{J}\{\cdot\}, \tag{5.35b}$$

where $\bar{\Omega}$ was defined in (5.26). The complete derivation of $\mathrm{D}\bar{\mathbf{E}}(\chi)[\mathbf{v}]$ is presented in Appendix B. The final expression is

$$\mathrm{D}\bar{\mathbf{E}}(\chi)[\mathbf{v}] = \frac{1}{3}\vartheta \left(J \mathrm{tr}\left(\boldsymbol{\nabla}^0 \mathbf{v} \mathbf{F}^{-1}\right)\right) \bar{\mathbf{F}}^{\mathrm{T}} \bar{\mathbf{F}} + \alpha (\bar{\mathbf{F}}^{\mathrm{T}} \boldsymbol{\nabla}^0 \mathbf{v})_{\mathrm{sym}}. \tag{5.36}$$

[2]See Appendix A for details on directional derivative and weak form derivation.

On substituting (5.36) into (5.33) leads to the final weak form expression as

$$\begin{aligned} \mathrm{D}\bar{\Pi}(\chi)[\mathbf{v}] \;=\; & \frac{1}{3}\int_{\Omega} \vartheta\left(J\mathrm{tr}(\boldsymbol{\nabla}^0\mathbf{v}\mathbf{F}^{-1})\right)\bar{\mathbf{S}} : (\bar{\mathbf{F}}^{\mathrm{T}}\bar{\mathbf{F}})\, d\Omega + \int_{\Omega}\alpha\bar{\mathbf{S}} : (\bar{\mathbf{F}}^{\mathrm{T}}\boldsymbol{\nabla}^0\mathbf{v})_{\mathrm{sym}}\, d\Omega \\ & - \int_{\Omega}\mathbf{f}_0\cdot\mathbf{v}\, d\Omega - \int_{\Gamma_t}\mathbf{t}_0\cdot\mathbf{v}\, d\Gamma = 0. \end{aligned} \tag{5.37}$$

5.4 Linearized Weak Form

The implicit numerical solution relies on the linearization of the weak form (5.37). The linearized weak form in the direction of the increment $\Delta\mathbf{u}$ is given by [3]

$$\mathrm{D}\bar{\Pi}(\chi)[\mathbf{v}] + \mathrm{D}^2\bar{\Pi}(\chi)[\mathbf{v},\Delta\mathbf{u}] = 0, \tag{5.38}$$

where $\mathrm{D}^2\bar{\Pi}(\chi)[\mathbf{v},\Delta\mathbf{u}] \equiv \mathrm{D}\left\{\mathrm{D}\bar{\Pi}(\chi)[\mathbf{v}]\right\}[\Delta\mathbf{u}]$ is the second variation of $\bar{\Pi}(\chi)$ in $\Delta\mathbf{u}$. The derivation of the second variation is complicated and leads to many terms. Thus, only the final result is provided here and details are given in Appendix B. The external forces are assumed independent of the motion, and for the sake of clarity, the second variation is split into a material and a geometric part:

$$\mathrm{D}^2\bar{\Pi}(\chi)[\mathbf{v},\Delta\mathbf{u}] = \left(\mathrm{D}^2\bar{\Pi}(\chi)[\mathbf{v},\Delta\mathbf{u}]\right)_{\mathrm{mat}} + \left(\mathrm{D}^2\bar{\Pi}(\chi)[\mathbf{v},\Delta\mathbf{u}]\right)_{\mathrm{geo}}, \tag{5.39a}$$

where

$$\begin{aligned} \left(\mathrm{D}^2\bar{\Pi}(\chi)[\mathbf{v},\Delta\mathbf{u}]\right)_{\mathrm{mat}} = & + \frac{1}{9}\int_{\Omega}\vartheta\left(J\mathrm{tr}(\boldsymbol{\nabla}^0\mathbf{v}\mathbf{F}^{-1})\right)\vartheta\left(J\mathrm{tr}(\boldsymbol{\nabla}^0\Delta\mathbf{u}\mathbf{F}^{-1})\right)(\bar{\mathbf{F}}^{\mathrm{T}}\bar{\mathbf{F}}) : \bar{\mathcal{C}} : (\bar{\mathbf{F}}^{\mathrm{T}}\bar{\mathbf{F}})\, d\Omega \\ & + \frac{1}{3}\int_{\Omega}\alpha\,\vartheta\left(J\mathrm{tr}(\boldsymbol{\nabla}^0\mathbf{v}\mathbf{F}^{-1})\right)(\bar{\mathbf{F}}^{\mathrm{T}}\bar{\mathbf{F}}) : \bar{\mathcal{C}} : (\bar{\mathbf{F}}^{\mathrm{T}}\boldsymbol{\nabla}^0\Delta\mathbf{u})_{\mathrm{sym}}\, d\Omega \\ & + \frac{1}{3}\int_{\Omega}\alpha(\bar{\mathbf{F}}^{\mathrm{T}}\boldsymbol{\nabla}^0\mathbf{v})_{\mathrm{sym}} : \bar{\mathcal{C}} : (\bar{\mathbf{F}}^{\mathrm{T}}\bar{\mathbf{F}})\,\vartheta\left(J\mathrm{tr}(\boldsymbol{\nabla}^0\Delta\mathbf{u}\mathbf{F}^{-1})\right)\, d\Omega \\ & + \int_{\Omega}\alpha^2(\bar{\mathbf{F}}^{\mathrm{T}}\boldsymbol{\nabla}^0\mathbf{v})_{\mathrm{sym}} : \bar{\mathcal{C}} : (\bar{\mathbf{F}}^{\mathrm{T}}\boldsymbol{\nabla}^0\Delta\mathbf{u})_{\mathrm{sym}}\, d\Omega, \end{aligned} \tag{5.39b}$$

[3] See Appendix A for details on linearization of nonlinear equations and linearization of the weak form.

and

$$\begin{aligned}\left(\mathrm{D}^2\bar{\Pi}(\chi)[\mathbf{v},\Delta\mathbf{u}]\right)_{\text{geo}} = &-\frac{1}{3}\int_\Omega \frac{1}{\bar{J}^2}\,\theta\left(J\mathrm{tr}(\boldsymbol{\nabla}^0\mathbf{v}\mathbf{F}^{-1})\right)\theta\left(J\mathrm{tr}(\boldsymbol{\nabla}^0\Delta\mathbf{u}\mathbf{F}^{-1})\right)\bar{\mathbf{S}} : (\bar{\mathbf{F}}^{\mathrm{T}}\bar{\mathbf{F}})\,d\Omega\\ &+\frac{1}{3}\int_\Omega \frac{1}{\bar{J}}\,\theta\left(J\mathrm{tr}(\boldsymbol{\nabla}^0\mathbf{v}\mathbf{F}^{-1})\mathrm{tr}(\boldsymbol{\nabla}^0\Delta\mathbf{u}\mathbf{F}^{-1})\right)\bar{\mathbf{S}} : (\bar{\mathbf{F}}^{\mathrm{T}}\bar{\mathbf{F}})\,d\Omega\\ &-\frac{1}{3}\int_\Omega \frac{1}{\bar{J}}\,\theta\left(J\mathrm{tr}(\boldsymbol{\nabla}^0\mathbf{v}\mathbf{F}^{-1}\boldsymbol{\nabla}^0\Delta\mathbf{u}\mathbf{F}^{-1})\right)\bar{\mathbf{S}} : (\bar{\mathbf{F}}^{\mathrm{T}}\bar{\mathbf{F}})\,d\Omega\\ &+\frac{1}{3}\int_\Omega \mathrm{tr}(\boldsymbol{\nabla}^0\mathbf{v}\mathbf{F}^{-1}\boldsymbol{\nabla}^0\Delta\mathbf{u}\mathbf{F}^{-1})\bar{\mathbf{S}} : (\bar{\mathbf{F}}^{\mathrm{T}}\bar{\mathbf{F}})\,d\Omega\\ &+\frac{2}{9}\int_\Omega \vartheta\left(J\mathrm{tr}(\boldsymbol{\nabla}^0\mathbf{v}\mathbf{F}^{-1})\right)\vartheta\left(J\mathrm{tr}(\boldsymbol{\nabla}^0\Delta\mathbf{u}\mathbf{F}^{-1})\right)\bar{\mathbf{S}} : (\bar{\mathbf{F}}^{\mathrm{T}}\bar{\mathbf{F}})\,d\Omega\\ &+\frac{2}{3}\int_\Omega \alpha\,\vartheta\left(J\mathrm{tr}(\boldsymbol{\nabla}^0\mathbf{v}\mathbf{F}^{-1})\right)\bar{\mathbf{S}} : (\bar{\mathbf{F}}^{\mathrm{T}}\boldsymbol{\nabla}^0\Delta\mathbf{u})_{\text{sym}}\,d\Omega\\ &+\frac{2}{3}\int_\Omega \alpha(\bar{\mathbf{F}}^{\mathrm{T}}\boldsymbol{\nabla}^0\mathbf{v})_{\text{sym}} : \bar{\mathbf{S}}\,\vartheta\left(J\mathrm{tr}(\boldsymbol{\nabla}^0\Delta\mathbf{u}\mathbf{F}^{-1})\right)\,d\Omega\\ &+\int_\Omega \alpha^2\bar{\mathbf{S}} : [(\boldsymbol{\nabla}^0\mathbf{v})^{\mathrm{T}}\boldsymbol{\nabla}^0\Delta\mathbf{u}]_{\text{sym}}\,d\Omega. \end{aligned} \tag{5.39c}$$

In the derivation of (5.39b), the modified Lagrangian elasticity tensor $\bar{\mathcal{C}}$ is obtained as follows:

$$\bar{\mathcal{C}} = \mathcal{C}(\bar{\mathbf{E}}(\chi)) = \frac{\partial\mathbf{S}(\mathbf{E})}{\partial\mathbf{E}}(\bar{\mathbf{E}}(\chi)). \tag{5.40}$$

Finally, upon collecting terms from (5.37) and (5.39b)-(5.39c) and substituting into (5.38) yields the final expression for the linearized weak form.

5.5 Discrete Linearized Weak Form

Discretization of the linearized weak form (5.38) leads to the following Newton-Raphson scheme:

$${}^{t+\Delta t}\left(\mathbf{K}_{\text{mat}} + \mathbf{K}_{\text{geo}}\right)^{(i-1)}\Delta\mathbf{u}^{(i)} = {}^{t+\Delta t}\mathbf{F} - {}^{t+\Delta t}\mathbf{T}^{(i-1)}, \tag{5.41}$$

where $t+\Delta t$ is to indicate that the material and geometric tangent stiffness matrices, $\mathbf{K}_{\text{mat}}$ and $\mathbf{K}_{\text{geo}}$, respectively, and the external and internal nodal force vectors, $\mathbf{F}$ and $\mathbf{T}$, respectively, are computed incrementally by application of boundary conditions (forces and

displacements) in increments. On the other hand, i stands for the equilibrium iterations that are involved within an increment. A solution obtained from the Newton-Raphson scheme (5.41) is computationally demanding in most practical applications due to the continuous formation of $\mathbf{K}_{\text{mat}}$ and $\mathbf{K}_{\text{geo}}$. Other schemes that provide a compromise between accuracy and computational cost are desired. Among such schemes BFGS [178] seems to be the most robust for large computations and is therefore widely used in the implementations in this dissertation. Details on the latter and other Newton-based schemes for solving nonlinear equations are provided in Appendix C.

In order to derive the material and geometric tangent stiffness matrix, as well as the residual nodal force vector (right-hand side of (5.41)), the following maximum-entropy approximations are used for both the test and trial functions in the reference configuration:

$$\Delta\mathbf{u}_h(\mathbf{X}) = \sum_{a=1}^{3} \phi_a(\mathbf{X})\Delta\mathbf{u}_a, \tag{5.42a}$$

$$\mathbf{v}_h(\mathbf{X}) = \sum_{a=1}^{3} \phi_a(\mathbf{X})\mathbf{v}_a, \tag{5.42b}$$

where now the nodal quantities are related to the nodes of the three-node triangular background (integration) mesh plus an extra interior node per triangle, which mimics a bubble node ensuring a good balance between number of displacement degrees of freedom and number of dilatational constraints [7]. Fig. 5.1 depicts a sample mesh used for displacement approximation as well as averaging of J (see (5.26)) in the maximum-entropy meshfree method. In what follows, the following matrix notations which result from symmetry considerations are used:

$$\{\bar{\mathbf{C}}\} = \{\bar{\mathbf{F}}^{\mathrm{T}}\bar{\mathbf{F}}\} = \begin{bmatrix} \bar{C}_{11} & \bar{C}_{22} & 2\bar{C}_{12} \end{bmatrix}^{\mathrm{T}}, \tag{5.43}$$

$$\{\bar{\mathbf{S}}\} = \begin{bmatrix} \bar{S}_{11} & \bar{S}_{22} & \bar{S}_{12} \end{bmatrix}^{\mathrm{T}}, \tag{5.44}$$

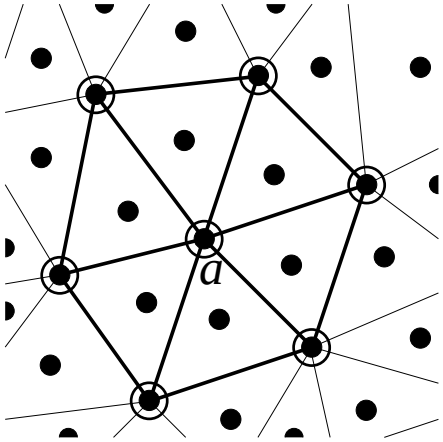

Figure 5.1: Mesh to compute volume-averaged nodal J around a representative node a. Filled black circles represent displacement nodes and open circles are the nodes used for linear finite element shape functions.

$$\{\bar{\mathcal{C}}\} = \begin{bmatrix} \bar{\mathcal{C}}_{1111} & \bar{\mathcal{C}}_{1122} & \bar{\mathcal{C}}_{1112} \\ \bar{\mathcal{C}}_{2211} & \bar{\mathcal{C}}_{2222} & \bar{\mathcal{C}}_{2212} \\ \bar{\mathcal{C}}_{1211} & \bar{\mathcal{C}}_{1222} & \bar{\mathcal{C}}_{1212} \end{bmatrix}, \tag{5.45}$$

where $\{\cdot\}$ denotes Voigt notation; and the following matrix forms which result from the discretization procedure:

$$\mathbf{B}_q = \begin{bmatrix} (F_{11})^{-1}\phi_{q,X} & 0 \\ 0 & (F_{22})^{-1}\phi_{q,Y} \\ (F_{21})^{-1}\phi_{q,Y} & (F_{12})^{-1}\phi_{q,X} \end{bmatrix}, \tag{5.46}$$

$$\bar{\mathbf{B}}_q^0 = \begin{bmatrix} \bar{F}_{11}\phi_{q,X} & \bar{F}_{21}\phi_{q,X} \\ \bar{F}_{12}\phi_{q,Y} & \bar{F}_{22}\phi_{q,Y} \\ \bar{F}_{12}\phi_{q,X} + \bar{F}_{11}\phi_{q,Y} & \bar{F}_{22}\phi_{q,X} + \bar{F}_{21}\phi_{q,Y} \end{bmatrix}, \tag{5.47}$$

$$\bar{\mathbf{B}}_q^{kk} = \begin{bmatrix} \vartheta\left(J\mathbf{m}^{\mathrm{T}}\mathbf{B}_q\right)\bar{C}_{11} \\ \vartheta\left(J\mathbf{m}^{\mathrm{T}}\mathbf{B}_q\right)\bar{C}_{22} \\ 2\vartheta\left(J\mathbf{m}^{\mathrm{T}}\mathbf{B}_q\right)\bar{C}_{12} \end{bmatrix}, \tag{5.48}$$

$$\bar{\mathbf{B}}_q = \frac{1}{3}\bar{\mathbf{B}}_q^{kk} + \alpha\bar{\mathbf{B}}_q^0. \tag{5.49}$$

Additionally, the following vector that arises from some trace operations is defined:

$$\mathbf{m} = \begin{bmatrix} 1 & 1 & 1 \end{bmatrix}^{\mathrm{T}}. \tag{5.50}$$

5.5.1 Residual Nodal Force Vector

The residual nodal force vector is $\mathbf{R} = {}^{t+\Delta t}\mathbf{F} - {}^{t+\Delta t}\mathbf{T}^{(i-1)}$ and is obtained upon discretization of (5.37), which yields

$$\begin{aligned} \mathbf{R} \;=\; & \sum_q \mathbf{v}_q^{\mathrm{T}} \left[\int_\Omega \phi_q \mathbf{f}_0 \, d\Omega + \int_\Gamma \phi_q \mathbf{t}_0 \, d\Gamma \right. \\ & \left. -\frac{1}{3}\int_\Omega \vartheta \left(J\mathbf{B}_q^{\mathrm{T}}\mathbf{m} \right) \{\bar{\mathbf{C}}\}^{\mathrm{T}} \{\bar{\mathbf{S}}\} \, d\Omega - \int_\Omega \alpha \left(\bar{\mathbf{B}}_q^0 \right)^{\mathrm{T}} \{\bar{\mathbf{S}}\} \, d\Omega \right]. \end{aligned} \tag{5.51}$$

5.5.2 Material Tangent Stiffness Matrix

The material tangent stiffness matrix is obtained upon discretization of (5.39b). Before proceeding likewise, terms in (5.39b) are rearranged such that the following expression is obtained:

$$\left(\mathrm{D}^2\bar{\Pi}(\chi)[\mathbf{v}, \Delta\mathbf{u}] \right)_{\mathrm{mat}} = \int_\Omega (\boldsymbol{\nabla}^0 \bar{\mathbf{v}}) : \bar{\mathcal{C}} : (\boldsymbol{\nabla}^0 \Delta\bar{\mathbf{u}}) \, d\Omega, \tag{5.52}$$

where

$$\boldsymbol{\nabla}^0(\bar{\cdot}) = \frac{1}{3}\vartheta \left(J\mathrm{tr}(\boldsymbol{\nabla}^0(\cdot)\mathbf{F}^{-1}) \right) \bar{\mathbf{C}} + \alpha \left(\bar{\mathbf{F}}^{\mathrm{T}} \boldsymbol{\nabla}^0(\cdot) \right)_{\mathrm{sym}}. \tag{5.53}$$

Due to the symmetry of (5.52), further arrangements can be done by using Voigt notation to obtain

$$\left(\mathrm{D}^2\bar{\Pi}(\chi)[\mathbf{v}, \Delta\mathbf{u}] \right)_{\mathrm{mat}} = \int_\Omega \{\boldsymbol{\nabla}^0 \bar{\mathbf{v}}\}^{\mathrm{T}} \{\bar{\mathcal{C}}\} \{\boldsymbol{\nabla}^0 \Delta\bar{\mathbf{u}}\} \, d\Omega. \tag{5.54}$$

Finally, on substituting (5.42) into (5.54) leads to the following discrete material tangent stiffness matrix:

$$\mathbf{K}_{\text{mat}} = \sum_p \sum_q \mathbf{v}_p^{\mathrm{T}} \left[\int_\Omega \bar{\mathbf{B}}_p^{\mathrm{T}} \{\bar{\mathcal{C}}\} \bar{\mathbf{B}}_q \, d\Omega \right] \Delta \mathbf{u}_q. \tag{5.55}$$

5.5.3 Geometric Tangent Stiffness Matrix

On substituting (5.42) into (5.39c) yields the following discrete geometric tangent stiffness matrix:

$$\begin{aligned}
\mathbf{K}_{\text{geo}} \;=\; & \sum_p \sum_q \mathbf{v}_p^{\mathrm{T}} \Bigg[-\frac{1}{3} \int_\Omega \frac{1}{\bar{J}^2} \, \theta \left(J \mathbf{B}_p^{\mathrm{T}} \mathbf{m} \right) \theta \left(J \mathbf{m}^{\mathrm{T}} \mathbf{B}_q \right) \{\bar{\mathbf{C}}\}^{\mathrm{T}} \{\bar{\mathbf{S}}\} \, d\Omega \\
& + \frac{1}{3} \int_\Omega \frac{1}{\bar{J}} \, \theta \left(J \mathbf{B}_p^{\mathrm{T}} \mathbf{m} \mathbf{m}^{\mathrm{T}} \mathbf{B}_q \right) \{\bar{\mathbf{C}}\}^{\mathrm{T}} \{\bar{\mathbf{S}}\} \, d\Omega \\
& - \frac{1}{3} \int_\Omega \frac{1}{\bar{J}} \, \theta \left(J \mathbf{F}^{-\mathrm{T}} (\boldsymbol{\nabla}^0 \phi_p) (\boldsymbol{\nabla}^0 \phi_q)^{\mathrm{T}} \mathbf{F}^{-1} \right) \{\bar{\mathbf{C}}\}^{\mathrm{T}} \{\bar{\mathbf{S}}\} \, d\Omega \\
& + \frac{1}{3} \int_\Omega \mathbf{F}^{-\mathrm{T}} (\boldsymbol{\nabla}^0 \phi_p) (\boldsymbol{\nabla}^0 \phi_q)^{\mathrm{T}} \mathbf{F}^{-1} \{\bar{\mathbf{C}}\}^{\mathrm{T}} \{\bar{\mathbf{S}}\} \, d\Omega \\
& + \frac{2}{9} \int_\Omega \vartheta \left(J \mathbf{B}_p^{\mathrm{T}} \mathbf{m} \right) \vartheta \left(J \mathbf{m}^{\mathrm{T}} \mathbf{B}_q \right) \{\bar{\mathbf{C}}\}^{\mathrm{T}} \{\bar{\mathbf{S}}\} \, d\Omega \\
& + \frac{2}{3} \int_\Omega \alpha \, \vartheta \left(J \mathbf{B}_p^{\mathrm{T}} \mathbf{m} \right) \{\bar{\mathbf{S}}\}^{\mathrm{T}} \bar{\mathbf{B}}_q^0 \, d\Omega \\
& + \frac{2}{3} \int_\Omega \alpha (\bar{\mathbf{B}}_p^0)^{\mathrm{T}} \{\bar{\mathbf{S}}\} \, \vartheta \left(J \mathbf{m}^{\mathrm{T}} \mathbf{B}_q \right) \, d\Omega \\
& + \mathbf{I} \int_\Omega \alpha^2 (\boldsymbol{\nabla}^0 \phi_p)^{\mathrm{T}} \bar{\mathbf{S}} (\boldsymbol{\nabla}^0 \phi_q) \, d\Omega \Bigg] \Delta \mathbf{u}_q.
\end{aligned} \tag{5.56}$$

5.6 Numerical Results and Discussions

In this section, the performance of the maximum-entropy meshfree (MEM) method for two-dimensional analysis of near-incompressible elastic solids at finite strains is examined. By means of three benchmark problems, the ability of the MEM method in the nonlinear regime is tested by comparing its numerical solution to the corresponding ones of two mixed *u-p* finite elements, namely, the linear displacement/constant pressure triangle (T1P0) and the `MINI` [166] element. The former is well-known to fail the LBB inf-sup stability condition [13–15], whereas the second one is LBB stable and has proved to be the most stable finite element

for two-dimensional analysis of fully incompressible elastic solids at finite strains [179]. In all the numerical experiments, the following neo-Hookean material is considered:

$$\Psi(\mathbf{C}) = \frac{1}{2}\mu(J^{-2/3}\mathrm{tr}\mathbf{C} - 3) + \frac{1}{2}\kappa(\ln J)^2, \tag{5.57}$$

with material parameters $\mu = 80.1938$ and $\kappa = 400942$, which results in a near-incompressible elastic solid with $\nu = 0.49989$. For all the examples in this section, the nodal degrees of freedom are arranged as shown in Fig. 5.1. In respect of the parameters of max-ent basis functions (see Section 3.3), we usually set $\gamma = 1.1$ to $\gamma = 1.5$ for the quartic prior. In the examples, fifth-order accurate Gauss integration scheme has been used for the MEM method, whereas third-order sufficed for the finite element methods. This difference in the integration order is expected since meshfree basis functions are rational functions and their supports do not coincide with the background cells that are employed in the numerical integration. Details on numerical integration issues in meshfree methods are presented in Section 4.2 of Chapter 4. In the examples, no explicit unit system is adopted, but consistency of units is assumed.

5.6.1 Nonlinear Cook's Membrane

In this example, the ability of the proposed meshfree formulation is studied by means of a standard benchmark problem that has been employed by many authors to test the behavior of near-incompressible formulations under combined bending and shear in distorted meshes [12,64,96]. The model geometry and boundary conditions are shown in Fig. 5.2(a). The left edge of the membrane is clamped and its right end is subjected to a shear load $F = 6.25$ per unit length (total shear load of 100). A reference background mesh of $n \times n$ subdivisions is shown in Fig. 5.2(b) for $n = 20$. The convergence study of the vertical tip displacement at point A upon mesh refinement is shown in Fig. 5.2(c) for the MEM method and both finite element methods. Numerical results indicate that the MEM convergence is superior to the finite elements convergence, and that is achieved with moderate mesh size.

We observe that the MINI element solution behaves somewhat 'stiff' and therefore requires an even more refined mesh than those employed in the analysis to emulate what is obtained by the MEM method. On the other hand, the poor convergence showed by the T1P0 element is symptomatic of its well-known instability which does not preclude locking completely. The overall performance of the three methods considered is presented in Fig. 5.3 for the vertical displacement and pressure field solutions obtained with the mesh depicted in Fig. 5.2(b). We observe that the MEM and MINI element solutions deliver smooth pressure fields, whereas the pressure field for the T1P0 exhibits checkerboard pattern.

5.6.2 Plane Strain Compression

The following example is a standard test to demonstrate the ability of meshfree methods to withstand very large strains [81, 89, 93]. It consists of a plane strain analysis of a rubber block compression. The top and bottom surfaces of the block are assumed perfectly bonded to rigid plates. The compression is simulated by incrementally applying a downward displacement on the top surface with the bottom surface fixed to deform the model up to a vertical nominal strain of 35%. Due to the symmetry of the problem, only a quarter of the model is considered. The model geometry, boundary conditions and background mesh employed in the analysis are depicted in Fig. 5.4. A pictorial of the analysis results for the vertical displacement and pressure fields is presented in Fig. 5.5 for the last converged solution of the MEM and finite element methods. The poor performance of the T1P0 element is evident in Figs. 5.5(a) and 5.5(b) since an unreasonable deformation is predicted with checkerboarding pressure modes. On the other hand, the MINI element solutions presented in Figs. 5.5(c) and 5.5(d) reveal that the MINI element is unable to achieve the total compression imposed in the test even though checkerboard pressure pattern is not observed. Finally, the MEM solutions illustrated in Figs. 5.5(e) and 5.5(f) seem reasonable with respect to the solutions reported in other meshfree studies [81, 89, 93] for the total compression imposed in the analysis. It is also evident that the MEM method does not present checkerboarding pressure modes and delivers smooth pressure field.

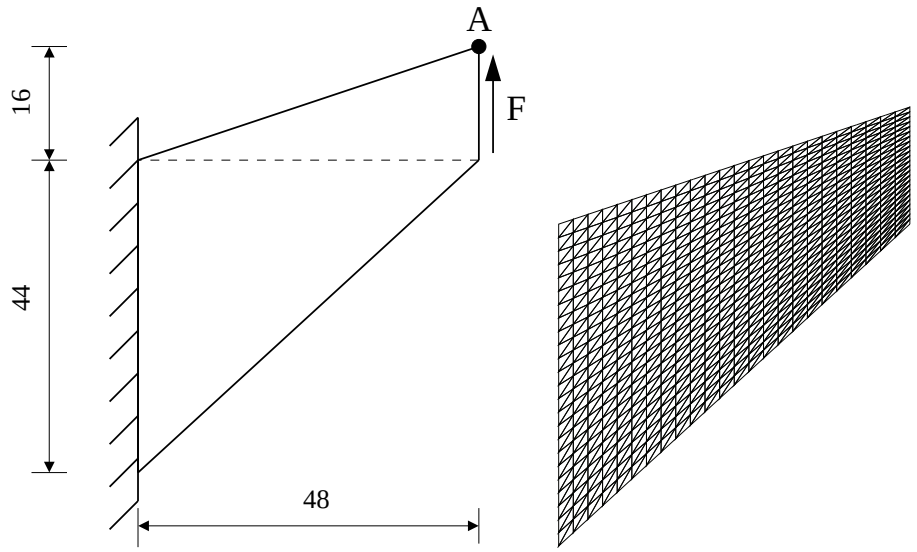

(a) (b)

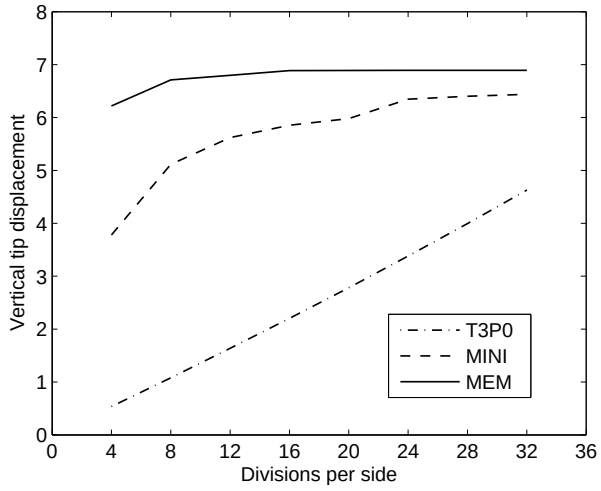

(c)

Figure 5.2: Nonlinear Cook's membrane. (a) Model geometry and boundary conditions; (b) Sample mesh; and (c) Vertical tip displacement convergence.

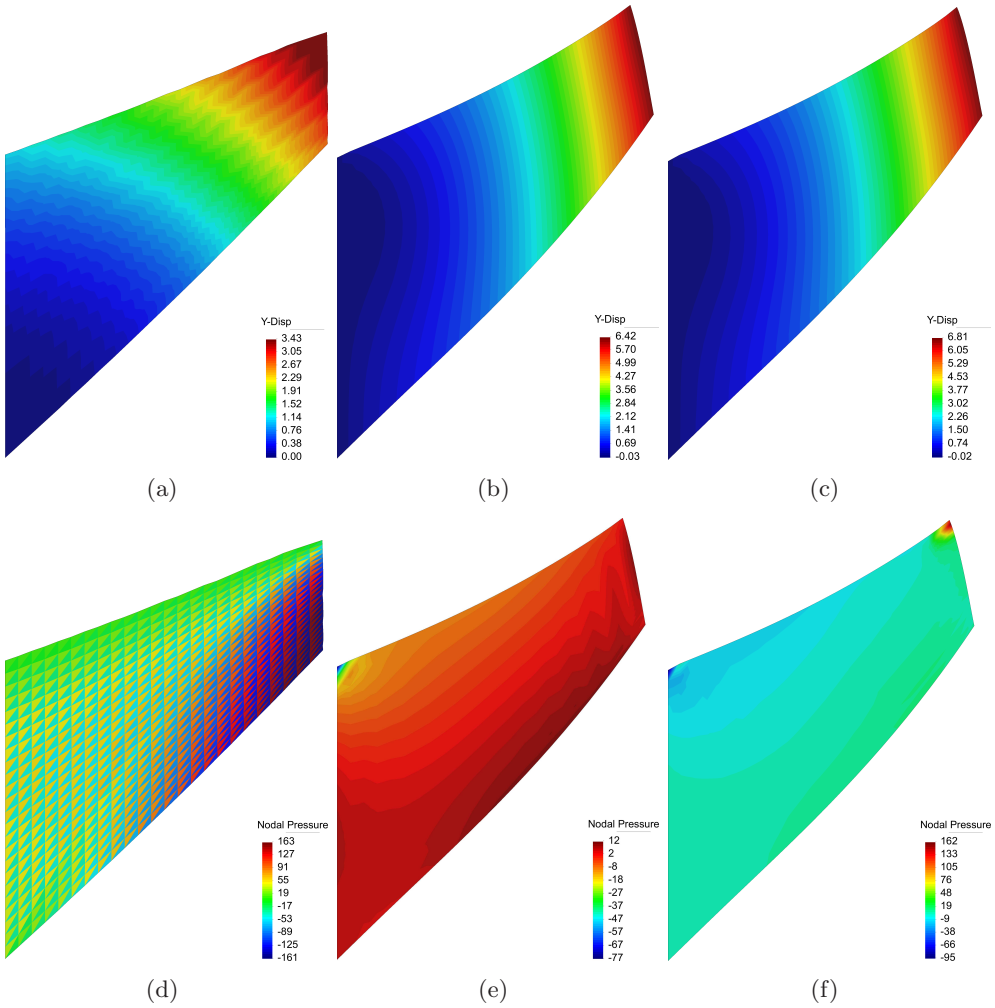

Figure 5.3: Nonlinear Cook's membrane. Vertical displacement and hydrostatic pressure field solutions for the mesh shown in Fig. 5.2(b). (a),(d)T3P0 element; (b),(e) MINI element; and (c),(f) MEM method.

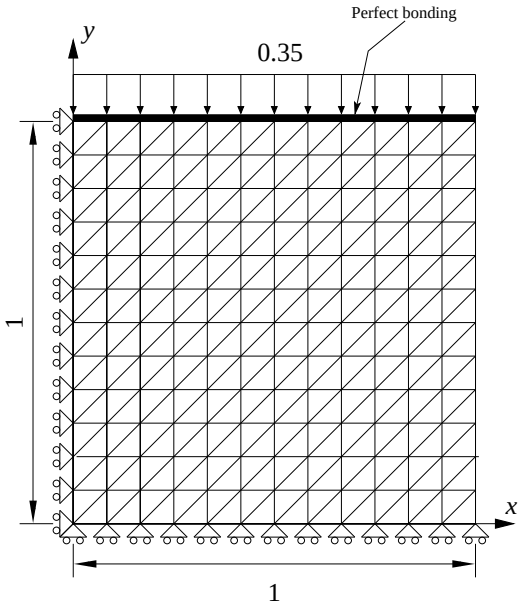

Figure 5.4: Plane strain compression. Model geometry, boundary conditions and background mesh.

We also study up to how much deformation the MEM method is able to withstand. In this endeavor, a very particular behavior was found in the upper right corner of the domain when undergoing extreme large deformations. This behavior is shown in Fig. 5.6 for a vertical nominal strain of 70%. It consists of a flipping mechanism of the elements close to that corner. However, this is not surprising for a method like the one presented here for a couple of reasons. Firstly, the computation of meshfree basis functions derivatives does not rely on the parametric mapping that is needed in finite element methods. Therefore, issues such as negative volumes and singular Jacobi matrix, which breakdown finite element computations, do not arise in meshfree methods. Secondly, in the proposed method for near-incompressible analysis, the determinant of the deformation gradient tensor, namely J, is not relevant in the near-incompressible limit but the average $\bar{J}$, which is computed from the elements surrounding a node. Therefore, even though $J < 0$ may occur for a particular element, the average $\bar{J}$ can still be a positive scalar allowing the computation anyhow. We think that this behavior should be viewed as a virtue of meshfree methods rather than a weakness, but we realize that the underlying phenomena which motivate this

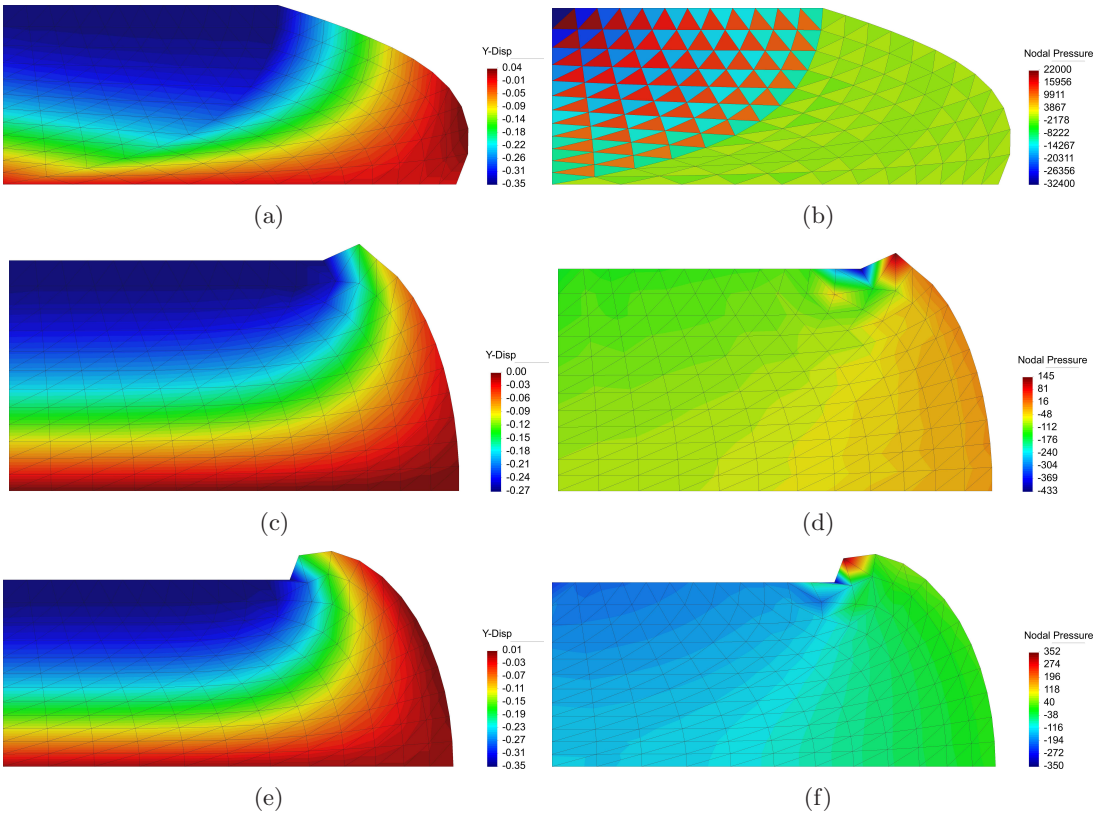

Figure 5.5: Plane strain compression. Vertical displacement and hydrostatic pressure field solutions. (a),(b) T3P0 element; (c),(d) MINI element; and (e),(f) MEM method.

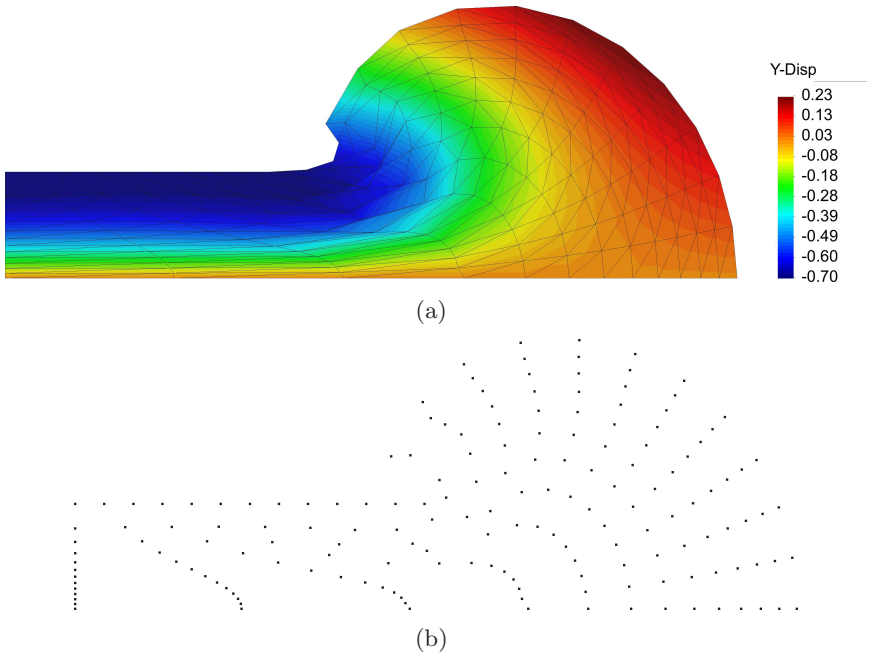

Figure 5.6: Plane strain compression. Extreme large deformations achieved by the MEM method. (a) Vertical displacement field and background integration mesh in the deformed configuration; and (b) nodes in the deformed configuration.

flipping behavior must be studied in detail. Among the underlying phenomena that might shed some light on the flipping of elements are physical instabilities, numerical instabilities and integration errors of the Gauss scheme employed.

5.6.3 Frictionless Indentation of a Rubber Block

The last example considered is a frictionless indentation of a rubber block of rectangular cross section, which is assumed to be in plain strain condition. The bottom and lateral surfaces are fixed in their normal directions, whereas a rectangular frictionless rigid indenter pushes inward a portion of the top surface. The indentation is simulated by incrementally applying a downward displacement on the top surface to deform the block up to a vertical nominal strain of 35%. A test of this type has been employed to evaluate near-incompressible formulations under highly constrained compression (e.g., see Refs. [12, 64, 96, 180, 181]). In addition, we wanted to evaluate the proposed method for

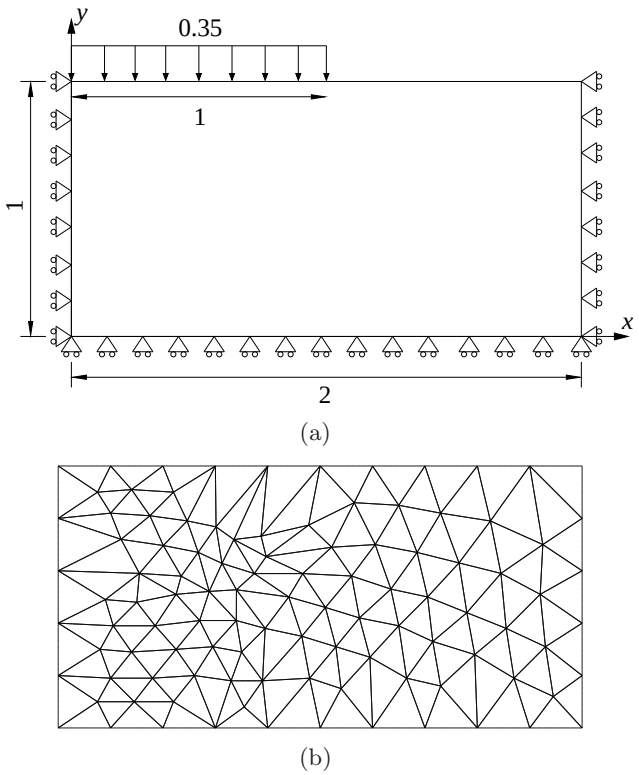

Figure 5.7: Frictionless indentation of a rubber block. (a) Model geometry and boundary conditions; and (b) Unstructured mesh employed.

near-incompressible hyperelasticity when an unstructured background mesh is employed for numerical integration of the weak form. Although a good tessellation can be easily obtained with two-dimensional mesh generators, we intentionally constructed a zone with poorly-shaped elements to compare the solution of the meshfree method with those of its finite element counterpart. The model geometry, boundary conditions and the unstructured background mesh employed in the analysis are shown in Fig. 5.7. The vertical displacement and pressure fields resulted from the analysis are illustrated in Fig. 5.8 for the last converged solution of the MEM and finite elements methods. Once again, we observe that the T1P0 predicts an unreasonable deformed shape with checkerboarding pressure modes, whereas the `MINI` element withstands only up to a vertical nominal strain of around 24%. We also observe that in the `MINI` element solution an unreasonable deformation state results near to the zone where poorly-shaped elements reside, which clearly is a consequence of the acute

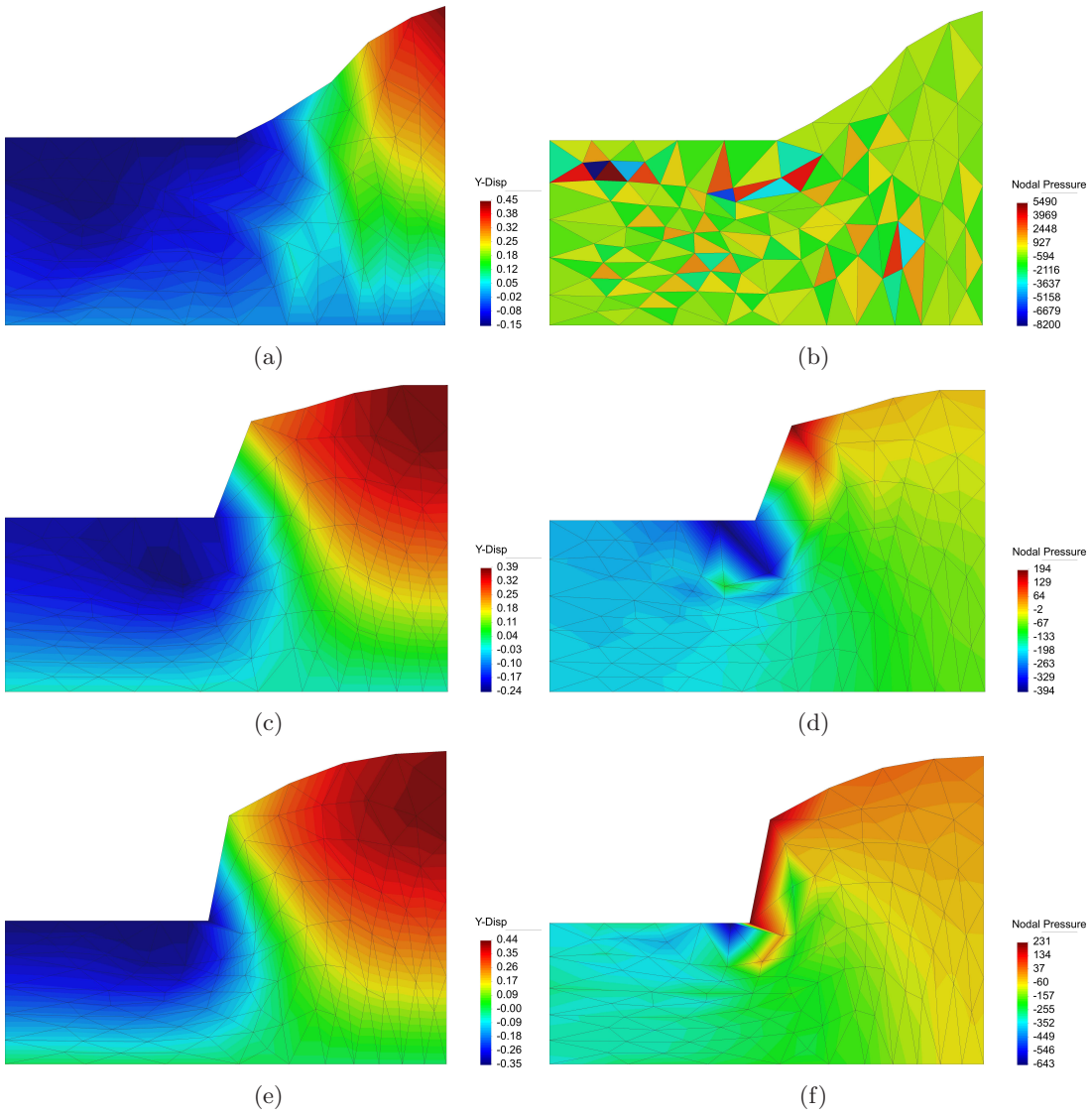

Figure 5.8: Frictionless indentation of a rubber block. Vertical displacement and pressure solutions for the last stable increment. (a),(b) T3P0 element; (c),(d) MINI element; and (e),(f) MEM method.

angles in the element. On the other hand, we observe that the solution delivered by the MEM method does not present that unreasonable deformation state. The superiority of the MEM method is attested by its ability to withstand the total indentation applied by the indenter with a smoother pressure field.

Chapter 6

Summary and Conclusions

In this dissertation, a Galerkin meshfree method based on maximum-entropy approximants was developed and its applications to elastostatics was demonstrated. The standard displacement-based Galerkin formulation was used to model compressible linear elastic solids, whereas the classical *u-p* mixed formulation for near-incompressible linear elastic media was adopted to formulate a volume-averaged nodal technique, in which the pressure variable is eliminated from the analysis. This resulted in a single-field (displacement or velocity) formulation that is devoid of volumetric locking. Since numerical integration errors are prevalent in meshfree methods, a modified Gauss integration technique was proposed to accurately compute the weak form integrals of the linear elastostatics problem. On considering ideas from assumed strain methods and nodal integration techniques, a redefinition of the small strain tensor was devised, which after discretization with maximum-entropy basis functions resulted in a correction to the stiffness matrix that alleviated integration errors in meshfree methods and proved to pass the patch test to machine accuracy.

Various standard benchmark problems were studied to assess the accuracy, performance and versatility of the maximum-entropy meshfree method for compressible and near-incompressible linear elastic media. Patch tests on structured and unstructured background meshes were considered to affirm its satisfaction to within machine precision for both

compressible and near-incompressible linear elasticity. A cantilever beam subjected to a parabolic end load was then considered. The maximum-entropy and MINI element displacement field solutions were compared to the exact (analytical) solution for both compressible and near-incompressible behavior. A convergence study for the vertical tip displacement was conducted. The maximum-entropy meshfree method converged faster with mesh refinements, whereas the MINI element solution behaved somewhat 'stiff'. In the maximum-entropy computations, standard Gauss integration sufficed for compressible elasticity with low-order quadrature, whereas the proposed modified Gauss integration provided a more efficient scheme with less Gauss points evaluations in the near-incompressible case. Optimal rates of convergence in the L^2- and energy-norm of the error were found for both the maximum-entropy meshfree method and the MINI element, but the former was more accurate. The MINI element results also showed some pressure oscillations, whereas the maximum-entropy meshfree method delivered smooth pressure field. A further example consisted in a combined bending and shear problem (Cook's membrane). A convergence test for the vertical tip displacement upon mesh refinement was conducted for both the maximum-entropy method and the MINI element. Superior convergence was found in the maximum-entropy meshfree method.

We then moved to three-dimensional problems with the aim of testing unstructured tetrahedral background meshes. Two examples were considered. A three-dimensional cantilever beam subjected to an end load and a three-dimensional rigid flat punch test. In the first problem, the maximum-entropy and MINI element vertical tip displacement solutions were studied. The maximum-entropy method delivered almost the exact (analytical) solution, whereas the MINI element solution underestimated it. Due to the complexity of basis functions supports on unstructured tetrahedral meshes, standard Gauss integration proved to be prohibitive for practical use—eight-order accurate scheme was insufficient, whereas the proposed modified Gauss integration scheme only required a second-order accurate scheme. In the three-dimensional rigid flat punch test, smoother solutions were found in the maximum-entropy meshfree method for both displacement and pressure fields.

In further examples, the volume-averaged formulation was tested in two Stokes flow problems: a leaky-lid driven cavity flow and the Poiseuille flow. Good agreement between maximum-entropy and `MINI` element velocity field solutions were found in both problems. However, in the former the pressure field predicted by the maximum-entropy meshfree method was smooth, whereas pressure oscillations were found in the `MINI` element solution. Finally, a series of numerical inf-sup tests were performed to assess the stability of the maximum-entropy meshfree method in various Stokes flow problems. With nodal refinement, the numerical inf-sup value remained a constant that was bounded away from zero; furthermore, there were no spurious pressure modes. These results affirmed the stability of the maximum-entropy meshfree method.

The maximum-entropy meshfree method was extended to treat near-incompressible elastic solids at finite strains in two dimensions. The nonlinear version of the volume-averaged nodal technique was formulated and used to average the dilatational constraint at a node from the displacement field of surrounding nodes. The methodology resulted in a single-field formulation (displacement-based) which is devoid of volumetric locking and is amenable for meshfree methods due to its node-wise character. It also exhibits commonalities with the F-bar methodologies that were recently developed for finite elements [96] and isogeometric analysis [12], and therefore it can be regarded as an F-bar methodology for meshfree methods. In devising this meshfree formulation, we were driven by the idea of improving the poor performance of low-order meshes in simulating near-incompressible hyperelastic problems. The meshfree method was developed for background meshes composed of three-node triangles, and its extension to four-node tetrahedra for three-dimensional simulations is straightforward. However, since fifth-order accurate standard Gauss integration scheme was required in two-dimensions, a more efficient integration scheme should be designed for the method to be robust in three-dimensional nonlinear computations.

Two different finite elements that rely on three-node triangular meshes were considered as a basis for comparison with the maximum-entropy meshfree method. The linear displacement/constant pressure triangle (T1P0) and the `MINI` element were considered.

A nonlinear Cook's membrane was considered to assess the meshfree methodology under combined bending and shear. A convergence study of the vertical tip displacement was performed. The maximum-entropy convergence was superior to the finite elements convergence with mesh refinements. Both the maximum-entropy meshfree method and the `MINI` element presented smooth pressure fields, whereas the pressure field delivered by the T1P0 showed checkerboard pattern, as expected. A plane strain compression of a rubber block was next considered to study the performance of the meshfree method under extreme large deformations induced by compression. The T1P0 element performed poorly with checkerboarding pressure modes, whereas the `MINI` element could not withstand the complete compression imposed in the analysis, although it did not present checkerboard pressure pattern. On the other hand, the maximum-entropy solution confirmed its superior performance by achieving the total compression imposed in the analysis with a smoother pressure field. The last example consisted in a frictionless indentation of a rubber block. The maximum-entropy meshfree method along with the finite elements were tested on an unstructured three-node triangular mesh with badly-shaped elements. As expected, the T1P0 element predicted an unreasonable displacement field with checkerboard pressure pattern, whereas the `MINI` element was unable to withstand the total displacement imposed by the indenter and presented a rare deformation near to the badly-shaped elements location. The superiority of the maximum-entropy meshfree method was verified by its ability to deform up to the total compression induced by the indenter with a smoother pressure field.

Two contributions have emanated from this dissertation. The first original contribution is the development of a novel technique for modeling near-incompressible media with low-order meshes (triangles and tetrahedra) in an effective manner due to the mesh distortion insensitivity property of meshfree basis functions. A formulation that renders low-order meshes viable for near-incompressible analysis is especially beneficial in two situations. Firstly, in complex geometries, where low-order triangular or tetrahedral meshes might be the only alternative for discretization, and secondly, in large deformation computations, where mesh distortions can invalidate the analysis if standard finite elements are used on

such meshes. The second original contribution is the development of an efficient and accurate numerical integration technique for meshfree methods that use cell-based integration. Numerical integration in meshfree methods is well-known to be prone to errors with patch test not being met to within machine precision. Many attempts have been made to improve the accuracy of the numerical integration in meshfree methods. However, these have resulted in expensive numerical integration schemes. The modified Gauss integration scheme proposed in this dissertation has proved to be a simple and inexpensive alternative for accurate integrations that also provides patch test satisfaction to machine accuracy. In particular, it was shown to be very efficient in three-dimensional settings on unstructured tetrahedral background meshes. The generality of the proposed modified Gauss integration technique renders it applicable not only for any Galerkin-based meshfree method such as the element-free Galerkin method and the natural element method, but also for polygonal finite element interpolants. The extension of the nonlinear meshfree methodology to three-dimensional near-incompressible solids at finite strains along with the development of an accurate numerical integration scheme for meshfree methods in nonlinear analysis will demonstrate the potential of the maximum-entropy meshfree method as a numerical tool. Developments along these lines are suggested for future investigations.

Appendix A

Directional Derivative and Linearizations

A.1 Directional Derivative

Consider a real-valued function $\mathbf{f}(\mathbf{z})$. The *directional derivative* of $\mathbf{f}(\mathbf{z})$ in the direction $\mathbf{n}$ is defined as

$$\mathrm{D}\mathbf{f}(\mathbf{z})[\mathbf{n}] \equiv \left.\frac{\partial \mathbf{f}(\mathbf{z}+\epsilon\mathbf{n})}{\partial \epsilon}\right|_{\epsilon=0}, \tag{A.1}$$

which represents the gradient of $\mathbf{f}(\mathbf{z})$ in the direction $\mathbf{n}$ and gives a linear (or first-order) approximation to the increment in $\mathbf{f}(\mathbf{z})$ due to the increment $\mathbf{n}$. The directional derivative is used in the derivation of the weak form (see Chapter 5, Section 5.3) and in its linearization (see Chapter 5, Section 5.5). The use of the directional derivative in the linearization of nonlinear equations is described in the next section.

A.2 Linearization of Nonlinear Equations

Consider a real-valued nonlinear system of equations $\mathbf{r}(\mathbf{z}) = \mathbf{0}$, which has a solution estimate $\mathbf{z}_k$ at iteration k. A new value $\mathbf{z}_{k+1} = \mathbf{z}_k + \mathbf{w}$ is obtained in terms of an increment $\mathbf{w}$ by

establishing the linear approximation

$$\mathbf{r}(\mathbf{z}_{k+1}) \approx \mathbf{r}(\mathbf{z}_k) + \mathrm{D}\mathbf{r}(\mathbf{z}_k)[\mathbf{w}] = \mathbf{0}, \tag{A.2}$$

where $\mathrm{D}(\cdot)[\mathbf{w}]$ is the directional derivative in the direction $\mathbf{w}$. The directional derivative on $\mathbf{r}(\mathbf{z}_k)$ yields

$$\mathrm{D}\mathbf{r}(\mathbf{z}_k)[\mathbf{w}] = \mathbf{K}\mathbf{w}, \tag{A.3}$$

where the tangent matrix $\mathbf{K}$ is

$$\mathbf{K}(\mathbf{z}_k) = [K_{ij}(\mathbf{z}_k)],\ K_{ij}(\mathbf{z}_k) = \left.\frac{\partial r_i}{\partial z_j}\right|_{\mathbf{z}_k}. \tag{A.4}$$

On substituting (A.3) into (A.2), a set of linear equations in $\mathbf{w}$ is obtained to be solved in a Newton-Raphson iteration as

$$\mathbf{K}(\mathbf{z}_k)\mathbf{w} = -\mathbf{r}(\mathbf{z}_k),\ \mathbf{z}_{k+1} = \mathbf{z}_k + \mathbf{w}. \tag{A.5}$$

A.3 Linearization of the Weak Form

On considering a reference map χ (see Chapter 5, Section 5.1.1) and a potential energy functional $\Pi(\chi) = 0$, the weak form is given by the directional derivative of $\Pi(\chi)$ in the arbitrary direction $\mathbf{v}$ as

$$\mathrm{D}\Pi(\chi)[\mathbf{v}] \equiv \left.\frac{\partial \Pi(\chi + \epsilon\mathbf{v})}{\partial \epsilon}\right|_{\epsilon=0} = 0, \tag{A.6}$$

which yields a set of nonlinear equations to be linearized using the procedure presented in Appendix A.2. To this end, the directional derivative of (A.6) is taken in the direction $\Delta\mathbf{u}$[1]

[1] We use the notation $\Delta\mathbf{u}$ instead of the simpler $\mathbf{u}$ to indicate that in an incremental procedure like the Newton's method, the displacements are obtained by increments $\Delta\mathbf{u}$ that sum to $\mathbf{u}$ in the final solution. The increment $\Delta\mathbf{u}$ is the incremental solution at a given iteration.

and consider (A.2) to arrive at the linearized weak form as

$$\mathrm{D}\Pi(\chi)[\mathbf{v}] + \mathrm{D}^2\Pi(\chi)[\mathbf{v}, \Delta\mathbf{u}] = 0, \tag{A.7}$$

where $\mathrm{D}^2\Pi(\chi)[\mathbf{v}, \Delta\mathbf{u}] \equiv \mathrm{D}\left\{\mathrm{D}\Pi(\chi)[\mathbf{v}]\right\}[\Delta\mathbf{u}]$. A common practice is to set $\mathbf{v} = \delta\mathbf{u}$, where $\delta\mathbf{u}$ is the so-called vector of *virtual displacements*. When virtual displacements are employed, (A.6) and (A.7) are known as *virtual work* and *linearized virtual work*, respectively.

As an example of the above procedure, consider the weak form in the initial (reference) configuration in terms of the second Piola-Kirchhoff stress and the Green-Lagrange strain tensor given as

$$\mathrm{D}\Pi(\chi)[\mathbf{v}] = \int_\Omega \mathbf{S}(\chi){:}\mathrm{D}\mathbf{E}(\chi)[\mathbf{v}]\, d\Omega - \int_\Omega \mathbf{f}_0 \cdot \mathbf{v}\, d\Omega - \int_{\Gamma_t} \mathbf{t}_0 \cdot \mathbf{v}\, d\Gamma = 0, \tag{A.8}$$

where the vectors of external body forces $\mathbf{f}_0$ and external surface forces $\mathbf{t}_0$ are assumed independent of the motion. The linearization of (A.8) in the direction $\Delta\mathbf{u}$ is

$$\begin{aligned} &\int_\Omega \mathbf{S}(\chi){:}\mathrm{D}\mathbf{E}(\chi)[\mathbf{v}]\, d\Omega - \int_\Omega \mathbf{f}_0 \cdot \mathbf{v}\, d\Omega - \int_{\Gamma_t} \mathbf{t}_0 \cdot \mathbf{v}\, d\Gamma \\ &+ \int_\Omega \mathrm{D}\mathbf{E}(\chi)[\mathbf{v}]{:}D\mathbf{S}(\chi)[\Delta\mathbf{u}]\, d\Omega + \int_\Omega \mathbf{S}(\chi){:}\mathrm{D}^2\mathbf{E}(\chi)[\mathbf{v}, \Delta\mathbf{u}]\, d\Omega \quad = \quad 0, \end{aligned} \tag{A.9}$$

where

$$D\mathbf{S}(\chi)[\Delta\mathbf{u}] = \frac{\partial \mathbf{S}(\chi)}{\partial \mathbf{E}(\chi)}{:}\mathrm{D}\mathbf{E}(\chi)[\Delta\mathbf{u}] = \mathcal{C} : \mathrm{D}\mathbf{E}(\chi)[\Delta\mathbf{u}], \tag{A.10}$$

with $\mathcal{C}$ as the *material elasticity tensor*. In (A.9), $\mathrm{D}^2\mathbf{E}(\chi)[\mathbf{v}, \Delta\mathbf{u}]$ is developed to give (for instance, see Ref. [182])

$$\mathrm{D}^2\mathbf{E}(\chi)[\mathbf{v}, \Delta\mathbf{u}] = \frac{1}{2}[(\boldsymbol{\nabla}^0\mathbf{v})^{\mathrm{T}}\boldsymbol{\nabla}^0\Delta\mathbf{u} + (\boldsymbol{\nabla}^0\Delta\mathbf{u})^{\mathrm{T}}\boldsymbol{\nabla}^0\mathbf{v}]. \tag{A.11}$$

Appendix B

Derivations for the Meshfree F-bar Methodology

B.1 Directional Derivative of the Modified Green-Lagrange Strain Tensor

The detailed derivation of (5.36) is developed. Before proceeding, some expressions are first defined. The following equations are obtained from the standard literature (for instance, see Ref. [182]):

$$\mathrm{D}\mathbf{F}(\chi)[\mathbf{v}] = \boldsymbol{\nabla}^0\mathbf{v}, \tag{B.1}$$

$$\mathrm{D}J(\chi)[\mathbf{v}] = J\mathrm{tr}\left(\boldsymbol{\nabla}^0\mathbf{v}\mathbf{F}^{-1}\right). \tag{B.2}$$

We now consider (B.2) and proceed to take the directional derivative of (5.26) to obtain

$$\mathrm{D}J_a(\chi)[\mathbf{v}] = \frac{\int_\Omega N_a J\mathrm{tr}\left(\boldsymbol{\nabla}^0\mathbf{v}\mathbf{F}^{-1}\right)\,d\Omega}{\int_\Omega N_a\,d\Omega}. \tag{B.3}$$

On considering the operator given in (5.35a) in conjunction with (B.3), the directional derivative of (5.27) yields

$$\mathrm{D}\bar{J}(\chi)[\mathbf{v}] = \theta \left(J \mathrm{tr} \left(\boldsymbol{\nabla}^0 \mathbf{v} \mathbf{F}^{-1} \right) \right). \tag{B.4}$$

Recalling that $\alpha = \left(\bar{J}/J \right)^{1/3}$, its directional derivative is developed with the aid of (B.4) and the operators defined in (5.35) as follows:

$$\begin{aligned} \mathrm{D}\alpha(\chi)[\mathbf{v}] &= \frac{1}{3\alpha^2} \left[\frac{1}{\bar{J}} \mathrm{D}\bar{J}(\chi)[\mathbf{v}] - \frac{\bar{J}}{J^2} \mathrm{D}J(\chi)[\mathbf{v}] \right] \\ &= \frac{1}{3\alpha^2 J} \left[\theta \left(J \mathrm{tr} \left(\boldsymbol{\nabla}^0 \mathbf{v} \mathbf{F}^{-1} \right) \right) - \bar{J} \mathrm{tr} \left(\boldsymbol{\nabla}^0 \mathbf{v} \mathbf{F}^{-1} \right) \right] \\ &= \frac{1}{3} \alpha \, \vartheta \left(J \mathrm{tr} \left(\boldsymbol{\nabla}^0 \mathbf{v} \mathbf{F}^{-1} \right) \right). \end{aligned} \tag{B.5}$$

We are now equipped to develop the directional derivative of the modified Green-Lagrange strain tensor. We continue by taking the directional derivative of (5.31):

$$\mathrm{D}\bar{\mathbf{E}}(\chi)[\mathbf{v}] = \frac{1}{2} \left[\left(\mathrm{D}\bar{\mathbf{F}}(\chi)[\mathbf{v}] \right)^{\mathrm{T}} \bar{\mathbf{F}} + \bar{\mathbf{F}}^{\mathrm{T}} \mathrm{D}\bar{\mathbf{F}}(\chi)[\mathbf{v}] \right]. \tag{B.6}$$

We now make use of (5.28) in conjunction with (B.1) and (B.5) to write

$$\begin{aligned} \mathrm{D}\bar{\mathbf{F}}(\chi)[\mathbf{v}] &= \mathrm{D}\alpha(\chi)[\mathbf{v}] \mathbf{F} + \alpha \mathrm{D}\mathbf{F}(\chi)[\mathbf{v}] \\ &= \frac{1}{3} \alpha \, \vartheta \left(J \mathrm{tr} \left(\boldsymbol{\nabla}^0 \mathbf{v} \mathbf{F}^{-1} \right) \right) \mathbf{F} + \alpha \boldsymbol{\nabla}^0 \mathbf{v}. \end{aligned} \tag{B.7}$$

On substituting (B.7) into (B.6) leads to the final expression for the modified Green-Lagrange strain tensor:

$$\mathrm{D}\bar{\mathbf{E}}(\chi)[\mathbf{v}] = \frac{1}{3} \vartheta \left(J \mathrm{tr} \left(\boldsymbol{\nabla}^0 \mathbf{v} \mathbf{F}^{-1} \right) \right) \bar{\mathbf{F}}^{\mathrm{T}} \bar{\mathbf{F}} + \alpha (\bar{\mathbf{F}}^{\mathrm{T}} \boldsymbol{\nabla}^0 \mathbf{v})_{\mathrm{sym}}. \tag{B.8}$$

B.2 Second Variation of the Modified Energy Functional

The detailed derivation of (5.39) is presented. The directional derivative of the modified second Piola-Kirchhoff stress tensor is first derived. In this process, we use (5.40) in conjunction with (B.8) and proceed as follows:

$$\begin{aligned} \mathrm{D}\bar{\mathbf{S}}(\chi)[\Delta\mathbf{u}] &= \frac{\partial \mathbf{S}(\mathbf{E})}{\partial \mathbf{E}}\left(\bar{\mathbf{E}}(\chi)\right) : \mathrm{D}\bar{\mathbf{E}}(\chi)[\Delta\mathbf{u}] \\ &= \bar{\mathcal{C}} : \mathrm{D}\bar{\mathbf{E}}(\chi)[\Delta\mathbf{u}] \\ &= \frac{1}{3}\vartheta\left(J\mathrm{tr}\left(\boldsymbol{\nabla}^0\Delta\mathbf{u}\mathbf{F}^{-1}\right)\right)\bar{\mathcal{C}} : \left(\bar{\mathbf{F}}^{\mathrm{T}}\bar{\mathbf{F}}\right) + \alpha\bar{\mathcal{C}} : \left(\bar{\mathbf{F}}^{\mathrm{T}}\boldsymbol{\nabla}^0\Delta\mathbf{u}\right)_{\mathrm{sym}}. \end{aligned} \tag{B.9}$$

Next, the definition of the directional derivative of the inverse of a tensor [182] is used to write

$$\mathrm{D}\mathbf{F}^{-1}(\chi)[\Delta\mathbf{u}] = -\mathbf{F}^{-1}\boldsymbol{\nabla}^0\Delta\mathbf{u}\mathbf{F}^{-1}, \tag{B.10}$$

which is employed along with (B.2) in the derivation of the following directional derivative:

$$\begin{aligned} \mathrm{D}\left(J\mathrm{tr}\left(\boldsymbol{\nabla}^0\mathbf{v}\mathbf{F}^{-1}\right)\right)[\Delta\mathbf{u}] &= \mathrm{D}J(\chi)[\Delta\mathbf{u}]\mathrm{tr}\left(\boldsymbol{\nabla}^0\mathbf{v}\mathbf{F}^{-1}\right) + J\mathrm{tr}\left(\boldsymbol{\nabla}^0\mathbf{v}\mathrm{D}\mathbf{F}^{-1}(\chi)[\Delta\mathbf{u}]\right) \\ &= J\left[\mathrm{tr}\left(\boldsymbol{\nabla}^0\mathbf{v}\mathbf{F}^{-1}\right)\mathrm{tr}\left(\boldsymbol{\nabla}^0\Delta\mathbf{u}\mathbf{F}^{-1}\right) - \mathrm{tr}\left(\boldsymbol{\nabla}^0\mathbf{v}\mathbf{F}^{-1}\boldsymbol{\nabla}^0\Delta\mathbf{u}\mathbf{F}^{-1}\right)\right]. \end{aligned} \tag{B.11}$$

The next expressions that need to be developed are the directional derivatives of the operators that were defined in (5.35). With the aid of (B.11) the following expression is obtained for the operator (5.35a):

$$\begin{aligned} \mathrm{D}\theta\left(J\mathrm{tr}\left(\boldsymbol{\nabla}^0\mathbf{v}\mathbf{F}^{-1}\right)\right)[\Delta\mathbf{u}] &= \theta\left(J\mathrm{tr}\left(\boldsymbol{\nabla}^0\mathbf{v}\mathbf{F}^{-1}\right)\mathrm{tr}\left(\boldsymbol{\nabla}^0\Delta\mathbf{u}\mathbf{F}^{-1}\right)\right) \\ &\quad - \theta\left(J\mathrm{tr}\left(\boldsymbol{\nabla}^0\mathbf{v}\mathbf{F}^{-1}\boldsymbol{\nabla}^0\Delta\mathbf{u}\mathbf{F}^{-1}\right)\right). \end{aligned} \tag{B.12}$$

Now, we apply the directional derivative on the operator (5.35b) and make use of (B.12) along with (B.2), (B.4) and (B.11) to arrive at the following expression:

$$\begin{aligned}
\mathrm{D}\vartheta\left(J\mathrm{tr}\left(\boldsymbol{\nabla}^0\mathbf{v}\mathbf{F}^{-1}\right)\right)[\Delta\mathbf{u}] \;=\;& -\frac{1}{\bar{J}^2}\,\theta\left(J\mathrm{tr}(\boldsymbol{\nabla}^0\mathbf{v}\mathbf{F}^{-1})\right)\theta\left(J\mathrm{tr}(\boldsymbol{\nabla}^0\Delta\mathbf{u}\mathbf{F}^{-1})\right)\\
&+\frac{1}{\bar{J}}\,\theta\left(J\mathrm{tr}(\boldsymbol{\nabla}^0\mathbf{v}\mathbf{F}^{-1})\mathrm{tr}(\boldsymbol{\nabla}^0\Delta\mathbf{u}\mathbf{F}^{-1})\right)\\
&-\frac{1}{\bar{J}}\,\theta\left(J\mathrm{tr}(\boldsymbol{\nabla}^0\mathbf{v}\mathbf{F}^{-1}\boldsymbol{\nabla}^0\Delta\mathbf{u}\mathbf{F}^{-1})\right)\\
&+\mathrm{tr}(\boldsymbol{\nabla}^0\mathbf{v}\mathbf{F}^{-1}\boldsymbol{\nabla}^0\Delta\mathbf{u}\mathbf{F}^{-1}).
\end{aligned}\tag{B.13}$$

Next, observing that $\mathrm{D}\left(\bar{\mathbf{F}}^{\mathrm{T}}\bar{\mathbf{F}}\right)[\mathbf{v}] = 2\mathrm{D}\bar{\mathbf{E}}[\mathbf{v}]$ and employing (B.13), yields the following directional derivative:

$$\begin{aligned}
\mathrm{D}\left(\vartheta\left(J\mathrm{tr}\left(\boldsymbol{\nabla}^0\mathbf{v}\mathbf{F}^{-1}\right)\right)\bar{\mathbf{F}}^{\mathrm{T}}\bar{\mathbf{F}}\right)[\Delta\mathbf{u}] \;=\;& -\frac{1}{\bar{J}^2}\,\theta\left(J\mathrm{tr}(\boldsymbol{\nabla}^0\mathbf{v}\mathbf{F}^{-1})\right)\theta\left(J\mathrm{tr}(\boldsymbol{\nabla}^0\Delta\mathbf{u}\mathbf{F}^{-1})\right)\bar{\mathbf{F}}^{\mathrm{T}}\bar{\mathbf{F}}\\
&+\frac{1}{\bar{J}}\,\theta\left(J\mathrm{tr}(\boldsymbol{\nabla}^0\mathbf{v}\mathbf{F}^{-1})\mathrm{tr}(\boldsymbol{\nabla}^0\Delta\mathbf{u}\mathbf{F}^{-1})\right)\bar{\mathbf{F}}^{\mathrm{T}}\bar{\mathbf{F}}\\
&-\frac{1}{\bar{J}}\,\theta\left(J\mathrm{tr}(\boldsymbol{\nabla}^0\mathbf{v}\mathbf{F}^{-1}\boldsymbol{\nabla}^0\Delta\mathbf{u}\mathbf{F}^{-1})\right)\bar{\mathbf{F}}^{\mathrm{T}}\bar{\mathbf{F}}\\
&+\mathrm{tr}(\boldsymbol{\nabla}^0\mathbf{v}\mathbf{F}^{-1}\boldsymbol{\nabla}^0\Delta\mathbf{u}\mathbf{F}^{-1})\bar{\mathbf{F}}^{\mathrm{T}}\bar{\mathbf{F}}\\
&+\frac{2}{3}\vartheta\left(J\mathrm{tr}(\boldsymbol{\nabla}^0\mathbf{v}\mathbf{F}^{-1})\right)\vartheta\left(J\mathrm{tr}(\boldsymbol{\nabla}^0\Delta\mathbf{u}\mathbf{F}^{-1})\right)\bar{\mathbf{F}}^{\mathrm{T}}\bar{\mathbf{F}}\\
&+2\alpha\,\vartheta\left(J\mathrm{tr}(\boldsymbol{\nabla}^0\mathbf{v}\mathbf{F}^{-1})\right)(\bar{\mathbf{F}}^{\mathrm{T}}\boldsymbol{\nabla}^0\Delta\mathbf{u})_{\mathrm{sym}}.
\end{aligned}\tag{B.14}$$

One more directional derivative is needed to complete the derivation. To this end, (B.5) and (B.7) are considered in the derivation of

$$\begin{aligned}
\mathrm{D}\left(\alpha(\bar{\mathbf{F}}^{\mathrm{T}}\boldsymbol{\nabla}^0\mathbf{v})_{\mathrm{sym}}\right)[\Delta\mathbf{u}] \;=\;& +\frac{1}{3\alpha^2 J}(\bar{\mathbf{F}}^{\mathrm{T}}\boldsymbol{\nabla}^0\mathbf{v})_{\mathrm{sym}}\theta\left(J\mathrm{tr}(\boldsymbol{\nabla}^0\Delta\mathbf{u}\mathbf{F}^{-1})\right)\\
&-\frac{1}{3}\alpha(\bar{\mathbf{F}}^{\mathrm{T}}\boldsymbol{\nabla}^0\mathbf{v})_{\mathrm{sym}}\mathrm{tr}(\boldsymbol{\nabla}^0\Delta\mathbf{u}\mathbf{F}^{-1})\\
&+\frac{1}{3}\alpha(\bar{\mathbf{F}}^{\mathrm{T}}\boldsymbol{\nabla}^0\mathbf{v})_{\mathrm{sym}}\vartheta\left(J\mathrm{tr}(\boldsymbol{\nabla}^0\Delta\mathbf{u}\mathbf{F}^{-1})\right)\\
&+\alpha^2\left((\boldsymbol{\nabla}^0\Delta\mathbf{u})^{\mathrm{T}}\boldsymbol{\nabla}^0\mathbf{v}\right)_{\mathrm{sym}}.
\end{aligned}\tag{B.15}$$

The last step is to take the second variation of (5.30), or equivalently, the directional derivative of (5.37). The derivation is split into a material and a geometric part and motion-independent external forces are assumed. This leads to

$$\begin{aligned}\left(\mathrm{D}^2\bar{\Pi}(\chi)[\mathbf{v},\Delta\mathbf{u}]\right)_{\mathrm{mat}} &= +\frac{1}{3}\int_\Omega \vartheta\left(J\mathrm{tr}(\boldsymbol{\nabla}^0\mathbf{v}\mathbf{F}^{-1})\right)(\bar{\mathbf{F}}^{\mathrm{T}}\bar{\mathbf{F}}) : \mathrm{D}\bar{\mathbf{S}}(\chi)[\Delta\mathbf{u}]\,d\Omega \\ &\quad + \int_\Omega \alpha(\bar{\mathbf{F}}^{\mathrm{T}}\boldsymbol{\nabla}^0\mathbf{v})_{\mathrm{sym}} : \mathrm{D}\bar{\mathbf{S}}(\chi)[\Delta\mathbf{u}]\,d\Omega, \end{aligned} \tag{B.16}$$

$$\begin{aligned}\left(\mathrm{D}^2\bar{\Pi}(\chi)[\mathbf{v},\Delta\mathbf{u}]\right)_{\mathrm{geo}} &= +\frac{1}{3}\int_\Omega \bar{\mathbf{S}} : \mathrm{D}\left(\vartheta\left(J\mathrm{tr}\left(\boldsymbol{\nabla}^0\mathbf{v}\mathbf{F}^{-1}\right)\right)\bar{\mathbf{F}}^{\mathrm{T}}\bar{\mathbf{F}}\right)[\Delta\mathbf{u}] \\ &\quad + \int_\Omega \bar{\mathbf{S}} : \mathrm{D}\left(\alpha(\bar{\mathbf{F}}^{\mathrm{T}}\boldsymbol{\nabla}^0\mathbf{v})_{\mathrm{sym}}\right)[\Delta\mathbf{u}]\,d\Omega. \end{aligned} \tag{B.17}$$

Finally, on substituting (B.9) into (B.16) yields the material part of the second variation that was presented in (5.39b):

$$\begin{aligned}\left(\mathrm{D}^2\bar{\Pi}(\chi)[\mathbf{v},\Delta\mathbf{u}]\right)_{\mathrm{mat}} &= +\frac{1}{9}\int_\Omega \vartheta\left(J\mathrm{tr}(\boldsymbol{\nabla}^0\mathbf{v}\mathbf{F}^{-1})\right)\vartheta\left(J\mathrm{tr}(\boldsymbol{\nabla}^0\Delta\mathbf{u}\mathbf{F}^{-1})\right)(\bar{\mathbf{F}}^{\mathrm{T}}\bar{\mathbf{F}}) : \bar{\mathcal{C}} : (\bar{\mathbf{F}}^{\mathrm{T}}\bar{\mathbf{F}})\,d\Omega \\ &\quad + \frac{1}{3}\int_\Omega \alpha\,\vartheta\left(J\mathrm{tr}(\boldsymbol{\nabla}^0\mathbf{v}\mathbf{F}^{-1})\right)(\bar{\mathbf{F}}^{\mathrm{T}}\bar{\mathbf{F}}) : \bar{\mathcal{C}} : (\bar{\mathbf{F}}^{\mathrm{T}}\boldsymbol{\nabla}^0\Delta\mathbf{u})_{\mathrm{sym}}\,d\Omega \\ &\quad + \frac{1}{3}\int_\Omega \alpha(\bar{\mathbf{F}}^{\mathrm{T}}\boldsymbol{\nabla}^0\mathbf{v})_{\mathrm{sym}} : \bar{\mathcal{C}} : (\bar{\mathbf{F}}^{\mathrm{T}}\bar{\mathbf{F}})\,\vartheta\left(J\mathrm{tr}(\boldsymbol{\nabla}^0\Delta\mathbf{u}\mathbf{F}^{-1})\right)\,d\Omega \\ &\quad + \int_\Omega \alpha^2(\bar{\mathbf{F}}^{\mathrm{T}}\boldsymbol{\nabla}^0\mathbf{v})_{\mathrm{sym}} : \bar{\mathcal{C}} : (\bar{\mathbf{F}}^{\mathrm{T}}\boldsymbol{\nabla}^0\Delta\mathbf{u})_{\mathrm{sym}}\,d\Omega, \end{aligned} \tag{B.18}$$

and on substituting (B.14) and (B.15) into (B.17) leads to the corresponding geometric part that was presented in (5.39c):

$$
\begin{aligned}
\big(\mathrm{D}^2\bar{\Pi}(\chi)[\mathbf{v},\Delta\mathbf{u}]\big)_{\mathrm{geo}} \;=\; & -\frac{1}{3}\int_\Omega \frac{1}{\bar{J}^2}\,\theta\left(J\mathrm{tr}(\boldsymbol{\nabla}^0\mathbf{v}\mathbf{F}^{-1})\right)\theta\left(J\mathrm{tr}(\boldsymbol{\nabla}^0\Delta\mathbf{u}\mathbf{F}^{-1})\right)\bar{\mathbf{S}} : (\bar{\mathbf{F}}^{\mathrm{T}}\bar{\mathbf{F}})\,d\Omega \\
& + \frac{1}{3}\int_\Omega \frac{1}{\bar{J}}\,\theta\left(J\mathrm{tr}(\boldsymbol{\nabla}^0\mathbf{v}\mathbf{F}^{-1})\mathrm{tr}(\boldsymbol{\nabla}^0\Delta\mathbf{u}\mathbf{F}^{-1})\right)\bar{\mathbf{S}} : (\bar{\mathbf{F}}^{\mathrm{T}}\bar{\mathbf{F}})\,d\Omega \\
& - \frac{1}{3}\int_\Omega \frac{1}{\bar{J}}\,\theta\left(J\mathrm{tr}(\boldsymbol{\nabla}^0\mathbf{v}\mathbf{F}^{-1}\boldsymbol{\nabla}^0\Delta\mathbf{u}\mathbf{F}^{-1})\right)\bar{\mathbf{S}} : (\bar{\mathbf{F}}^{\mathrm{T}}\bar{\mathbf{F}})\,d\Omega \\
& + \frac{1}{3}\int_\Omega \mathrm{tr}(\boldsymbol{\nabla}^0\mathbf{v}\mathbf{F}^{-1}\boldsymbol{\nabla}^0\Delta\mathbf{u}\mathbf{F}^{-1})\bar{\mathbf{S}} : (\bar{\mathbf{F}}^{\mathrm{T}}\bar{\mathbf{F}})\,d\Omega \\
& + \frac{2}{9}\int_\Omega \vartheta\left(J\mathrm{tr}(\boldsymbol{\nabla}^0\mathbf{v}\mathbf{F}^{-1})\right)\vartheta\left(J\mathrm{tr}(\boldsymbol{\nabla}^0\Delta\mathbf{u}\mathbf{F}^{-1})\right)\bar{\mathbf{S}} : (\bar{\mathbf{F}}^{\mathrm{T}}\bar{\mathbf{F}})\,d\Omega \\
& + \frac{2}{3}\int_\Omega \alpha\,\vartheta\left(J\mathrm{tr}(\boldsymbol{\nabla}^0\mathbf{v}\mathbf{F}^{-1})\right)\bar{\mathbf{S}} : (\bar{\mathbf{F}}^{\mathrm{T}}\boldsymbol{\nabla}^0\Delta\mathbf{u})_{\mathrm{sym}}\,d\Omega \\
& + \frac{2}{3}\int_\Omega \alpha(\bar{\mathbf{F}}^{\mathrm{T}}\boldsymbol{\nabla}^0\mathbf{v})_{\mathrm{sym}} : \bar{\mathbf{S}}\,\vartheta\left(J\mathrm{tr}(\boldsymbol{\nabla}^0\Delta\mathbf{u}\mathbf{F}^{-1})\right)\,d\Omega \\
& + \int_\Omega \alpha^2\bar{\mathbf{S}} : [(\boldsymbol{\nabla}^0\mathbf{v})^{\mathrm{T}}\boldsymbol{\nabla}^0\Delta\mathbf{u}]_{\mathrm{sym}}\,d\Omega. \qquad \text{(B.19)}
\end{aligned}
$$

Appendix C

Newton-Based Methods for the Solution of Nonlinear Systems

C.1 Introduction

The methodology to solve nonlinear system of equations by means of Newton's method was summarized in Appendix A.2. Here, different approaches are considered to implement the Newton's formula (A.5). The Newton's formula corresponding to the problems considered in this dissertation is given in (5.41). For convenience, it is rewritten here again as follows:

$$ {}^{t+\Delta t}\mathbf{K}^{(i-1)}\Delta\mathbf{u}^{(i)} = {}^{t+\Delta t}\mathbf{F} - {}^{t+\Delta t}\mathbf{T}^{(i-1)}, \tag{C.1a} $$

$$ \mathbf{K} = \mathbf{K}_{\text{mat}} + \mathbf{K}_{\text{geo}}, \tag{C.1b} $$

where $t + \Delta t$ is to indicate that the material and geometric tangent stiffness matrices, $\mathbf{K}_{\text{mat}}$ and $\mathbf{K}_{\text{geo}}$, respectively, and the external and internal nodal force vectors, $\mathbf{F}$ and $\mathbf{T}$, respectively, are computed incrementally by application of boundary conditions (forces and displacements) in increments. An increment defines a step. On the other hand, i stands for the equilibrium iterations that are involved within a step. An initial tangent

stiffness matrix and an initial residual force vector are usually computed in the reference configuration ($\mathbf{u} = \mathbf{0}$) to start the iterations. The tangent stiffness matrix and residual force vector are updated (reformed) as iterations go on. The reformation of the residual force vector is carried out at every iteration with the most updated solution. However, the reformation of the tangent stiffness matrix can take place after a selected number of iterations or steps. Moreover, the tangent stiffness matrix can be approximated, again at every iteration or after a selected number of iterations or steps. These options to compute the tangent stiffness matrix lead to different procedures. Some of them are summarized in the following sections of this appendix. Once the iterations are started, they are continued until appropriate convergence criteria are satisfied. Some of these criteria are discussed later in this appendix. The solution is then computed as

$$\mathbf{u}^{(i+1)} = \mathbf{u}^{(i)} + \alpha \Delta \mathbf{u}^{(i)}, \tag{C.2}$$

where $0 < \alpha \leq 1$ is a relaxation parameter that attempts to find the length of the Newton direction $\Delta \mathbf{u}$ that gives a better solution update. This slows convergence but increases the possibility to converge to a solution, especially when convergence is difficult to achieve with $\alpha = 1$. To find α, so-called line search techniques are employed. In this dissertation, the Illinois algorithm [183] has been employed as the line search technique.

C.2 Newton-Raphson Method

In the Newton-Raphson method (also known as full Newton or Newton's method), the material and geometric tangent stiffness matrices are reformed (assembled) at every iteration. The Newton's formula for the Newton-Raphson method reads exactly as in (C.1). Although reformation at every iteration can be an expensive task, the Newton-Raphson method is attractive since it provides quadratic convergence to the solution if the initial guess (usually chosen as $\mathbf{u} = \mathbf{0}$) is sufficiently close to the solution.

C.3 Modified Newton-Raphson Method

A more inexpensive alternative to the Newton-Raphson method is the modified Newton-Raphson method. The main idea consists in reforming the tangent stiffness matrix only few times during the analysis. For instance, the tangent stiffness matrix can be computed one time in the initial (reference) configuration ($\mathbf{u} = \mathbf{0}$), and be employed as is for the rest of the analysis. The foregoing method is referred to as the *initial stress method* [16] and its Newton's formula becomes

$$ {}^{0}\mathbf{K}_{\text{mat}} \Delta \mathbf{u}^{(i)} = {}^{t+\Delta t}\mathbf{F} - {}^{t+\Delta t}\mathbf{T}^{(i-1)}, \tag{C.3} $$

where ${}^{0}\mathbf{K}_{\text{mat}}$ stands for the material tangent stiffness matrix evaluated in the initial (reference) configuration[1]. However, the convergence of this method is slowed, and therefore it requires greater number of iterations within each step to achieve convergence.

In a more general view, the Newton's formula for the modified Newton-Raphson method is given as

$$ {}^{\tau}\mathbf{K}^{(i-1)} = {}^{t+\Delta t}\mathbf{F} - {}^{t+\Delta t}\mathbf{T}^{(i-1)}, \tag{C.4} $$

where τ corresponds to one of the accepted equilibrium configurations at time 0, Δt, $2\Delta t$, $\ldots$, or t. The modified Newton-Raphson method involves less tangent stiffness reformations than in the Newton-Raphson method. However, its convergence is slowed. The number of reformations depends on the degree of nonlinearity in the system response. The more nonlinear the response, the more often the reformations should be performed.

C.4 Broyden's Method

Instead of reforming the tangent stiffness matrix, an approximation to it can be employed. The approximation is termed secant matrix because in one dimension it reduces to a secant

[1] Notice that the geometric tangent stiffness matrix is a null matrix in the initial configuration, and therefore it does not appear in (C.3).

method. Procedures that attempt to approximate the tangent stiffness matrix are grouped within so-called quasi-Newton methods. Broyden's method [184] is one alternative that belongs to quasi-Newton methods. Its Newton's formula is (C.1) with $\mathbf{K}$ being a secant matrix rather than a tangent matrix. The secant matrix is updated every time on using the last known solution. However, the update is inexpensive since it only involves an assembly procedure on an initial tangent stiffness matrix, which is usually chosen as ${}^{0}\mathbf{K}_{\text{mat}}$. The secant matrices are then computed using a recursive formula on the initial tangent stiffness matrix. The Broyden's update is computed as follows:

$$\mathbf{R}^{(i-1)} = -\left({}^{t+\Delta t}\mathbf{T}^{(i-1)} - {}^{t+\Delta t}\mathbf{F}\right), \tag{C.5}$$

$$\Delta\mathbf{u}^{(i-1)} = \mathbf{u}^{(i)} - \mathbf{u}^{(i-1)}, \tag{C.6}$$

$$\Delta\mathbf{R}^{(i-1)} = \mathbf{R}^{(i)} - \mathbf{R}^{(i-1)}, \tag{C.7}$$

$$\mathbf{K}^{(i)} = \mathbf{K}^{(i-1)} + \frac{\left(\Delta\mathbf{R}^{(i-1)} - \mathbf{K}^{(i-1)} \cdot \Delta\mathbf{u}^{(i-1)}\right) \otimes \Delta\mathbf{u}^{(i-1)}}{\Delta\mathbf{u}^{(i-1)} \cdot \Delta\mathbf{u}^{(i-1)}}. \tag{C.8}$$

C.5 BFGS Method

The BFGS method [178] is another alternative that belongs to quasi-Newton methods. It operates similarly to Broyden's method. The only distinction is that the update procedure is computed as follows:

$$\mathbf{K}^{(i)} = \mathbf{K}^{(i-1)} + \frac{\Delta\mathbf{R}^{(i-1)} \otimes \Delta\mathbf{R}^{(i-1)}}{\Delta\mathbf{R}^{(i-1)} \cdot \Delta\mathbf{u}^{(i-1)}} - \frac{\left(\mathbf{K}^{(i-1)} \cdot \Delta\mathbf{u}^{(i-1)}\right) \otimes \left(\mathbf{K}^{(i-1)} \cdot \Delta\mathbf{u}^{(i-1)}\right)}{\Delta\mathbf{u}^{(i-1)} \cdot \mathbf{K}^{(i-1)} \cdot \Delta\mathbf{u}^{(i-1)}}. \tag{C.9}$$

C.6 Convergence Criteria

Typical convergence criteria are based on displacement or residual norms. A displacement criterion is the following:

$$e_D = \sqrt{\frac{\Delta\mathbf{u}^{(i)} \cdot \Delta\mathbf{u}^{(i)}}{\mathbf{u}^{(i+1)} \cdot \mathbf{u}^{(i+1)}}}, \tag{C.10}$$

whereas a residual criterion is

$$e_R = \frac{1}{n}\sqrt{\mathbf{R}^{(i)} \cdot \mathbf{R}^{(i)}}, \tag{C.11}$$

where n is the total number of nodes in the domain of analysis. The equilibrium iterations are terminated when preset tolerances are satisfied. A common technique is to check convergence on both norms as $e_D < Dtol$ and $e_R < Rtol$, where $Dtol$ and $Rtol$ are the displacement and residual tolerances, respectively. However, most of the times the former suffices.

C.7 Practical Implementation of Nonlinear Solvers

Numerical tests reveal that a combination of the nonlinear solvers described above performs better than any of the solvers by themselves. Most of the examples in this dissertation have been solved using a nonlinear solver in which the modified Newton-Raphson method is combined with the Broyden's or BFGS method. The second combination performed better in most of the cases. Additionally, the geometric part of the tangent or secant stiffness matrix is usually disregarded. A typical sequence starts at the beginning of a step with a reformation of the tangent stiffness matrix with the last known solution. In the rest of the iterations of that step, and in all the iterations of the next 5 or 10 steps, only BFGS updates are employed. That sequence is repeated during the entire analysis. If at some point the solution diverges before the preset number of BFGS steps is completed, a reduction in that number is considered until convergence is restored. This scheme usually requires many more steps and iterations than the Newton-Raphson method. However, the inexpensive computations that are involved in the Broyden's or BFGS updates vastly reduce the analysis time, which makes the scheme robust for nonlinear analysis.

References

[1] Li S, Liu WK. *Meshfree Particle Methods*. Springer: Germany, 2004.

[2] Liu GR. *Meshfree Methods: Moving Beyond the Finite Element Method*. Second edn., CRC Press: Boca Raton, FL, 2010.

[3] Dolbow J, Belytschko T. Numerical integration of Galerkin weak form in meshfree methods. *Computational Mechanics* 1999; **23**(3):219–230.

[4] Sukumar N, Moran B, Belytschko T. The natural element method in solid mechanics. *International Journal for Numerical Methods in Engineering* 1998; **43**(5):839–887.

[5] Atluri SN, Zhu T. A new meshless local Petrov-Galerkin (MLPG) approach in computational mechanics. *Computational Mechanics* 1998; **22**(2):117–127.

[6] De S, Bathe KJ. The method of finite spheres with improved numerical integration. *Computers and Structures* 2001; **79**(22–25):2183–2196.

[7] Hughes TJR. *The Finite Element Method: Linear Static and Dynamic Finite Element Analysis*. Dover Publications, Inc: Mineola, NY, 2000.

[8] Hughes TJR. Generalization of selective integration procedures to anisotropic and non-linear media. *International Journal for Numerical Methods in Engineering* 1980; **15**(9):1413–1418.

[9] Malkus DS, Hughes TJR. Mixed finite element methods – reduced and selective integration techniques: a unification of concepts. *Computer Methods in Applied Mechanics and Engineering* 1978; **15**(1):63–81.

[10] Simo JC, Rifai S. A class of mixed assumed strain methods and the method of incompatible modes. *International Journal for Numerical Methods in Engineering* 1990; **29**(8):1595–1638.

[11] Simo JC, Hughes TJR. On the variational foundations of assumed strain methods. *Journal of Applied Mechanics* 1986; **53**(1):51–54.

[12] Elguedj T, Bazilevs Y, Calo V, Hughes TJR. $\bar{B}$-bar and $\bar{F}$-bar projection methods for nearly incompressible linear and non-linear elasticity and plasticity using higher-order NURBS elements. *Computer Methods in Applied Mechanics and Engineering* 2008; **1**(33–40):2667–3172.

[13] Brezzi F. On the existence, uniqueness and approximation of saddle-point problems arising from Lagrangian multipliers. *RAIRO, Analyse Numérique* 1974; **8**:129–151.

[14] Ladyzhenskaya OA. *The Mathematical Theory of Viscous Incompressible Flows*. Gordon and Breach: London, 1969.

[15] Babuška I. The finite element method with Lagrangian multipliers. *Numerische Mathematik* 1973; **20**(3):179–192.

[16] Bathe KJ. *Finite Element Procedures*. Prentice Hall: Englewood Cliffs, NJ, 1996.

[17] Chapelle D, Bathe KJ. The inf-sup test. *Computers and Structures* 1993; **47**(4–5):537–545.

[18] Brezzi F, Pitkäranta J. On the stabilization of finite element approximations of the Stokes equations. *In: W. Hackbusch (Ed.), Efficient solutions of elliptic systems. Notes on numerical fluid mechanics* 1984; **10**:11–19.

[19] Hughes TJR, Franca LP, Balestra M. A new finite element formulation for computational fluid dynamics: V. Circumventing the Babuška-Brezzi condition: a stable Petrov-Galerkin formulation of the Stokes problem accommodating equal-order interpolations. *Computer Methods in Applied Mechanics and Engineering* 1986; **59**(1):85–99.

[20] Bathe KJ. The inf-sup condition and its evaluation for mixed finite element methods. *Computers and Structures* 2001; **79**(9):243–252.

[21] Nayroles B, Touzot G, Villon P. Generalizing the finite element method: Diffuse approximation and diffuse elements. *Computational Mechanics* 1992; **10**:307–318.

[22] Belytschko T, Lu YY, Gu L. Element-free Galerkin methods. *International Journal for Numerical Methods in Engineering* 1994; **37**(2):229–256.

[23] Liu WK, Jun S, Zhang YF. Reproducing kernel particle methods. *International Journal for Numerical Methods in Engineering* 1995; **20**(8–9):1081–1106.

[24] Liszka TJ, Duarte CA, Tworzydlo WW. *hp*-meshless cloud method. *Computer Methods in Applied Mechanics and Engineering* 1996; **139**(1–4):263–288.

[25] Sukumar N, Moran B, Semenov AY, Belikov VV. Natural neighbour Galerkin methods. *International Journal for Numerical Methods in Engineering* 2001; **50**(1):1–27.

[26] De S, Bathe KJ. The method of finite spheres. *Computational Mechanics* 2000; **25**(4):329–345.

[27] Arroyo M, Ortiz M. Local maximum-entropy approximation schemes: a seamless bridge between finite elements and meshfree methods. *International Journal for Numerical Methods in Engineering* 2006; **65**(13):2167–2202.

[28] Huerta A, Fernández-Méndez S. Locking in the incompressible limit for the element-free Galerkin method. *International Journal for Numerical Methods in Engineering* 2001; **51**(11):1361–1383.

[29] Dolbow J, Belytschko T. Volumetric locking in the element free Galerkin method. *International Journal for Numerical Methods in Engineering* 1999; **46**(6):925–942.

[30] González D, Cueto E, Doblaré M. Volumetric locking in natural neighbour Galerkin methods. *International Journal for Numerical Methods in Engineering* 2004; **61**(4):611–632.

[31] Vidal Y, Villon P, Huerta A. Locking in the incompressible limit: pseudo-divergence-free element free Galerkin. *Communications in Numerical Methods in Engineering* 2003; **19**(9):725–735.

[32] Recio DP, Jorge RMN, Dinis LMS. Locking and hourglass phenomena in an element-free Galerkin context: the B-bar method with stabilization and an enhanced strain method. *International Journal for Numerical Methods in Engineering* 2006; **68**(13):1329–1357.

[33] Beissel S, Belytschko T. Nodal integration of the element-free Galerkin method. *Computer Methods in Applied Mechanics and Engineering* 1996; **139**(1):49–74.

[34] Chen JS, Wu CT, Yoon S, You Y. A stabilized conforming nodal integration for Galerkin mesh-free methods. *International Journal for Numerical Methods in Engineering* 2001; **50**(2):435–466.

[35] Chen JS, Hu W, Puso M. Orbital HP-clouds for solving Schrödinger equation in quantum mechanics. *Computer Methods in Applied Mechanics and Engineering* 2007; **196**(37–40):3693–3705.

[36] Puso MA, Chen JS, Zywicz E, Elmer W. Meshfree and finite element nodal integration methods. *International Journal for Numerical Methods in Engineering* 2008; **74**(3):416–446.

[37] Kucherov L, Tadmor EB, Miller RE. Umbrella spherical integration: a stable meshless method for non-linear solids. *International Journal for Numerical Methods in Engineering* 2007; **69**(13):2807–2847.

[38] Belytschko T, Guo Y, Liu WK, Xiao SP. A unified stability analysis of meshless particle methods. *International Journal for Numerical Methods in Engineering* 2000; **48**(9):1359–1400.

[39] Belytschko T, Xiao S. Stability analysis of particle methods with corrected derivatives. *Computers and Mathematics with Applications* 2002; **43**(3–5):329–350.

[40] Fries TP, Belytschko T. Convergence and stabilization of stress-point integration in mesh-free and particle methods. *International Journal for Numerical Methods in Engineering* 2008; **74**(7):1067–1087.

[41] Brezzi F, Fortin M. *Mixed and Hybrid Finite Element Methods*. Springer: NY, 1991.

[42] Boffi D, Brezzi F, Demkowicz LF, Durn RG, Falk RS, Fortin M. *Mixed Finite Elements, Compatibility Conditions, and Applications. Edited by D. Boffi and L. Gastaldi. Lecture Notes in Mathematics, 1939*. Springer-Verlag, Berlin Fondazione C.I.M.E., Florence, 2008.

[43] Li J, Yinnian H, Chen Z. Performance of several stabilized finite element methods for the Stokes equations based on the lowest equal-order pairs. *Computing* 2009; **86**(1):37–51.

[44] De S, Bathe KJ. Displacement/pressure mixed interpolation in the method of finite spheres. *International Journal for Numerical Methods in Engineering* 2001; **51**(3):275–292.

[45] Fries TP, Matthies HG. A stabilized and coupled meshfree/meshbased method for the incompressible Navier-Stokes equations-Part I: Stabilization. *Computer Methods in Applied Mechanics and Engineering* 2006; **195**(44–47):6205–6224.

[46] Li X, Duan Q. Meshfree iterative stabilized Taylor-Galerkin and characteristic-based split (CBS) algorithms for incompressible NS equations. *Computer Methods in Applied Mechanics and Engineering* 2006; **195**(44–47):6125–6145.

[47] Zhang L, Ouyang J, Zhang XH, Zhang WB. On a multi-scale element-free Galerkin method for the Stokes problem. *Applied Mathematics and Computation* 2008; **203**(2):745–753.

[48] Krysl P, Zhu B. Locking-free continuum displacement finite elements with nodal integration. *International Journal for Numerical Methods in Engineering* 2008; **76**(7):1020–1043.

[49] Zienkiewicz OC, Taylor RL. *The Finite Element Method, Volume 1: The Basis*. Fifth edn., Butterworth-Heinemann: Oxford, UK, 2000.

[50] Field DA. Qualitative measures for initial meshes. *International Journal for Numerical Methods in Engineering* 2000; **47**(4):887–906.

[51] Knupp PM. Algebraic mesh quality metrics for unstructured initial meshes. *Finite Elements in Analysis and Design* 2003; **39**(3):217–241.

[52] Lo SH. A new mesh generation scheme for arbitrary planar domains. *International Journal for Numerical Methods in Engineering* 1985; **21**(8):1403–1426.

[53] Löhner R, Parikh P. Generation of three-dimensional unstructured grids by the advancing-front method. *International Journal for Numerical Methods in Fluids* 1988; **8**(10):1135–1149.

[54] Jin H, Tanner RI. Generation of unstructured tetrahedral meshes by advancing front technique. *International Journal for Numerical Methods in Engineering* 1993; **36**(11):1805–1823.

[55] Caendish JC, Field DA, Frey WH. An apporach to automatic three-dimensional finite element mesh generation. *International Journal for Numerical Methods in Engineering* 1985; **21**(2):329–347.

[56] Weatherill NP. A method for generating irregular computational grids in multiply connected planar domains. *International Journal for Numerical Methods in Fluids* 1988; **8**(2):181–197.

[57] Schroeder WJ, Shephard MS. Geometry-based fully automatic mesh generation and the delaunay triangulation. *International Journal for Numerical Methods in Engineering* 1988; **26**(11):2503–2515.

[58] Baker T. Automatic mesh generation for complex three-dimensional regions using a constrained delaunay triangulation. *Engineering with Computers* 1989; **5**:161–175.

[59] Simo JC, Taylor RL, Pister KS. Variational and projection methods for the volume constraint in finite deformation elasto-plasticity. *Computer Methods in Applied Mechanics and Engineering* 1985; **51**(1–3):177–208.

[60] Simo JC, Armero F. Geometrically non-linear enhanced strain mixed methods and the method of incompatible modes. *International Journal for Numerical Methods in Engineering* 1992; **33**(7):1413–1449.

[61] Sussman T, Bathe KJ. A finite element formulation for nonlinear incompressible elastic and inelastic analysis. *Computers and Structures* 1987; **26**(1–2):357–409.

[62] Hughes TJ, Taylor RL, Sackman JL. Finite element formulation and solution of contact-impact problems in Continuum Mechanics-III. *Report No. UC SESM 75-7* ; Department of Civil Engineering University of California, Berkeley, July 1975.

[63] de Souza Neto EA, Perić D, Dutko M, Owen DRJ. Design of simple low order finite elements for large strain analysis of nearly incompressible solids. *International Journal of Solids and Structures* 1996; **33**(20–22):3277–3296.

[64] Hauret P, Kuhl E, Ortiz M. Diamond elements: a finite element/discrete-mechanics approximation scheme with guaranteed optimal convergence in incompressible elasticity. *International Journal for Numerical Methods in Engineering* 2007; **72**(3):253–294.

[65] Lipton S, Evans JA, Bazilevs Y, Elguedj T, Hughes TJR. Robustness of isogeometric structural discretizations under severe mesh distortion. *Computer Methods in Applied Mechanics and Engineering* 2010; **199**(5–8):357–373.

[66] Auricchio F, L Beirao da Veiga, Lovadina C, Reali A. An analysis of some mixed-enhanced finite element for plane linear elasticity. *Computer Methods in Applied Mechanics and Engineering* 2005; **194**(27–29):2947–2968.

[67] Lovadina C, Auricchio F. On the enhanced strain technique for elasticity problems. *Computers and Structures* 2003; **81**(8–11):777–787.

[68] Taylor RL. A mixed-enhanced formulation for tetrahedral finite elements. *International Journal for Numerical Methods in Engineering* 2000; **47**(1–3):205–227.

[69] Oñate E, Rojek J, Taylor RL, Zienkiewicz OC. Finite calculus formulation for incompressible solids using linear triangles and tetrahedra. *International Journal for Numerical Methods in Engineering* 2004; **59**(11):1473–1500.

[70] Cervera M, Chiumenti M, Valverde Q, C Agelet de Saracibar. Mixed linear/linear simplicial elements for incompressible elasticity and plasticity. *Computer Methods in Applied Mechanics and Engineering* 2003; **192**(49–50):5249–5263.

[71] Zienkiewicz OC, Rojek J, Taylor RL, Pastor M. Triangles and tetrahedra in explicit dynamic codes for solids. *International Journal for Numerical Methods in Engineering* 1998; **43**(3):565–583.

[72] de Souza Neto EA, Pires FMA, Owen DRJ. F-bar-based linear triangles and tetrahedra for finite strain analysis of nearly incompressible solids. Part I: formulation and

benchmarking. *International Journal for Numerical Methods in Engineering* 2005; **62**(3):353–383.

[73] Thoutireddy P, Molinari JF, Repetto EA, Ortiz M. Tetrahedral composite finite elements. *International Journal for Numerical Methods in Engineering* 2002; **53**(6):1337–1351.

[74] Guo Y, Ortiz M, Belytschko T, Repetto EA. Triangular composite finite elements. *International Journal for Numerical Methods in Engineering* 2000; **47**(1–3):287–316.

[75] Bonet J, Burton AJ. A simple average nodal pressure tetrahedral element for incompressible and nearly incompressible dynamic explicit applications. *Communications in Numerical Methods in Engineering* 1998; **14**(5):437–449.

[76] Dohrmann CR, Heinstein MW, Jung J, Key SW, Witkowski WR. Node-based uniform strain elements for three-node triangular and four-node tetrahedral meshes. *International Journal for Numerical Methods in Engineering* 2000; **47**(9):1549–1568.

[77] Bonet J, Marriot M, Hassan O. An averaged nodal deformation gradient linear tetrahedral element for large strain explicit dynamic applications. *Communications in Numerical Methods in Engineering* 2001; **17**(8):551–561.

[78] Puso MA, Solberg J. A stabilized nodally integrated tetrahedral. *International Journal for Numerical Methods in Engineering* 2006; **67**(6):841–867.

[79] Broccardo M, Micheloni M, Krysl P. Assumed-deformation gradient finite elements with nodal integration for nearly incompressible large deformation analysis. *International Journal for Numerical Methods in Engineering* 2009; **78**(9):1113–1134.

[80] Strang G, Fix G. *An Analysis of the Finite Element Method*. Second edn., Wellesley-Cambridge Press: MA, 2008.

[81] Jun S, Liu WK, Belytschko T. Explicit reproducing kernel particle methods for large deformation problems. *International Journal for Numerical Methods in Engineering* 1998; **41**(1):137–166.

[82] Liew KM, Ng TY, Wu YC. Meshfree method for large deformation analysis-a reproducing kernel particle approach. *Engineering Structures* 2002; **24**(5):543–551.

[83] Zhang X, Yao Z, Zhang Z. Application of MLPG in large deformation analysis. *Acta Mechanica Sinica* 2006; **22**:331–340.

[84] Li S, Hao W, Liu WK. Mesh-free simulations of shear banding in large deformation. *International Journal of Solids and Structures* 2000; **37**(48–50):7185–7206.

[85] Chen JS, Pan C, Roque CMOL, Wang HP. A Lagrangian reproducing kernel particle method for metal forming analysis. *Computational Mechanics* 1998; **22**:289–307.

[86] Yoon S, Chen JS. Accelerated meshfree method for metal forming simulation. *Finite Elements in Analysis and Design* 2002; **38**(10):937–948.

[87] Chen JS, Pan C, Wu CT, Liu WK. Reproducing kernel particle methods for large deformation analysis of non-linear structures. *Computer Methods in Applied Mechanics and Engineering* 1996; **139**(1–4):195–227.

[88] Chen JS, Pan C, Wu CT. Large deformation analysis of rubber based on a reproducing kernel particle method. *Computational Mechanics* 1997; **19**(3):211–227.

[89] Calvo B, Martinez MA, Doblaré M. On solving large strain hyperelastic problems with the natural element method. *International Journal for Numerical Methods in Engineering* 2005; **62**(2):159–185.

[90] Chen JS, Yoon S, Wang HP, Liu WK. An improved reproducing kernel particle method for nearly incompressible finite elasticity. *Computer Methods in Applied Mechanics and Engineering* 2000; **181**(1–3):117–145.

[91] Chen JS, Yoon S, Wu CT. Non-linear version of stabilized conforming nodal integration for galerkin mesh-free methods. *International Journal for Numerical Methods in Engineering* 2002; **53**(12):2587–2615.

[92] Puso M, Zywicz E, Chen JS. A new stabilized nodal integration approach. *Mesh-free Methods for Partial Differential Equations III*, *Lecture Notes in Computational Science and Engineering*, vol. 57. Springer Berlin Heidelberg, 2007; 207–217.

[93] Cho JR, Lee HW. 2-D large deformation analysis of nearly incompressible body by natural element method. *Computers and Structures* 2006; **84**(5–6):293–304.

[94] Batra RC, Porfiri M. Analysis of rubber-like materials using meshless local Petrov-Galerkin (MLPG) method. *Communications in Numerical Methods in Engineering* 2008; **24**(12):1781–1804.

[95] Rossi R, Alves M. On the analysis of an EFG method under large deformations and volumetric locking. *Computational Mechanics* 2007; **39**:381–399.

[96] de Souza Neto EA, Andrade Pires FM, Owen DRJ. F-bar-based linear triangles and tetrahedra for finite strain analysis of nearly incompressible solids. Part I: formulation and benchmarking. *International Journal for Numerical Methods in Engineering* 2005; **62**(3):353–383.

[97] Griebel M, Schweitzer MA. A particle-partition of unity method. Part II: Efficient cover construction and reliable integration. *SIAM Journal on Scientific Computing* 2002; **23**(5):1655–1682.

[98] Gerstner T, Griebel M. Numerical integration using sparse grids. *Numerical Algorithms* 1998; **18**(3–4):209–232.

[99] Riker C, Holzer SM. The mixed-cell-complex partition-of-unity method. *Computer Methods in Applied Mechanics and Engineering* 2009; **198**(13–14):1235–1248.

[100] Atluri SN, Kim HG, Cho JY. A critical assessment of the truly Meshless Local Petrov-Galerkin (MLPG), and Local Boundary Integral Equation (LBIE) methods. *Computational Mechanics* 1999; **24**(5):348–372.

[101] Duflot M, Nguyen-Dang H. A truly meshless Galerkin method based on a moving least squares quadrature. *Communications in Numerical Methods in Engineering* 2002; **18**(6):441–449.

[102] Zou W, Zhou JX, Zhang ZQ, Li Q. A truly meshless method based on partition of unity quadrature for shape optimization of continua. *Computational Mechanics* 2007; **39**(4):357–365.

[103] Zeng QH, Lu DT. Galerkin meshless methods based on partition of unity quadrature. *Applied Mathematics and Mechanics* 2005; **26**(7):893–899.

[104] Carpinteri A, Ferro G, Ventura G. The partition of unity quadrature in meshless methods. *International Journal for Numerical Methods in Engineering* 2002; **54**(7):987–1006.

[105] Balachandran GR, Rajagopal A, Sivakumar SM. Mesh free Galerkin method based on natural neighbors and conformal mapping. *Computational Mechanics* 2008; **42**(6):885–905.

[106] Liu GR, Tu ZH. An adaptive procedure based on background cells for meshless methods. *Computer Methods in Applied Mechanics and Engineering* 2002; **191**(1):1923–1943.

[107] Babuška I, Banerjee U, Osborn JE, Li QL. Quadrature for meshless methods. *International Journal for Numerical Methods in Engineering* 2008; **76**(9):1434–1470.

[108] Schembri P, Crane DL, Reddy JN. A three-dimensional computational procedure for reproducing meshless methods and the finite element method. *International Journal for Numerical Methods in Engineering* 2004; **61**(6):896–927.

[109] Sukumar N, Wright RW. Overview and construction of meshfree basis functions: from moving least squares to entropy approximants. *International Journal for Numerical Methods in Engineering* 2007; **70**(2):181–205.

[110] Ortiz A, Puso MA, Sukumar N. Maximum-entropy meshfree method for compressible and near-incompressible elasticity. *Computer Methods in Applied Mechanics and Engineering* 2010; **199**(25–28):1859–1871.

[111] Ortiz A, Puso MA, Sukumar N. Maximum-entropy meshfree method for incompressible media problems. *Finite Elements in Analysis and Design* 2011; in press.

[112] Ortiz A, Puso MA, Sukumar N. Maximum-entropy meshfree method for near-incompressible nonlinear elasticity 2011; in preparation.

[113] Sukumar N, Malsch EA. Recent advances in the construction of polygonal finite element interpolants. *Archives of Computational Methods in Engineering* 2006; **13**(1):129–163.

[114] Lucy LB. A numerical approach to testing the fission hypothesis. *Astronomical Journal* 1977; **82**(12):1013–1924.

[115] Gingold RA, Monaghan JJ. Smoothed particle hydrodynamics: Theory and application to non-spherical stars. *Monthly Notices Royal Astronomical Society* 1977; **181**:375–389.

[116] Benz W. Applications of smooth particle hydrodynamics (SPH) to astrophysical problems. *Computer Physics Communications* 1988; **48**(1):97–105.

[117] Monaghan JJ. Smoothed particle hydrodynamics. *Annual Review of Astronomy and Astrophysics* 1992; **30**:543–574.

[118] Monaghan JJ. Simulating gravity currents with SPH lock gates. *Applied Mathematics Reports and Preprints* 1995; Monash University.

[119] Springel V, Hernquist L. Cosmological smoothed particle hydrodynamics simulations: a hybrid multiphase model for star formation. *Monthly Notices of the Royal Astronomical Society* 2003; **339**(2):289–311.

[120] Springel V. Smoothed particle hydrodynamics in astrophysics. *Annual Review of Astronomy and Astrophysics*, *Annual Review of Astronomy and Astrophysics*, vol. 48. 2010; 391–430.

[121] Ayliffe BA, Bate MR. Planet migration: self-gravitating radiation hydrodynamical models of protoplanets with surfaces. *Monthly Notices of the Royal Astronomical Society* 2010; **408**(2):876–896.

[122] Libersky L, Petschek A. Smooth particle hydrodynamics with strength of materials. *Advances in the Free-Lagrange Method Including Contributions on Adaptive Gridding and the Smooth Particle Hydrodynamics Method*, *Lecture Notes in Physics*, vol. 395, Trease H, Fritts M, Crowley W (eds.). Springer Berlin / Heidelberg, 1991; 248–257.

[123] Johnson GR, Beissel SR. Normalized smoothing functions for SPH impact computations. *International Journal for Numerical Methods in Engineering* 1996; **39**(16):2725–2741.

[124] Randles PW, Libersky LD. Smoothed Particle Hydrodynamics: Some recent improvements and applications. *Computer Methods in Applied Mechanics and Engineering* 1996; **139**(1–4):375–408.

[125] Fountzoulas CG, Gazonas GA, Cheeseman BA. Computational modeling of tungsten carbide sphere impact and penetration into high-strength-low-alloy (HSLA)-100 steel targets. *Journal of Mechanics of Materials and Structures* 2007; **2**(10):1965–1979.

[126] Khayyer A, Gotoh H. Wave impact pressure calculations by improved SPH methods. *International Journal of Offshore and Polar Engineering* 2009; **19**(4):300–307.

[127] Oger G, Guilcher PM, Jacquin E, Brosset L, Deuff JB, Touze DL. Simulations of hydro-elastic impacts using a parallel SPH Model. *International Journal of Offshore and Polar Engineering* 2010; **20**(3):181–189.

[128] Colagrossi A, Colicchio G, Lugni C, Brocchini M. A study of violent sloshing wave impacts using an improved SPH method. *Journal of Hydraulic Reseach* 2010; **48**(Sp. Iss. SI):94–104.

[129] Zhou CE, Liu GR, Lou KY. Three-dimensional penetration simulation using smoothed particle hydrodynamics. *International Journal of Computational Methods* 2007; **4**(4):671–691.

[130] Binglin L, Jinyu X, Ning S, Jie X, Zhenyu W, Jinyong Y. Computation of steel penetrated by rigid projectile with coupled FEM-SPH methods. *Journal of Projectiles, Rockets, Missiles and Guidance* 2008; **28**(5):105–8.

[131] Bonet J, Kulasegaram S. Correction and stabilization of smooth particle hydrodynamics methods with applications in metal forming simulations. *International Journal for Numerical Methods in Engineering* 2000; **47**(6):1189–1214.

[132] Cleary PW, Prakash M, Ha J. Novel applications of smoothed particle hydrodynamics (SPH) in metal forming. *Journal of Materials Processing Technology* 2006; **177**(1–3, Sp. Iss. SI):1–48.

[133] Liszka T, Orkisz J. The finite difference method at arbitrary irregular grids and its application in applied mechanics. *Computers and Structures* 1980; **11**(1–2):83–95.

[134] Kansa EJ. Multiquadrics–A scattered data approximation scheme with applications to computational fluid-dynamics–I surface approximations and partial derivative estimates. *Computers and Mathematics with Applications* 1990; **19**(8–9):127–145.

[135] Braun J, Sambridge M. A numerical method for solving partial differential equations on highly irregular evolving grids. *Nature* 1995; **376**(6542):655–660.

[136] Melenk JM, Babuška I. The partition of unity finite element method: Basic theory and applications. *Computer Methods in Applied Mechanics and Engineering* 1996; **139**(1–4):289–314.

[137] Babuška I, Melenk JM. The partition of unity method. *International Journal for Numerical Methods in Engineering* 1997; **40**(4):727–758.

[138] Oñate E, Idelsohn S, Zienkiewicz OC, Taylor RL. A finite point method in computational mechanics. applications to convective transport and fluid flow. *International Journal for Numerical Methods in Engineering* 1996; **39**(22):3839–3866.

[139] Duarte CA, Oden JT. An h-p adaptive method using clouds. *Computer Methods in Applied Mechanics and Engineering* 1996; **139**(1–4):237–262.

[140] Li S, Liu WK. Meshfree and particle methods and their applications. *Applied Mechanics Reviews* 2002; **55**(1):1–34.

[141] Fries TP, Matthies HG. Classification and overview of meshfree methods. *Technical Report Informatikbericht-Nr. 2003-03*, Institute of Scientific Computing, Technical University Braunschweig, Braunschweig, Germany 2004.

[142] Liu G, Gu Y. A meshfree method: meshfree weakstrong (MWS) form method, for 2-D solids. *Computational Mechanics* 2003; **33**(1):2–14.

[143] Liu GR, Wu YL, Ding H. Meshfree weak-strong (MWS) form method and its application to incompressible flow problems. *International Journal for Numerical Methods in Fluids* 2004; **46**(10):1025–1047.

[144] Lancaster P, Salkauskas K. Surfaces generated by moving least squares methods. *Mathematics of Computations* 1981; **37**:141–158.

[145] Liu GR, Gu YT. A matrix triangularization algorithm for the polynomial point interpolation method. *Computer Methods in Applied Mechanics and Engineering* 2003; **192**(19):2269–2295.

[146] Liu GR, Gu YT. *An Introduction to Meshfree Methods and their Programming*. Springer: the Netherlands, 2005.

[147] Zhang X, Song KZ, Lu MW, Liu X. Meshless methods based on collocation with radial basis functions. *Computational Mechanics* 2000; **26**:333–343.

[148] Oñate E. Derivation of stabilized equations for numerical solution of advective-diffusive transport and fluid flow problems. *Computer Methods in Applied Mechanics and Engineering* 1998; **151**(1–2):233–265.

[149] Oñate E, Perazzo F, Miquel J. A finite point method for elasticity problems. *Computers and Structures* 2001; **79**(22–25):2151–2163.

[150] Fernández-Méndez S, Huerta A. Imposing essential boundary conditions in mesh-free methods. *Computer Methods in Applied Mechanics and Engineering* 2004; **193**(12–14):1257–1275.

[151] Wang JG, Liu GR. A point interpolation meshless method based on radial basis functions. *International Journal for Numerical Methods in Engineering* 2002; **54**(11):1623–1648.

[152] Liu Y, Belytschko T. A new support integration scheme for the weakform in mesh-free methods. *International Journal for Numerical Methods in Engineering* 2010; **82**(6):699–715.

[153] Jaynes ET. Information theory and statistical mechanics. *Physical Review* 1957; **106**(4):620–630.

[154] Shannon CE. A mathematical theory of communication. *The Bell Systems Technical Journal* 1948; **27**:379–423.

[155] Kullback S. *Information Theory and Statistics*. Wiley: New York, NY, 1959.

[156] Shore JE, Johnson RW. Axiomatic derivation of the principle of maximum entropy and the principle of minimum cross-entropy. *IEEE Transactions on Information Theory* 1980; **26**(1):26–36.

[157] Sukumar N. Construction of polygonal interpolants: a maximum entropy approach. *International Journal for Numerical Methods in Engineering* 2004; **61**(12):2159–2181.

[158] Hormann K, Sukumar N. Maximum entropy coordinates for arbitrary polytopes. *Computer Graphics Forum* 2008; **27**:1513–1520.

[159] Yaw LL, Sukumar N, Kunnath SK. Meshfree co-rotational formulation for two-dimensional continua. *International Journal for Numerical Methods in Engineering* 2009; **79**(8):979–1003.

[160] Cyron CJ, Arroyo M, Ortiz M. Smooth, second order, non-negative meshfree approximants selected by maximum entropy. *International Journal for Numerical Methods in Engineering* 2009; **79**(13):1605–1632.

[161] González D, Cueto E, Doblaré M. A higher order method based on local maximum entropy approximation. *International Journal for Numerical Methods in Engineering* 2010; **83**(6):741–764.

[162] Li B, Habbal F, Ortiz M. Optimal transportation meshfree approximation schemes for fluid and plastic flows. *International Journal for Numerical Methods in Engineering* 2010; **83**(12):1541–1579.

[163] Cyron C, Nissen K, Gravemeier V, Wall W. Stable meshfree methods in fluid mechanics based on Green's functions. *Computational Mechanics* 2010; **46**:287–300.

[164] Cyron C, Nissen K, Gravemeier V, Wall W. Information flux maximum-entropy approximation schemes for convection-diffusion problems. *International Journal for Numerical Methods in Fluids* 2010; **64**:1180–1200.

[165] Rosolen AM, Millán RD, Arroyo M. On the optimum support size in meshfree methods: a variational adaptivity approach with maximum entropy approximants. *International Journal for Numerical Methods in Engineering* 2010; **82**(7):868–895.

[166] Arnold DN, Brezzi F, Fortin M. A stable finite element for the Stokes equations. *Calcolo* 1984; **21**(4):337–344.

[167] Nakshatrala KB, Masud A, Hjelmstad KD. On finite element formulations for nearly incompressible linear elasticity. *Computational Mechanics* 2008; **41**(4):547–561.

[168] Yvonnet J, Villon P, Chinesta F. Natural element approximations involving bubbles for treating mechanical models in incompressible media. *International Journal for Numerical Methods in Engineering* 2006; **66**(7):1125–1152.

[169] Brezzi F, Bathe KJ. A discourse on the stability conditions for mixed finite element formulations. *Computer Methods in Applied Mechanics and Engineering* 1990; **82**(1–3):27–57.

[170] Timoshenko SP, Goodier JN. *Theory of Elasticity*. Third edn., McGraw-Hill: NY, 1970.

[171] Kikuchi N. Remarks on 4CST-elements for incompressible materials. *Computer Methods in Applied Mechanics and Engineering* 1983; **37**(1):109–123.

[172] Turner DZ, Nakshatrala KB, Hjelmstad KD. On the stability of bubble functions and a stabilized mixed finite element formulation for the Stokes problem. *International Journal for Numerical Methods in Fluids* 2009; **60**(12):1291–1314.

[173] Shaughnessy EJ, Katz IM, Schaffer JP. *Introduction to Fluids Mechanics*. Oxford University Press, Inc: NY, 2005.

[174] Hughes TJR, Taylor RL, Sackman JL. Finite element formulation and solution of contact-impact problems in continuum mechanics-iii. *SESM Report 75-3, Department of Civil Engineering, The University of California, Berkeley* 1975; .

[175] Simo JC, Taylor RL, Pister KS. Variational and projection methods for the volume constraint in finite deformation elasto-plasticity. *Computer Methods in Applied Mechanics and Engineering* 1985; **51**(1–3):177–208.

[176] Simo JC, Taylor RL. Quasi-incompressible finite elasticity in principal stretches. continuum basis and numerical algorithm. *Computer Methods in Applied Mechanics and Engineering* 1991; **85**(3):273–310.

[177] de Souza Neto EA, Perić D, Dutko M, Owen DRJ. Design of simple low order finite elements for large strain analysis of nearly incompressible solids. *International Journal of Solids and Structures* 1996; **33**(20–22):3277–3296.

[178] Matthies H, Strang G. The solution of nonlinear finite element equations. *International Journal for Numerical Methods in Engineering* 1979; **14**(11):1613–1626.

[179] Auricchio F, L Beirao da Veiga, Lovadina C, Reali A. The importance of the exact satisfaction of the incompressibility constraint in nonlinear elasticity: mixed FEMs versus NURBS-based approximations. *Computer Methods in Applied Mechanics and Engineering* 2010; **199**(5–8):314–323.

[180] Yamada T, Kikuchi F. An arbitrary Lagrangian-Eulerian finite element method for incompressible hyperelasticity. *Computer Methods in Applied Mechanics and Engineering* 1993; **102**(2):149–177.

[181] Crisfield MA, Moita GF, Lyons LPR, Jelenic G. Enhanced lower-order element formulations for large strains. *Computational Mechanics* 1995; **17**:62–73.

[182] Bonet J, Wood RD. *Nonlinear Continuum Mechanics for Finite Element Analysis*. Cambridge University Press: UK, 2008.

[183] Dowell M, Jarratt P. A modified regula falsi method for computing the root of an equation. *BIT Numerical Mathematics* 1971; **11**:168–174.

[184] Press WH, Teukolsky SA, Vetterling WT, Flannery BP. *Numerical Recipes 3rd Edition: The Art of Scientific Computing*. Third edn., Cambridge University Press, 2007.